PROCESSING AND CHARACTERIZATION OF ENERGETIC AND STRUCTURAL BEHAVIOR OF NICKEL ALUMINUM WITH POLYMER BINDERS

A Thesis
Presented to
The Academic Faculty

By

Morgana Martin

In Partial Fulfillment
Of the Requirements for the Degree
Master of Science in Materials Science and Engineering

Georgia Institute of Technology

April 2005

PROCESSING AND CHARACTERIZATION OF ENERGETIC AND STRUCTURAL BEHAVIOR OF NICKEL ALUMINUM WITH POLYMER BINDERS

Approved by:

Dr. Sathyanaraya Hanagud, Advisor
School of Aerospace Engineering
Georgia Institute of Technology

Dr. Naresh N. Thadhani
School of Materials Science and Engineering
Georgia Institute of Technology

Dr. Min Zhou
School of Materials Science and Engineering
Georgia Institute of Technology

Date Approved: April 5, 2005

ACKNOWLEDGEMENTS

I would like to acknowledge my advisor, Dr. Sathya Hanagud, for the opportunity to conduct this research. I would also like to thank the members of my thesis committee, Dr. Naresh Thadhani and Dr. Min Zhou, for their advice and suggestions. I would like to give a special thank you to Dr. Thadhani for use of his laboratory equipment, materials and facilities, as well as the continuous support and guidance.

Funding for thus research was provided by AFOSR/MURI under Contract No. F49620-02-1-0382.

My appreciation and gratitude goes to Dan Eakins, Lou Ferranti, Dr. Zhiqiang Jin, Matt McGill, Ry Doolittle and Matt Trexler for their contributions in the lab and discussions of results. I would also like to thank Dr. Kimberly Kurtis and Joy Justice for use of compression testing facilities, and Yolande Berta, Mike Haluska, Julia Cernatescu and the Georgia Tech Center for Nanostructure Characterization for providing microscopy and x-ray diffraction training and facilities necessary for my work.

Finally, I would like to express my appreciation to my mom, brother, sister and other family members and close friends for their continued support and encouragement.

TABLE OF CONTENTS

LIST OF TABLES

LIST OF FIGURES

SUMMARY

In the work presented in this thesis, a polymer-based composite reinforced with a mixture of Ni and Al powders was investigated as an example of a multifunctional structural energetic material. Micron-sized Ni powder, nano/micron-sized Al powders, and a polymer binder (10vol% Teflon or 20-30wt% epoxy), were fabricated as bulk materials by pressing or casting. Initial characterization of fabricated materials using scanning electron microscopy (SEM) analysis revealed a uniform distribution of Ni and Al particles in the polymer matrices. Density measurements showed that cast materials achieved much lower porosity than pressed materials, and that materials containing nano-Al were less dense than those containing micron-sized Al.

The **thermally initiated** reaction response of these materials was evaluated using differential thermal analysis (DTA) coupled with x-ray diffraction. The analyses showed evidence of thermally initiated reactions between Ni and Al powders, as well as between Ni+Al and Teflon. Pressed materials showed an additional "pre-initiation" reaction between Ni and Al that was not seen in the cast materials or in the unpressed powder mixtures. Nano-sized Al powder showed a preference for reaction with Teflon over Ni, while micron-sized Al reacted strongly with Ni regardless of the presence of a binder. Teflon was shown to be very reactive with the Ni+Al/nano Al mixture, whereas epoxy was not reactive with the metallic powders, and also inhibited reaction between Ni and nano Al.

The structural/mechanical behavior of these materials was evaluated using elastic and plastic property measurements via static and dynamic compression tests performed

on cylindrical samples. Dynamic mechanical testing using reverse Taylor anvil-on-rod impact tests combined with velocity interferometry gave qualitative and quantitative information about the transient deformation and failure response of the composites. Static compression tests revealed that pressed samples containing Teflon were lacking in strength when compared to the cast samples, due to inherent porosity (up to ~19.8%) present in these samples. The material containing 20wt% epoxy and nano-sized Al powder showed the most superior mechanical properties in terms of elastic modulus, and static and dynamic compressive strength. During dynamic testing, the composite containing 20wt% epoxy and nano-sized Al powder endured the most strain before fracture, as compared to the other cast materials containing Ni and micron/nano Al. The addition of Ni and Al powders to the epoxy matrix increased the strength of the composites, and their tendency toward brittle fracture, as evidenced by Ni particle pullout in SEM analysis. Fracture through the Ni particles was also observed in specimens recovered after reverse anvil Taylor impact tests.

The results illustrate that nano-sized Al particles provide significant enhancement to strength of epoxy composites, but at the expense of reactivity. The nano-Al particles get dissociated from the Ni and Al mixture and swept into the epoxy, generating a nano-Al containing epoxy matrix with embedded Ni particles. The chemical reactivity of the system is thus sacrificed as contacts between Ni and Al powders are minimized. Additionally, the Al_2O_3 coating on the Al nanoparticles provides a barrier to reaction. A mixture of nano-sized Ni and Al particles may however provide the best combination of high strength and reactivity.

CHAPTER 1

INTRODUCTION

Traditional classes of materials typically have conflicting properties; for example, energetic materials have no structural strength, whereas structural materials are inert and have no energy releasing ability. Multifunctional Energetic Structural Materials (MESMs) represent a class of materials with both strength and energy release capabilities. Such materials can greatly advance defense technology, but the conflicting trends make structural energetic materials a challenging multifunctional system. The work described in this thesis is part of a major effort at Georgia Tech, which is focused on design of materials engineered as novel systems to simultaneously attain structural strength and enhanced explosive power so that they can be used to provide a dual-function by combining properties of structural materials and high explosives. This new generation of materials has many potential applications as penetrating warheads, missiles, and high-performance solid rocket propellants.

Alloys based on the intermetallic compounds of nickel and aluminum (Ni-Al) possess an ideal combination of mechanical and physical properties that make them attractive candidates for many high-temperature applications in aviation, automotive and nuclear power engineering. Mixtures of elemental Ni and Al powders also represent a highly reactive material system. While a mixture of powders does not have the mechanical properties to provide the performance needs of a structural material, particle

reinforced polymer composites have many favorable properties including the ability to form into bulk shapes and attain improved mechanical properties.

The physical and mechanical properties of MESMs, the energetics between the reactants, and the influence of initial powder mixture characteristics (e.g. porosity, powder morphology, and volumetric distribution of the constituents) on the fabrication process and subsequent response under impact loading need to be fully investigated [1-5]. In order to examine the role of some of these variables, this study involved fabrication of Ni+Al+polymer binder composites in which the volume percentage and type of polymer binder was varied. Since the strength and reactivity of materials have been shown to change with size [6, 7], which can promote faster reaction initiation and enhance strength, both nano- and micron-sized Al powders were used in fabrication of bulk materials.

The objectives of the work presented in this study include processing and characterization of Teflon or epoxy based polymer composite MESMs consisting of Ni and Al powders of micron and nano sized particles. Both energetic and structural characterization of fabricated samples were conducted using density measurements, microscopy, differential thermal analysis coupled with x-ray diffraction, and elastic and plastic property measurements via compression testing. Additionally, dynamic mechanical testing, using reverse anvil-on-rod Taylor impact tests with high-speed digital photography and velocity interferometry measurements, was performed. The results obtained about dynamic mechanical properties and reaction energetics were correlated to describe the influence of Al particle size and type of binder (Teflon or epoxy) used to fabricate the MESMs.

CHAPTER 2

LITERATURE REVIEW

In this chapter, a brief review is given for intermetallic alloys, especially the nickel-aluminum system, as well as polymer binders, specifically Teflon and epoxy, used to fabricate the MESMs. Self-propagating high temperature synthesis, shock-induced and shock-assisted chemical reactions, and the effects of shock compression on powders are briefly discussed. Energetic and reactive properties of intermetallic-forming materials are discussed in terms of processing variables and characteristics between particular components in a nickel-aluminum-polymer composite. Finally, structural and mechanical properties are discussed, with a focus on dynamic mechanical behavior and reverse anvil Taylor impact testing as applied to reinforced polymer composites.

2.1 Multifunctional Energetic Structural Materials

Traditional organic high explosives have no structural strength, whereas traditional structural materials like metals have no explosive power. Multifunctional Energetic Structural Materials (MESMs) are defined as materials with both mechanical strength and reactive capabilities. Development of tools for the optimal design of multifunctional materials made of reactive mixtures is of great importance in the area of defense. MESMs can be engineered as novel systems to simultaneously attain structural strength and enhanced explosive power (much higher than organic explosives) so that they can be used as a dual-functioned material to replace (or partially substitute for) structural materials and high explosives. This new generation of materials has potential

applications for future weapons such as penetrating warheads, missile components, and high-performance solid rocket propellants.

2.1.1 Intermetallic-Forming Materials

Intermetallic compounds are alloys formed in particular binary compositions that are true chemical compounds. Their formation is associated with large amounts of energy release (with $\Delta H_f << 0$). The thermodynamic properties of intermetallics account for their physical characteristics; free energy of formation is related to phase stability, heat of formation is related to type of bonding, entropy of formation is related to changes in vibrational behavior and configuration of atoms [2]. Intermetallic compounds have highly desirable characteristics such as high-temperature strength, and corrosion and oxidation resistance [8]. Shock synthesis studies on binary elemental mixtures forming intermetallic compounds have been performed because of their potential applications as high temperature structural materials and their large negative heats of formation.

2.1.1.1 Nickel-Aluminum

Alloys based on the intermetallic compound of nickel and aluminum (e.g. NiAl and Ni_3Al) possess an ideal combination of mechanical and physical properties that make them attractive candidates for many high-temperature applications in aviation, automotive, and nuclear power engineering. These properties include a high melting point, high strength-to-weight ratio, low density, and high thermal conductivity [6, 9]. The Ni-Al system has the additional advantage of existence of large differences in the heats of reaction of its various intermetallic compounds (e.g. $NiAl_3$, Ni_2Al_3, NiAl, and Ni_3Al), as seen in Figure 2-1 [2]. The large differences in heats of reaction have been exploited via use of highly economic and energy-efficient self-sustaining chemical

reactions. Shock synthesis of nickel aluminides via shock-initiated chemical reactions has also been investigated [2].

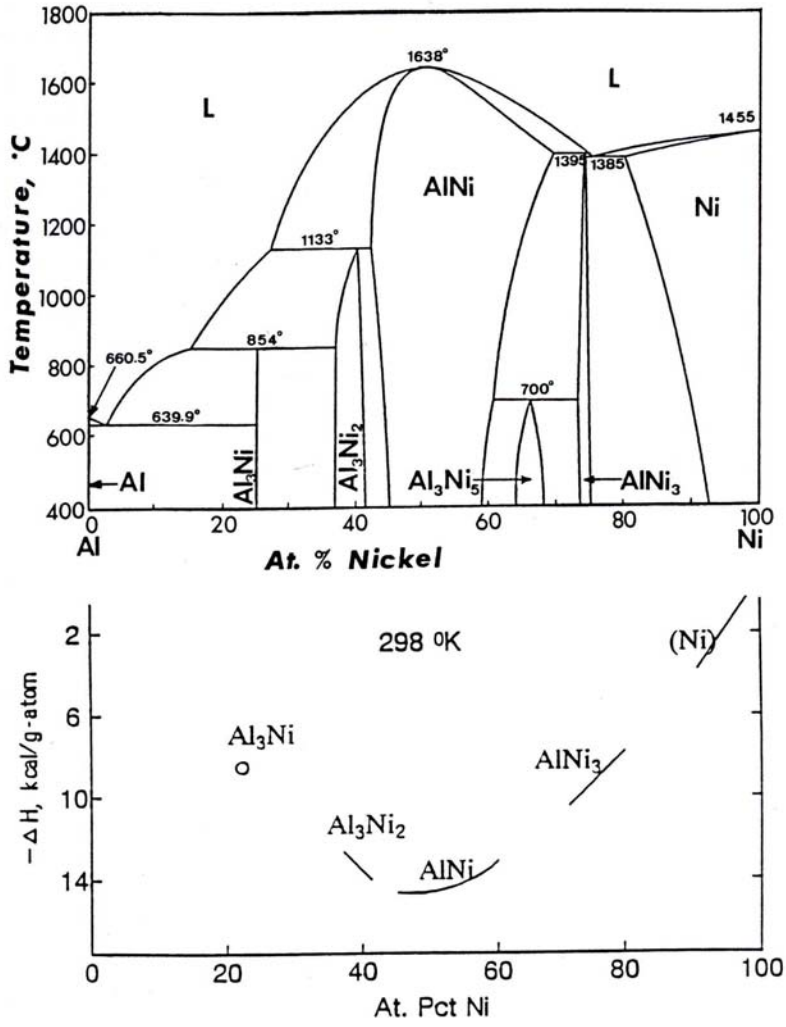

Figure 2-1: Phase diagram of Ni-Al system and heats of formation of the various phases in the system [10].

Previous work on shock synthesis in the nickel aluminide system was first done by Horie *et al.* [3, 11]. Nickel aluminides were shock synthesized from mechanically mixed powders in the appropriate stoichiometric ratios to form Ni_3Al. It was found that

the products were readily synthesized with large production yields, and were controlled by the shock conditions in that the reaction product was determined by the shock pressure.

2.1.2 Reinforced Plastics

Most composites consist of a binder or matrix and a structural reinforcement. The reinforcement is much stronger and stiffer than the matrix, and gives the composite its good properties. The matrix simply holds the reinforcements in an orderly pattern. Because the reinforcements are usually discontinuous, the matrix also helps to transfer load among the reinforcements. Reinforced composites result in a lightweight material with high strength. Polymer binders are often used as matrix materials in composites to provide lateral support to the fibers and transfer loads. They can also be a source of toughness in the composite.

2.1.2.1 Teflon

A candidate matrix material is polytetrafluoroethylene (PTFE), or Teflon, the chemical structure of which is shown in Figure 2-2 as a monomer and in Figure 2-3 as a polymer. Teflon is a polymer with a very unusual combination of properties and a high melting point (327 °C). Due to its nonpolarity, Teflon is very inert and has an electrical resistance over 10^{18}. Teflon has a very low coefficient of friction due to low interfacial forces between its surface and other materials, and it also requires a relatively low force for deformation. Carbon-carbon and carbon-fluorine bonds are among the strongest in single bond organic chemistry, so a large amount of thermal energy is required to break down the material. However, decomposition of Teflon can lead to its constituents undergoing chemical reactions with other components.

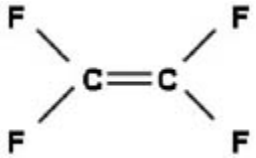

Figure 2-2: Monomer tetrafluoroethylene (C_2F_4)

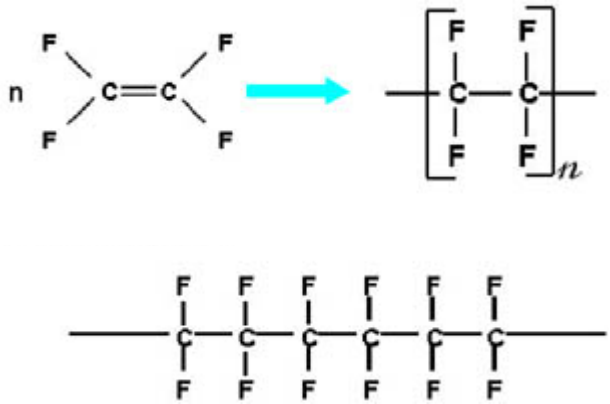

Figure 2-3: Polymer poly(tetrafluoroethylene)

2.1.2.2 Epoxy

Epoxy is a thermoset polymer commonly used as a matrix to form high strength composite materials. It is comprised of two parts: a resin, or low molecular weight polymer with epoxy groups at each end, as shown in Figure 2-4, and a hardener, or diamine, which is shown in Figure 2-5. When the two components of epoxy react, they form a crosslinked molecule as shown in Figure 2-6. Epoxy does not soften prior to degradation. Because of its thermosetting characteristics, it can be easily cast-cured into shapes.

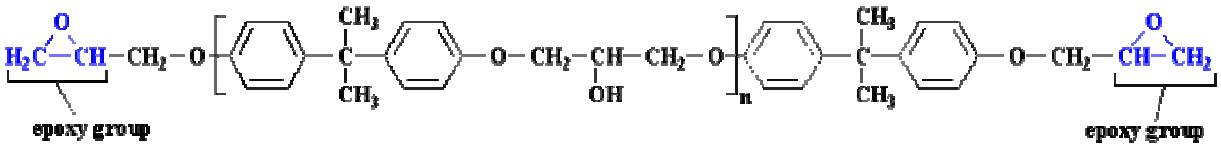

Figure 2-4: Resin: low molecular weight polymer

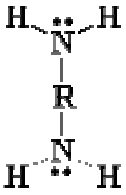

Figure 2-5: Hardener: diamine

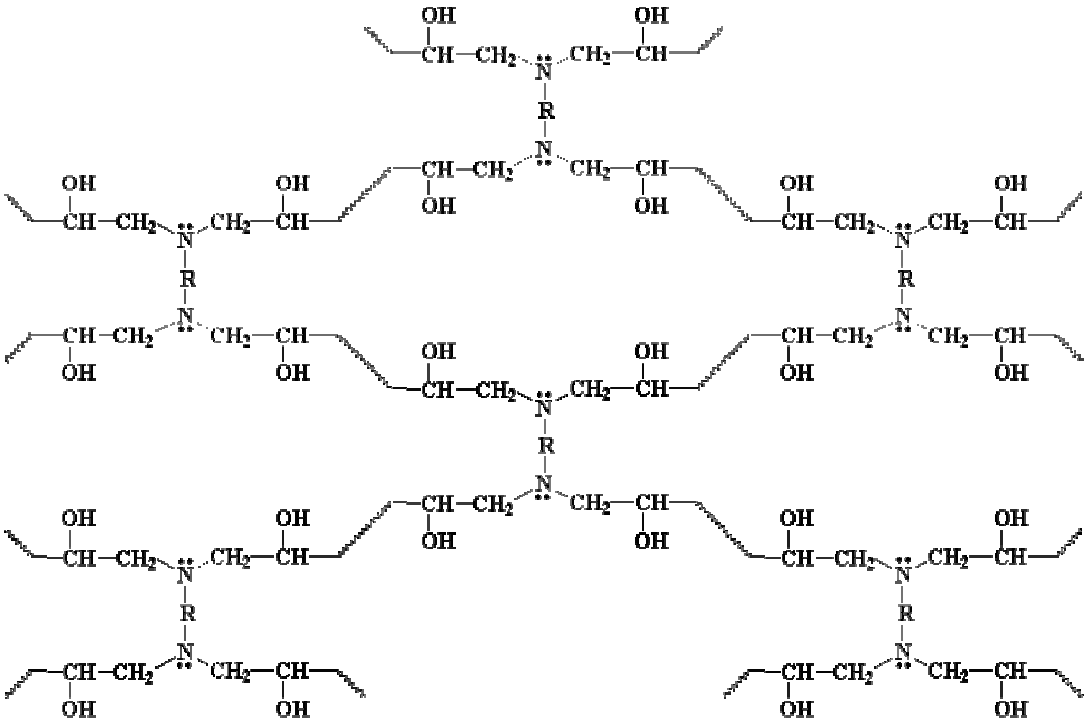

Figure 2-6: Crosslinked epoxy network

2.1.3 Reinforced Polymer Composites

The addition of metal particles to polymer matrices produces composites of greater density, improved electrical conductivity, better thermal conductivity, better behavior at high temperatures, as well as improved mechanical properties. Metals and plastics can be combined in several ways, including dispersing metal powders in the liquid mixture of thermosetting resins and their curing agents, to form composites [12].

Polymeric materials usually have low mechanical moduli and high vibration damping properties. At high temperatures, their mechanical moduli decrease further, and the materials are therefore practically inoperative for structural purposes. Composites produced from a mechanical combination of polymeric matrices and stiff, non-dissipative fillers can possess high stiffness and high damping which is ideal for structural materials. Thermal properties can also be improved by addition of thermally conductive fillers [12].

2.2 Energetic/Reactive Properties of Intermetallic-Forming Powder Mixtures

Many studies have been done employing various methods to study the energetics of intermetallic-forming materials systems. These methods include self-propagating combustion synthesis, shock-induced and shock-assisted chemical reactions, and ball-milling of powders, which all result in mechanical alloys. A brief description and comparison of these methods follows.

2.2.1 Self-Propagating High Temperature Synthesis

Self-propagating high temperature synthesis (SHS) of materials involves ignition of a compressed powder mixture, which produces a chemical reaction with sufficient heat release that it becomes self-sustaining [13]. SHS reactions typically propagate at velocities less than 1 m/s [14].

Intermetallic-forming mixtures for SHS are of particular interest. These mixtures consist of particles that are in near atomic scale proximity, but are constrained from reaction until triggered. Once triggered, the reaction will become self-sustaining if the rate of heat release exceeds the rate of heat dissipated, and a new intermetallic alloy will be produced [6]. The following is an example of an SHS reaction between Ni and Al in which a nickel-aluminide alloy is produced [15]:

$$Ni + Al \rightarrow NiAl,\ \Delta H_{comb} = 7.15\ kJ/cm^3,\ T_{af} = 1910\ K$$

This reaction is sufficiently exothermic such that the chemical energy generated will propagate the heat wave through the sample.

2.2.2 Shock Reactive Synthesis

Shock reactive synthesis (SRS) of materials is based on shock-wave ignited reactions where the induced shock pressure in the condensed matter (usually a mixture of powders) is a governing factor in synthesis of intermetallic compounds from elemental mixtures [16]. The simultaneous application of high pressure and high strain rate deformation characterize this reaction process [3]. A shock wave which triggers a reaction travels at a velocity that can be of the order of 1 km/s, so substantial reaction may not occur in the shock front, but the reaction will be initiated throughout the powder on a much shorter time scale than that of an SHS reaction [14].

Shock compression of powders results in various types of mechanical, physical and chemical effects that can alter the solid-state reactivity of the powders. Shock synthesis involves very high pressure, significant heat release, increases in temperature on the microsecond timescale, as well as large local stresses and temperature gradients, forced relative mass motion, mechanically induced saturation levels of point and line

defects, and cleansing of existing surfaces [11]. Extensive plastic deformation, fluid-like turbulent flow, heating, particle comminution, and mixing of constituents with cleansed surfaces are possible [1, 2, 4, 17, 18]. These changes cause an enhancement in chemical reactivity that can cause powder mixtures to undergo chemical reactions during the microsecond duration shock state [1, 17], and can result in the formation of metastable phases, nonequilibrium compounds, or radically modified microstructures. The processes of void collapse, particle deformation and flow, particle fracture/comminution, intimate mixing that can cause interparticle fusion, restructuring of atoms, generation of activated states, and formation of stable or metastable phases are only possible by the shock-compression technique [2]. These chemical reactions and formation of new compounds are of interest in applications relevant to synthesis of intermetallic compounds [19].

The events occurring during shock compression that are thought to be important in leading to chemical reaction in powder mixtures are summarized by Horie *et al.* [3, 11] as:

(a) Initial pressure pulse reverberations within individual particles, high speed motion of dislocations, formation of defects, cleaning of surfaces, and possible creation of fresh surfaces.

(b) Consolidation of particles into a fully dense state due to plastic deformation.

(c) Solid state diffusion and localized melting at enhanced rates.

(d) Local chemical reactions leading to exothermic reactions and correspondingly large increases in temperature.

(e) Formation of reaction products appropriate with pressure, temperature and defect state of the materials.

(f) Crystallization of end products.

2.2.3 Self-Propagating High Temperature Synthesis vs. Shock-Induced Chemical Reactions

In an attempt to better understand the similarities and differences in mechanisms of SHS and shock-induced chemical reactions, Krueger *et al.* [14] showed that in shock-densified powder compacts a reduction in reaction initiation temperature occurs, which is similar to the initiation of combustion type SHS reactions at lower than usual temperatures in green compacts pressed to high densities, or in compacts heated at slow rates. These conditions promote a significant degree of solid-state diffusion leading to the bulk of the reaction occurring in the solid-state.

In a study by Hammetter *et al.* [20], the effect of shock-loading on SHS type chemical reactions was investigated in a Ni-Al system while heating during DTA. This study showed that unshocked Ni-Al mixtures displayed one main exotherm near the melting temperature of aluminum (near 650 °C). In contrast, the shock-densified mixtures displayed an additional "pre-initiation" exotherm at approximately 550 °C in addition to the main exotherm, as can be seen in Figure 2-7. X-ray diffraction showed that while the "pre-initiation" exotherm corresponds to the formation of $NiAl_3$, the main exotherm corresponds to Ni_3Al formation. The presence of this "pre-initiation" exotherm in the shocked powder mixtures was attributed to fine scale mechanical mixing, generation of intimate contacts, and surface conditioning of the elemental powders during shock compression. These characteristics lead to enhanced chemical reactivity and solid-state diffusion reactions at lower temperatures. It was also shown that the chemical reactivity of the powder mixtures, deduced based on the area under the pre-initiation exotherm, increased with increasing intensity of shock conditions, indicating that the

amount of shock-induced mixing and conditioning is controlled by the kinetic energy of the shock process [20].

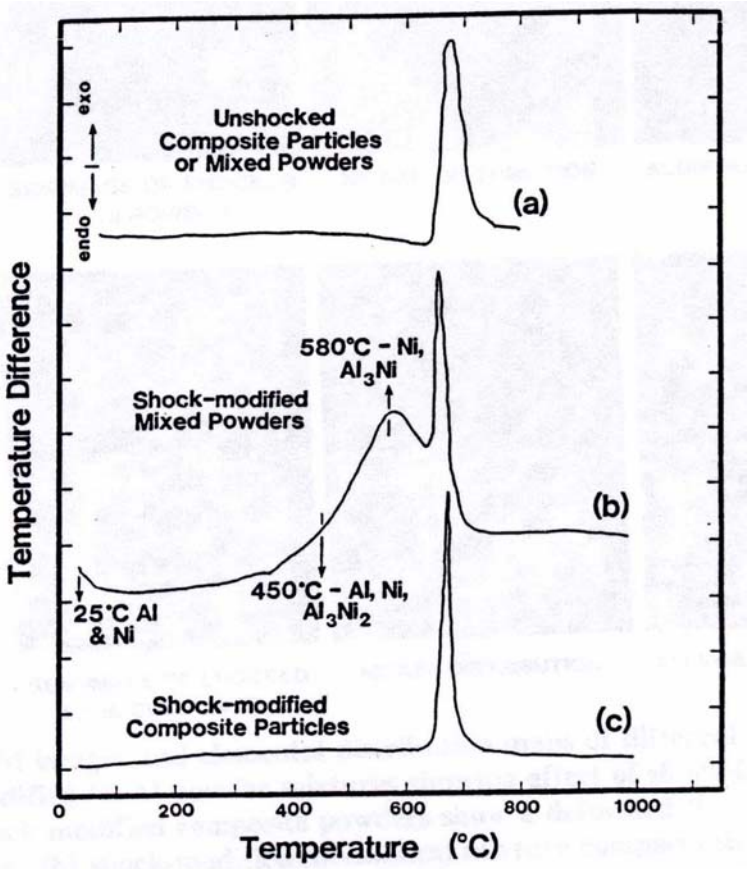

Figure 2-7: DTA traces of (a) unshocked, (b) shock-treated mechanical mixtures, and (c) shock-treated composite powders of Ni-Al [20]. The shock-modified powder mixture shows an additional reaction exotherm (at a lower temperature) due to enhanced diffusion caused by fine scale mixing and intimate contacts.

Namjoshi [21] conducted a similar DTA study on Ti-Si powder, in which two exothermic reactions were observed. The first exotherm was believed to be due to the formation of a product via a solid-state diffusion reaction before sufficient heat was released to trigger the final combustion-type exothermic reaction resulting in the higher

temperature exotherm [21]. These DTA studies provide evidence that shock compression indeed alters the chemical reactivity of powder mixtures.

2.2.4 Shock-Induced vs. Shock-Assisted Reactions

Questions remain as to whether shock-induced chemical reactions occur as a direct consequence of the high pressures generated during shock-loading, or if the reactions are initiated under shock pressure conditions but later time thermal effects are responsible for their propagation [4]. The enhancement in chemical reactivity caused by shock-compression of powder mixtures makes it difficult to delineate between "shock-induced" and "shock-assisted" chemical reactions. Shock-induced reactions have been defined as those occurring in the time scale of pressure equilibration (nano- to micro-second duration), while shock-assisted reactions are those occurring in time scales of thermal equilibration (tens of microseconds to milliseconds) as a result of shock activation of powders [18]. Often, temperature transients and residual heating experienced during shock loading can be sufficiently high such that the shock-initiated reactions can become self-sustained due to shock assisted reactions [18]. Shock waves can deposit a significant amount of thermal energy in powders pressed at low density. The plastic deformation associated with void collapse and relative interparticle motion can result in a significant energy deposition. Shock wave propagation through powders results in deformation of the material occurring at the shock front, as the pressure is raised to several GPa in a short duration and the material behind the shock front attains particle velocities of hundreds of meters per second[14].

Krueger *et al.* [14] found that in a 1:1 atomic ratio nickel-silicon powder mixture, a thermal energy threshold exists below which only minor surface reactions occur and

above which the reaction proceeds to completion. They claim this as evidence that thermal energy is the critical parameter for bulk reactions, and that shock effects are of secondary importance [14]. Since chemical reactions can occur in these shock-modified powder mixtures [17] at lower temperatures and faster rates than self-sustaining combustion reactions [22], Thadhani [18] has classified these as post-shock, or "shock-assisted," chemical reactions occurring as a result of shock compression assisting the powder for subsequent thermal initiation.

Vandersall and Thadhani [19] used recovery experiments and time-resolved measurements to investigate the difference between "shock-induced" (occurring during the high pressure shock state) and "shock-assisted" (due to bulk temperature increases subsequent to unloading from the shock state) chemical reactions in a Mo + 2Si powder mixture system. Based on post-mortem microstructural characterization of shocked samples, they observed formation of mixed phases and partially reacted products and attributed those to thermally initiated chemical reactions, while formation of the single-phase reaction product was found to be due to pressure-initiated reactions [19]. The thermally initiated reactions producing mixed phases and partially reacted products were observed in fixtures (e.g. cylindrical implosion geometry) in which large increases in shock-generated bulk temperatures, produced in time scales of thermal equilibrium following unloading from the high pressure state, were expected. Hence, these are referred to as "shock-assisted" chemical reactions. The single phase reaction products believed to be caused by pressure-initiated reactions occur during the rise to peak pressure and in time scales of pressure equilibrium such as those produced in planar loading geometries. Therefore, these are referred to as "shock-initiated" reactions.

2.2.5 Variables Influencing Shock-Initiation of Reactions

Shock-initiation of chemical reactions occurring between components of intermetallic-forming powder mixtures are influenced by a number of parameters. These variables include shock loading conditions, powder particle morphology (shape), volumetric distribution, and particle size [2]. The effects of each of these have been studied in intermetallic-forming powder mixture systems. The results of some of these studies will be described below.

Chemical reactions occurring during shock compression have been shown to be influenced by the intensity of shock-loading conditions [1-5, 23], as shown in Figure 2-8 by the presence of different reaction products due to different impact velocities. Shock loading conditions affect chemical reactions since they control the degree of plastic flow, mechanical mixing between the constituents, and densification. Additionally, the physical, mechanical and hydrodynamic properties of the starting materials, the energetics between the reactants, and the initial powder mixture characteristics such as porosity, powder morphology, and volumetric distribution of the constituents influence the reaction synthesis process [1-5].

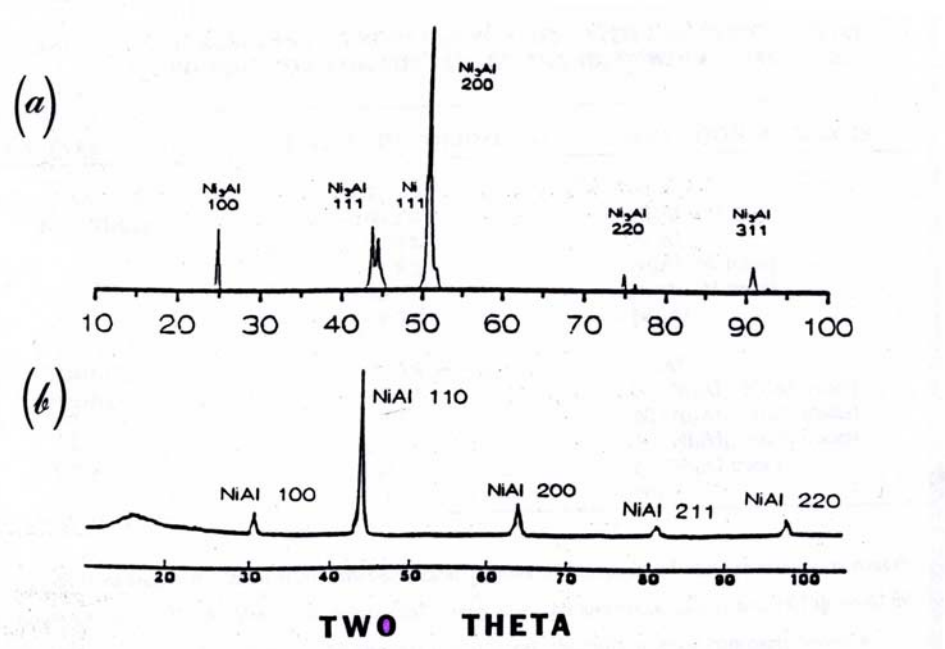

Figure 2-8: XRD traces of 3Ni + Al powder mixture shock synthesized at (a) 1.28 km/s and (b) 1.6 km/s [2] showing presence of different reaction products due to different impact velocities.

Thadhani [4] conducted a study with nickel and aluminum powders of spherical and flaky powder morphology to determine the effect of morphology and shock conditions on the extent and nature of reaction product formed. It was shown that under similar shock conditions the compact (65 at% Ni and 35 at% Al) with flaky Ni (~44 μm) and spherical Al (~44 μm) particles (ρ = 4.20 g/cm^3) displayed maximum reactivity due to more efficient contact between these powder types. The fine powder mixtures (10-20 μm) of Ni and Al exhibited lower reactivity due to improper mixing since the very fine powders tended to agglomerate with like particles. Likewise, coarse powders showed minimal reaction since particles are not brought into intimate contact and mixing with each other. There was also a tendency for the reaction to yield NiAl when the flaky powder was used and Ni_3Al when the coarse or round powders were the reactants. In

terms of shock conditions, the lowest shock condition (generated upon impact at a velocity of 0.9 km/s) led to very little reaction to a Ni_3Al product in the coarse powder mixture, but a significant amount of reaction occurred forming the intermetallic compound Ni_3Al in the flaky powder mixture, along with complete depletion of Al. At a higher velocity of 1.37 km/s, the coarse powder showed more reaction to Ni_3Al as well as traces of NiAl, along with retention of some Ni and Al, while the flaky powder showed both products and some elemental Ni. At the highest shock conditions (1.60 km/s), both the coarse and flaky powders showed NiAl as the primary product. These results led to the conclusion that higher shock pressures coupled with flaky powder morphology enhance the molecular-scale mixing between dissimilar particles. This suggests that shock synthesis involving "shock-induced" reactions is more of a mechanochemical process rather than a thermochemical process.

The effects of varying morphology and volumetric distributions of Ni-Al powder mixtures have also been studied by Dunbar *et al.* [17]. The degree of macroscopic mixing, contact intimacy, and activation were varied through the use of powder mixtures of different morphology and volumetric distribution that were all shock-treated under the same conditions [17]. It was determined that mixtures containing 3Ni+Al (or equimolar) distribution of powders and flaky or irregular morphologies undergo a significant extent of configuration change during shock compression resulting in an activated, intimately mixed and close-packed state. These conditions readily lead to subsequent chemical reaction initiated by heating, such as during DTA. Hence, as shown in Figure 2-9, reaction in flaky and fine 3Ni+Al powder mixtures is dominated by a solid-state process occurring below the melting of Al, while the coarse powder shows a small solid-state

diffusion reaction and the bulk of the reaction occurring with the melting of Al. As seen in Figure 2-10, the 3Ni+Al (equimolar) distribution of coarse powders shows both solid-state reaction and another reaction occurring with melting of Al, while the other two stoichiometries show no solid-state diffusion reaction.

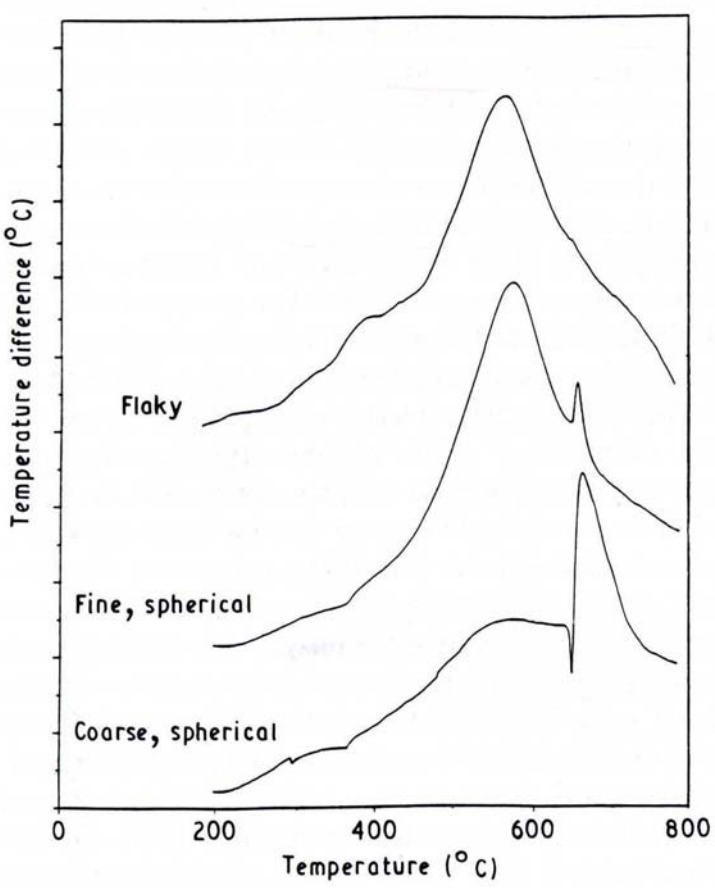

Figure 2-9: DTA traces of 3Ni + Al showing the effect of powder morphology [17]. Reaction in flaky and fine 3Ni+Al powder mixtures is dominated by a solid-state process occurring below the melting of Al, while the coarse powder shows a small solid-state diffusion reaction, with the bulk of the reaction occurring with the melting of Al.

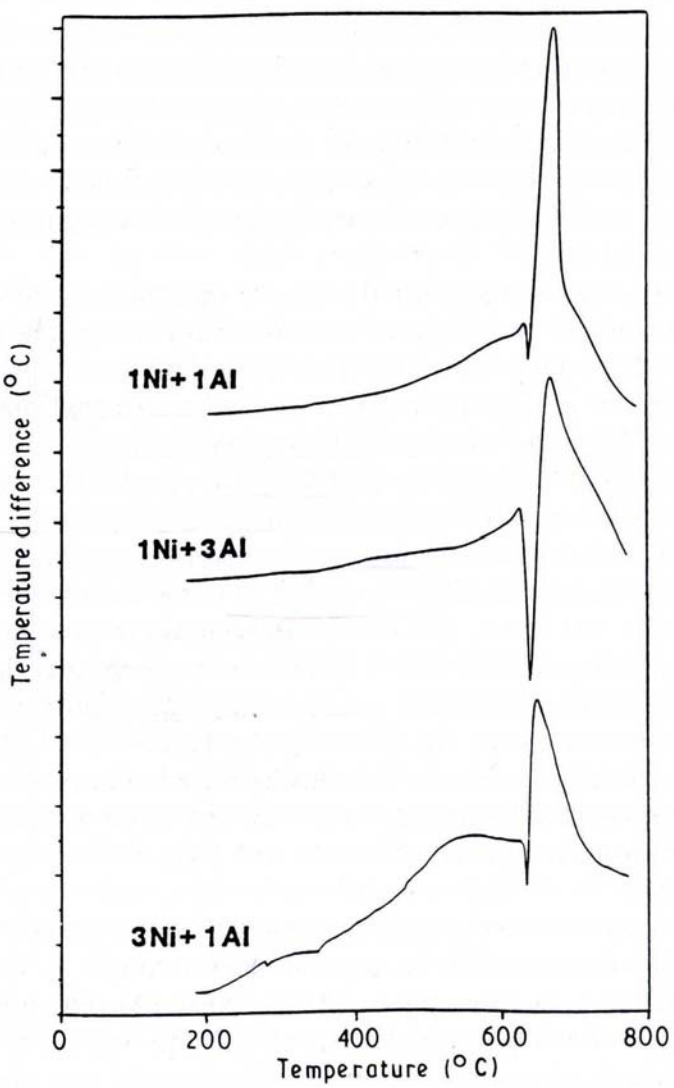

Figure 2-10: DTA traces showing the effect of volumetric distribution [17]. The 3Ni+1Al distribution of powders shows both a solid-state reaction and an additional reaction occurring with melting of Al, while 1Ni+3Al and 1Ni+1Al show no solid-state diffusion reaction.

Song and Thadhani [23] conducted an experiment to determine the effects of the peak shock energy on the extent of the reaction and the type of product formed in a Ni + Al system. The peak shock energy is a function of the peak shock pressure and change in density from initial to final state. More specifically, the effects of shock pressures and densities were investigated using powders of varying densities packed in steel recovery

fixtures impacted at three different velocities. In the experiments where packing density was varied from 29.8 to 72.8% dense, complete reaction to Ni_3Al was observed in flaky powder mixtures pressed at densities up to 55.2% dense, and in spherical powder mixtures up to 50.5% dense. It was determined that the onset energy for complete reactions in flaky powders is ~663 kJ/kg, and the onset energy state for reactions in spherical powders is ~721 kJ/kg.

2.2.6 Nano Energetic Systems

The development of nano-composite thermites for SHS applications is of particular interest. Ultrafine grain powder mixtures of thermite-like materials have been shown to exhibit greater reaction rates than conventional grain size thermite mixtures [24]. Al and MoO_3 powder mixtures with average particle sizes between 20-50 nm have been shown to react more than 1000 times faster than conventional powdered thermites due to the reduced diffusion distances between the reactants [24]. The melting temperatures of certain materials have also been shown to decrease with size [6, 7], which can promote faster ignition and reduced reaction times.

In the micron scale regime, burn rate has been shown to increase with decreasing reactant particle size [25]. Makino and Law [9] showed for Ni-Ti and Co-Ti systems that burn rate increases as a function of inverse radius for particles between 50 and 300 μm radius. These studies suggest that burn rates can further increase as particles progress into nano sizes. However, this may not apply to nano-scale particles due to their high surface area-to-volume ratio and unique physical properties. In preliminary studies, nano-scale particles have been shown to generate significantly higher burn rates over micron-size particle [26]. Increased burn rates are indicative of higher heating rates

during product formation, which can lead to synthesized products with fewer impurities. Because nano particles have a significantly higher surface area-to-volume ratio, more contact between fuel and oxidizer is achieved. Nano powders have also been shown to increase the homogeneity of mixtures due to their size and geometry, which may improve the microstructure of the final product [6].

Aluminum powder is commonly added to explosives, propellants and pyrothechnics to improve their performance. Oxidation of Al is known to add energy to the burning reaction in propellants and to enhance the blast effect of explosives. Due to its large surface area and therefore enhanced reactivity, Al nanopowder can cause dramatic improvements in the performance of some energetic materials [27, 28].

The melting temperature of Al is typically around 660 °C, but nano-Al has been shown to have a melting temperature as low as 353 °C for 20 nm Al and 462 °C for 80 nm Al particles [27]. In a study by Hunt *et al.* [6], ignition time and temperature were determined as a function of Al particle size during laser ignition experiments on pressed NiAl pellets, and the nano-scale composites were observed to have significantly reduced ignition times in comparison to the micro-scale composites due to the thermal properties associated with nano-particles.

Nano-scale Al particles have physical properties that are different from those of micron-scale particles. Pure Al is pyrophoric, so each particle is typically coated with a 1-4 nm Al_2O_3 passivation layer to prevent accidental ignition. As particle size decreases, the total percentage of Al_2O_3 increases and can become a large amount of the total powder [6]. The rate at which energy is released is a function of particle size distribution, degree of intermixing of Al and oxidizer powders, mean oxide thickness, and physical

characteristics of the amorphous alumina shells. Total energy released is a function of reaction stoichiometry, or the ratio of pure Al to oxidizer [24].

Aumann *et al.* [24] showed that activation energy for oxidation of ultrafine grain particles is less than that for nominally flat surfaces, and small particles oxidize faster than larger particles. Al_2O_3 has been found to act as a diluent causing a decrease in both maximum reaction temperature and velocity. Al_2O_3 also acts as a heat sink and less energy is available for the reaction to propagate [29], and in a Ni-Al system the presence of Al_2O_3 impedes the free flow of the Al liquid phase around the Ni particles, which is an important step in product formation [29]. Al_2O_3 causes the core Al to remain isolated from the oxidizer material until external energy is introduced into the composite causing the oxide shells to break resulting in initiation of a self-propagating reaction [24].

Hunt *et al.* [6] examined the effects of the trade off between decreasing Al particle size and increasing Al_2O_3 content on burn velocities and microstructural features of the final product, as well as the effect of particle size on ignition in a Ni-Al system. As shown in Figure 2-11, it was determined that ignition time is reduced by an order of magnitude when Al particle size is decreased to the nano-scale; this may be an effect of the particle size-dependent melting temperature. Since the nano-sized particles melt at lower temperatures, as shown in Figure 2-12, diffusion between the Ni and Al particles occurs at lower temperatures and causes ignition to initiate earlier. Flame propagation was more homogeneous with nano-composite Ni-Al, and burn rates were found to decrease with Al particle size. This is in contrast with expectations since diffusion is enhanced in these particles, but it may be explained by the presence of the Al_2O_3 passivation layer which acts as a heat sink and retards flame propagation. As the Al_2O_3

content increases, the burn rate continues to decrease. Microstructurally, products tended to be more homogeneous as reactant particle size decreased. SEM micrographs taken during this study have revealed the development of fibrous structures on the edges of the burnt pellets in the samples containing high percentages of Al_2O_3. These whiskers are believed to be due to the unique thermal properties of nano-scale particles. The lower melting temperature of Al may lead to a lowered boiling point if the melted Al nano-particles remain isolated in particle surrounded by Ni. The nano-liquid may then maintain the intermolecular forces experienced during its solid state, which would allow the liquid to transfer to a vapor at a lower temperature. If these nano-liquid droplets indeed have a lower vapor pressure than the bulk, Al vapor could exist earlier than with bulk Al particles. The presence of Al vapor at earlier times may contribute to the formation of Al_2O_3 whiskers in the nano-scale samples.

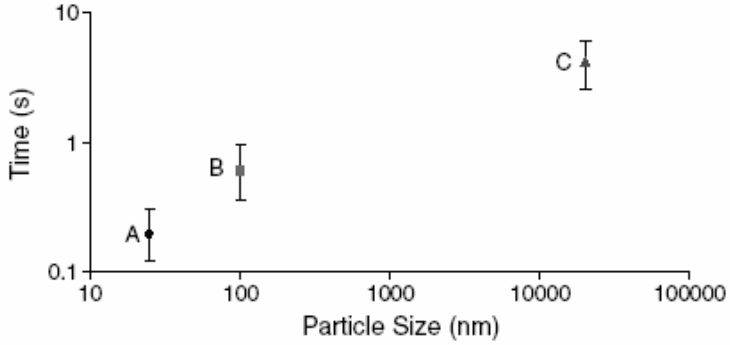

Figure 2-11: Ignition time as a function of Al particle size [6]

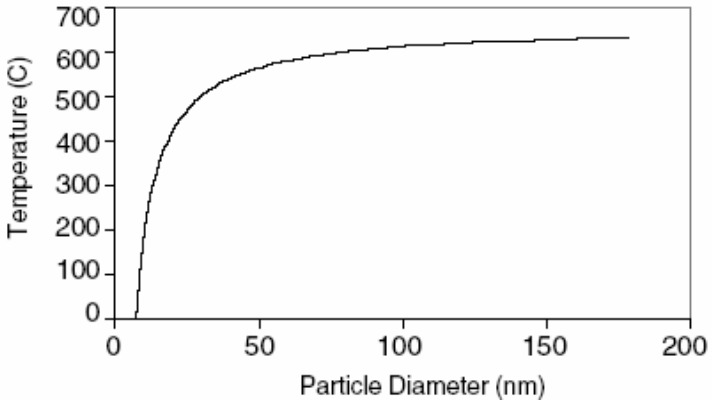

Figure 2-12: Melting temperature as a function of Al particle diameter [6]

2.2.7 Polymer Energetic Systems

Several activation techniques have been explored for overcoming thermodynamic or kinetic limitations in systems that could otherwise have self-propagating reactions. Specifically, the use of chemical promoters has been investigated to increase the reactivity of these systems [30].

The addition of polytetrafluoroethylene (PTFE or Teflon) to Ni-Al intermetallic-forming mixtures has been shown to affect the extent of reaction. Woody *et al.* [31] observed SHS-like reactions in metal powders mixed with Teflon and impacted at 13 m/s in a drop-weight test using real-time emission measurements of the reacting materials with an infrared detector and spectrometer. Qualitative signs of reaction in this study included visible light emission, audible signal, and altered characteristics of the recovered sample's surface. The most exothermic samples exhibited a visible flash and sustained burning after impact, which varied by changing the percentages of Teflon added to the mixture. The Ni-Al system showed an increase in infrared emission and decreased reaction time with the addition of Teflon, but the overall increase in exothermic release was not as substantial as that observed in other systems.

In a study of the Al and Fe_2O_3 thermite system mixed with 10 wt% Teflon, shock-induced chemical reactions were analyzed. Two types of chemical reactions were proposed: an Al + Fe_2O_3 reaction and an Al + Teflon reaction, in which a gaseous AlF_j (j=1,2,3) is produced. The Teflon powder is much softer than either of the other two components, so it was assumed that most of the pore collapse energy is absorbed by the Teflon. This results in a temperature increase causing it to decompose and react with the Al, through the following steps:

$$\text{Teflon} + 4\text{Al} \rightarrow 4\text{AlF}_3 + 6\text{C}$$

$$\text{Teflon} \rightarrow \text{C}_2\text{F}_4 \text{ -1.42 kJ/g}$$

$$3\text{C}_2\text{F}_4 + 4\text{Al} \rightarrow 4\text{AlF}_3 + 6\text{C}$$

$$\text{Teflon} + \text{Al} \rightarrow 4\text{AlF}_2 + \text{C} \text{ or Teflon} + 2\text{Al} \rightarrow 2\text{AlF} + \text{C}$$

However, no single chemical reaction was found to describe the results, indicating that different gases are produced. It was proposed that the aluminum fluoride produced varied depending on shock pressure, with the fluorine-rich compound favored at higher shock pressures [32].

The role of Teflon as a reaction promoter and a carburizing agent was studied in the context of SHS of TiC-Ti composites from elemental powders. A threshold amount of Teflon was found to be necessary to sustain the reaction front. It was determined that the combustion temperature and velocity of the propagating front increased with the amount of Teflon added to the mixture, as shown in Figure 2-13 and Figure 2-14, respectively. The amount of Ti in the end product correspondingly decreased, which demonstrated that the polymer directly participates in the carburization process. In this

reaction system, TiF_3 was found to be an intermediate species that triggered the Teflon activated combustion synthesis of TiC_x-Ti composites [30].

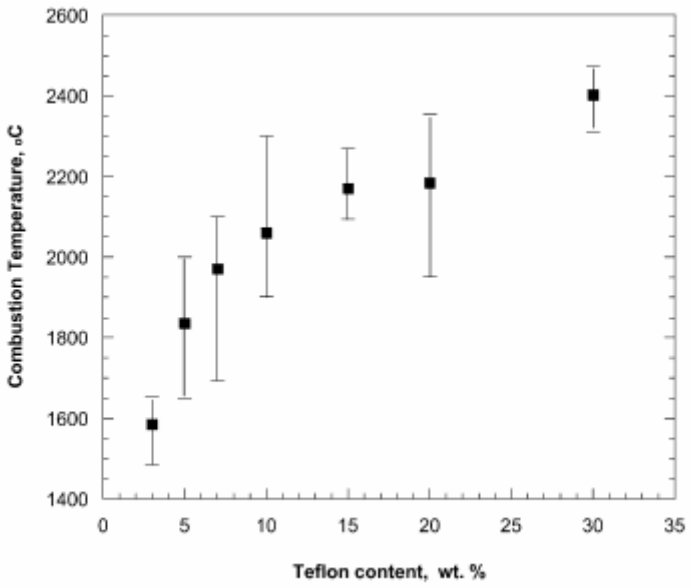

Figure 2-13: Effect of Teflon content on combustion temperature [30]

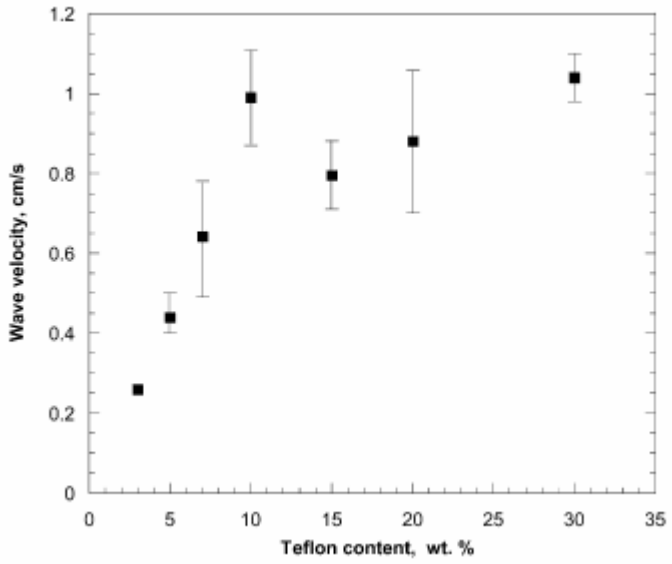

Figure 2-14: Effect of Teflon content on reaction propagation velocity [30]

The propagation of shock-induced chemical reactions in energetic materials consisting of nano Al particles in Teflon, a polymer oxidizer, was studied by Yang *et al.* [32]. Flash heating of the nanoparticles produced an Al vapor that reacted with the oxidizer shell. The energy then drove a spherical shock front that caused shock-induced chemical decomposition of the polymer.

2.3 Structural/Mechanical Properties of Multifunctional Structural Energetic Materials

Besides energetic properties, the mechanical behavior (under static and dynamic loading) of reinforced composites is another essential element in the design of MESMs. Static mechanical properties can be obtained by conventional mechanical testing approaches. The reverse Taylor anvil-on-rod impact test can be used as a method of determining the dynamic mechanical properties under a range of strain rates (10^2-10^5 s^{-1}). A brief description of the test method and its modifications employing imaging of transient states will be described next.

2.3.1 Taylor Test and Modifications

In 1948, Taylor [33], Whiffin [34], and Carrington and Gayler [35] reported a test aimed at determining the dynamic yield stress of materials deformed at high strain rates (up to 10^4 s^{-1}) since it is known that metals may be subjected momentarily to stresses far exceeding their static yield stress. This experiment, referred to as the Taylor impact test, is performed by striking a specimen against a rigid anvil. The deformed specimen geometry and striking velocity, as shown in Figure 2-15, are analyzed to give an estimate of the flow stress and the average dynamic compressive yield strength.

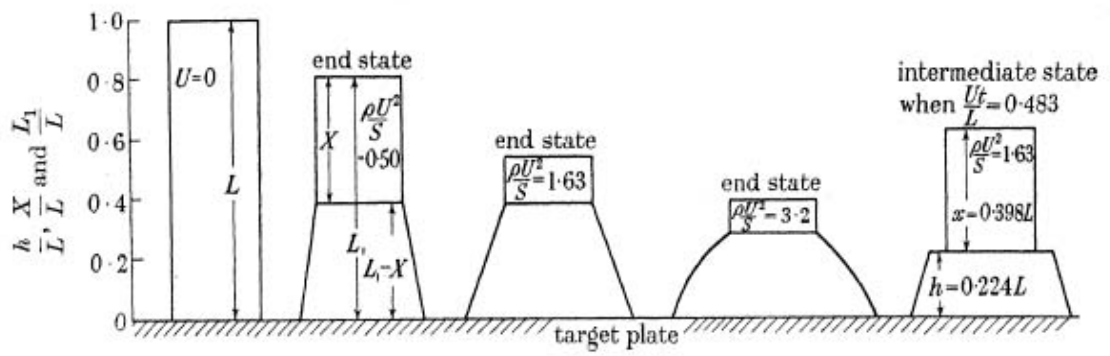

Figure 2-15: Schematic of a cylindrical projectile with flat surfaces fired at a target plate at a speed U, as in the Taylor impact test [33].

During the Taylor test, a high stress occurs at the site of the projectile impact. If these stresses exceed the elastic limit of the material, a plastic front moves back into the projectile. The portion of the projectile that is still elastic flows into the plastic front, fails by plastic flow, and shortens as material flows radially out. The elastic portion of the projectile can support stresses no greater than the elastic limit. These stresses, which move between the plastic front and the free end, decelerate the projectile [36]. Therefore, deceleration of the projectile is due to material strength; the greater the strength of the material, the faster the deceleration for a given impact velocity [36, 37].

Based on computer simulations, Wilkins *et al.* [36] found that deceleration of the cylinders is independent of specimen diameter. The time required to completely decelerate the sample from a specific impact velocity is directly proportional to the original length of the specimen. The strain rate was also found to vary linearly with impact velocity. Wilkins *et al.* [36] also verified Whiffin's [34] finding that yield strength is nearly independent of impact velocity. Wilkins *et al.* determined that the plastic wave front is actually closer to the rigid boundary than was assumed in Taylor's

original analysis, so he modified Taylor's analysis accordingly. The scaling law that relates deceleration to strength, density and impact velocity follows. The rate of decrease of the cylinder of length L is given by:

$$\frac{dL}{dt} = -U \qquad (2\text{-}1)$$

where U is the impact velocity. The deceleration of length L is:

$$\sigma_y = -\rho_0 L \frac{dU}{dt} \qquad (2\text{-}2)$$

where σ_y is the material yield strength and ρ_0 is the projectile material density. Combination of these two equations gives

$$\frac{dL}{L} = \frac{\rho_0 U}{\sigma_y} dU \qquad (2\text{-}3)$$

$$[\ln L]_{L_0}^{L_f} = \left[\frac{\rho_0 U^2}{2\sigma_y} \right]_U^0 \qquad (2\text{-}4)$$

$$\ln \frac{L_f}{L_0} = -\frac{\rho_0 U^2}{2\sigma_y} \qquad (2\text{-}5a)$$

$$\frac{L_f}{L_0} = \exp\left(-\frac{\rho_0 U^2}{2\sigma_y} \right) \qquad (2\text{-}5b)$$

Equation 2-5 states that the only material properties responsible for the ratio of final to initial length of the specimen are density and yield strength [36].

Taylor's analysis, as well as several others, employs a rigid-plastic idealization of the stress-strain curve. Flow stress is the only parameter considered in this analysis, therefore it is lacking the ability to provide a detailed description of material properties since parameters such as strain and strain rate are absent. In order to account for these

missing parameters, House *et al.* [38] developed a method of analysis using high-speed digital photography to capture transient deformation states to estimate the stress-strain and stress-versus-strain rate curves for each material tested. House used Taylor's definition of strain, *e*:

$$e = 1 - \frac{A_0}{A} \qquad (2\text{-}6)$$

which closely approximates the axial strain everywhere except the anvil face. A_0 is the cross-sectional area of the specimen prior to impact and A is the current area at the time of *e*. A schematic illustration showing the dimensions of the projectile used to describe strain at various times during a Taylor impact test is shown in Figure 2-16.

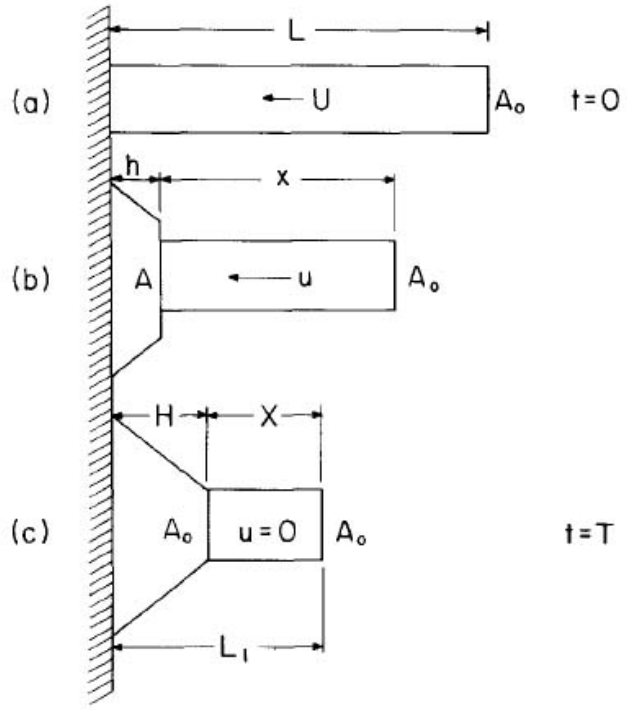

Figure 2-16: Schematic showing a projectile impacting a rigid anvil, as in the Taylor impact test [39]. This illustration shows the area dimensions used to describe strain of the projectile in Equation 2-6.

The first step in using House's analysis to obtain a stress-strain curve is to measure the change in length of the specimen, which enables the back end speed, u, to be calculated by

$$u = \frac{l_1 - l_2}{t_1 - t_2}, \qquad (2\text{-}7)$$

where l_1 and l_2 are specimen lengths at times corresponding to t_1 and t_2. These values can be obtained from a plot of specimen radius vs. axial position, an example of which is shown in Figure 2-17.

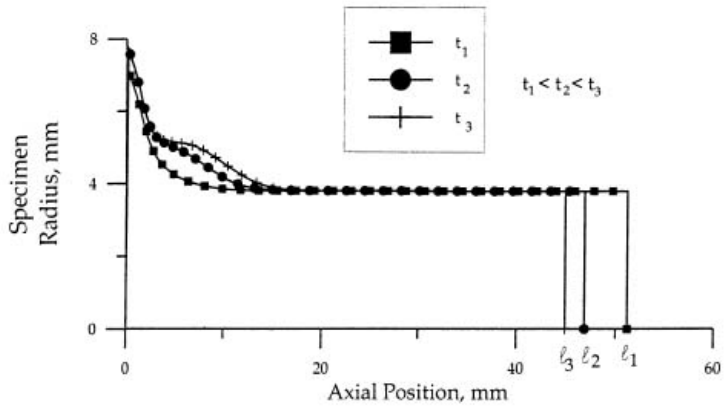

Figure 2-17: Plot of specimen radius vs. axial position generated from images at three different times during a Taylor impact experiment.

The next step in the construction of the stress-strain curve is to determine a series of plastic wave speeds, v, from a plot of strain vs. axial position, which is shown in Figure 2-18. To do this, a strain is selected and the corresponding axial positions for two different time profiles, t_1 and t_2, are denoted as h_1 and h_2. With respect to the anvil face, this specific strain has propagated a distance $h_2 - h_1$ during the time interval $t_2 - t_1$. In the following equation, v is the average Eulerian wave speed for the specific strain level over the time interval from t_1 to t_2.

$$v = \frac{h_2 - h_1}{t_2 - t_1} \qquad (2\text{-}8)$$

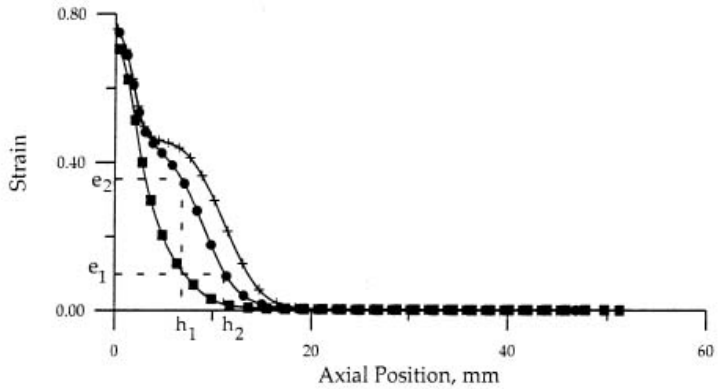

Figure 2-18: Plot of strain vs. axial position generated from images at three different times during a Taylor impact experiment.

An approximation to the strain rate can be determined by

$$\frac{de}{dt} \approx \frac{e_2 - e_1}{t_2 - t_1} \qquad (2\text{-}9)$$

however e is a Lagrangian strain measure which is embedded in the material, and the material located at h_1 at time t_2 is different than that at time t_1.

To determine the stress, Taylor's original approach was used. From conservation of mass,

$$A_0(u+v) = Av \qquad (2\text{-}10)$$

and impulse-momentum considerations give

$$\rho A_0(u+v)u = \sigma(A - A_0) \qquad (2\text{-}11)$$

where ρ denotes the density of the material and σ is a compressive stress magnitude. Simplifying these two equations gives

$$\sigma = \rho(u+v)v \qquad (2\text{-}12)$$

In combination with Equations 2-7 and 2-8, a stress σ is associated with each strain e. These stress-strain pairs can then be plotted from the measured values of diameter as a

function of axial length from images obtained during the Taylor impact test [38]. The plots of stress vs. strain and strain rate vs. strain are shown together in Figure 2-19.

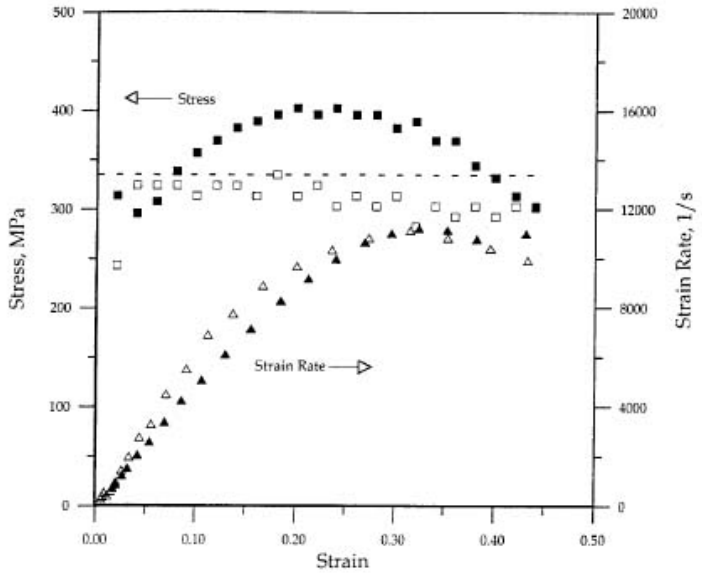

Figure 2-19: Plot of stress vs. strain and strain rate vs. strain generated from images taken at three different times during a Taylor impact experiment.

2.3.2 Dynamic Properties of Polymer Composites

The response of polymeric materials to shock loading has become increasingly important since they are used as binders in composites and energetic materials and as adhesives during the assembly of targets for shock wave experiments [40].

The dynamic moduli of a polymeric matrix, in which metal powders have been dispersed, depend on the stress/strain fields developed around the individual particles under dynamic loading. These stress/strain fields depend on (i) the shape of the particles and the distribution of the matrix, (ii) the particle sizes as compared with the length of the

stress wave, (iii) the interaction between the stress/strain fields of neighboring inclusions, (iv) stress fields due to polymerization shrinkage and (v) thermal stress fields due to different thermal expansion coefficients of the constituents at elevated temperatures. The nature of the interfacial bond between matrix and filler particles is also important. Perfect adhesion is often assumed in analysis, but real composites rarely exhibit this, and cracks, voids and flaws distort the stress/strain fields developed in the composite. An impedance mismatch ($\rho_2 c_2 >> \rho_1 c_1$), which is common in metal-filled plastics tends to create situations similar to those seen with imperfect bonding. A stress wave practically does not enter the reinforcing particle, but circumnavigates it. In this case, the filler only perturbs the stress fields by restraining the matrix as long as the strain rate is sufficiently high. Energy dissipation occurs primarily in the viscoelastic matrix and depends on the strains developed. Addition of a non-dissipative filler decreases the effective dissipation volume, but creates additional strain fields, therefore increasing damping [12].

The dynamic behavior of composites is dependent on all of its components. The failure or energy absorption modes of a composite subjected to impact can take the form of delamination, matrix shear failure, fiber/matrix debonding and fiber pullout [41], as shown in the schematic in Figure 2-20. As the impact velocity increases, the energy transfer rate and strain rate increase. The composite has a maximum energy absorption capacity, so if the velocity is too high, the energy transfer is faster than the energy absorption by strain. The energy that the composite absorbs by means of strain decreases as strain rate increases. Therefore, at a high strain-rate, the impact energy that has not been absorbed by strain must be consumed by another method such as delamination. At high velocity impact, these failure modes dominate composite strain.

For this reason, energy absorption capability is more important than other composite design parameters [42].

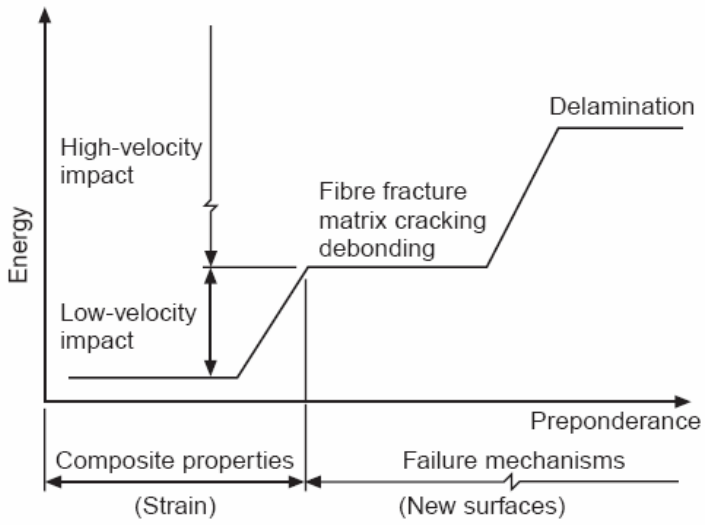

Figure 2-20: Schematic showing composite energy behavior and failure mechanisms [42]

In a study of plastic bonded explosives, Christopher *et al.* [43] stated that there is a critical velocity below which no permanent macroscopic deformation occurs. Above this velocity, radial cracks originate on the outer edges and propagate toward the center. At higher velocities, these cracks are joined by a circular crack that forms around half the radius of the cylinder [44]. In this study by Roessig *et al.* [44], microstructural damage observed in the samples consisting of explosives in a polymer binder consisted of crystal fracture, crystal twinning, crystal/binder debonding, and binder tear.

PTFE is typically a ductile polymer, but it undergoes an abrupt ductile-brittle transition at moderate impact velocities. Rae *et al.* [45] examined the effect of the pressure-induced phase transition in PTFE on the failure of Taylor impact cylinders. The

phase transition occurs at approximately 0.65 GPa (134±1 m/s) at 21 °C, but the transition velocity is inversely related to temperature, as shown in Figure 2-21. The temperature of the Taylor cylinders in this experiment were varied and this showed that the phase transition is likely to be involved in failure of the rods since the critical velocity increases as temperature decreases, despite the decreasing fracture toughness.

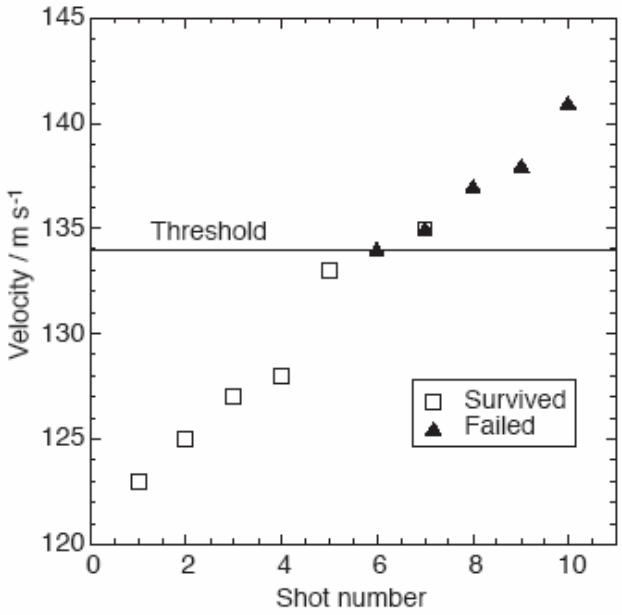

Figure 2-21: Fracture velocity threshold map for Teflon [45], showing a ductile-brittle transition at a critical velocity of 134±1 m/s at room temperature.

Millett *et al.* [40] investigated the response of an epoxy resin to planar shock waves. Shear strength was shown to increase with longitudinal stress, and lateral stresses were shown to decrease behind the shock front, implying an increase in the strength of the material during shock loading. This could be a result of the viscoplastic nature of epoxy based resins.

A study by Paipetis *et al.* [46] investigated the dynamic properties of an epoxy matrix filled with Al or Fe particles. They concluded that the introduction of the metal powder filler led to a reinforcing effect due to a restraining of the matrix, while the matrix was the principal load-carrying element. Temperature was found to affect the modulus of the composites in the same way as it affects the modulus of the matrix alone. Loss factor was negligibly increased by the addition of metal powder at low temperatures, but dramatically increased at high temperature.

2.4 Motivation and Rationale

The literature review of the Ni-Al intermetallic systems, Teflon and Epoxy polymer binders, energetic and reactive properties, and dynamic mechanical properties will aid in design and analysis of MESMs. It is known that reactivity of intermetallic forming powder mixtures is influenced by volume fraction, powder morphology, particle size, and shock loading conditions, among other factors. Mechanical properties of the materials of interest are also dependent on variations in the aforementioned factors, and it is known that material properties vary with strain rate. New methods to test materials at high strain rates can be employed to characterize materials throughout a range of strain rates. Modifications to the Taylor impact test involving high speed digital photography have allowed for analysis of dynamic material properties. All of the factors discussed in the literature review can be combined in an effort to fabricate and characterize the reaction behavior and static and dynamic mechanical properties of a multifunctional material with desirable structural and energetic properties.

CHAPTER 3

OBJECTIVES AND APPROACH

3.1 Objectives

The research conducted in this study is part of a collaborative multi-university research project aimed at design, fabrication and understanding of multifunctional energetic structural materials (MESMs). The goal of the work conducted in this thesis is to investigate Ni+Al+polymer composites as potential candidate MESMs. The more specific objectives include:

1) Processing of Ni and Al powder mixture composites by static pressing with Teflon or by casting/curing with epoxy
2) Physical, mechanical and microstructural characterization of as-processed Teflon-pressed and epoxy-cast materials
3) Characterization of the reaction energetics of these composites using differential thermal analysis (DTA) coupled with x-ray diffraction analysis to identify phases formed corresponding to exothermic events detected in the DTA
4) Dynamic mechanical behavior characterization of the Ni+Al+epoxy composites using reverse anvil Taylor impact tests coupled with real-time high-speed digital photography and velocity interferometry measurements

3.2 Experimental Procedures

3.2.1 Processing of Ni+Al+Polymer Composites

Reinforced polymer composite materials, consisting of Ni and Al powders and a polymer binder, were processed by means of static pressing with Teflon, or casting and curing with epoxy.

3.2.1.1 Powder Preparation

Dry powder mixtures of 50vol% (76.6wt%) Ni and 50vol% (23.4wt%) Al/nano-Al were prepared in a glove box (Labconco; Kansas City, MO) and then removed in a covered container. Table 3-1 describes the characteristics of the various as-received powders. The Ni and Al powder mixture was next placed into a Twin Shell Dry V-Blender (The Patterson Kelley Company, Inc.; East Stroudsburg, PA) for 24 hrs. To mix the Ni-Al/nano-Al mixtures with Teflon, the desired mass of Teflon powder was combined (10vol% or 3.95wt%) with the Ni-Al/nano-Al and placed in a covered container and mixed again in a V-Blender for 24 hrs.

Table 3-1: Characteristics of commercially purchased powders.

Material	Particle Size	Purity	Oxide Layer	Manufacturer	Location
Nickel	-325 mesh (<45 μm)	99.9%	none	Cerac	Milwaukee, WI
Aluminum	-325 mesh (<45 μm)	99.5%	none	Cerac	Milwaukee, WI
Nano Aluminum	Avg. 56.3 nm	72.7 wt% Al	2.1 nm	Technanogy	Irvine, CA
Zonyl MP 1100 PTFE	Avg. 4 μm		none	DuPont	Wilmington, DE

3.2.1.2 Static Pressing

Samples containing only Ni and Al/nano-Al powders, as well as samples containing Teflon powder were made by static pressing. Sample pressing was done using a 12 ton capacity Carver Press (Fred S. Carver Hydraulic Equipment; Menomonee Falls, WI) in increments of 5,000 lbs, holding for one minute at 5,000 lbs and then holding for five minutes at 10,000 lbs.

A ¼" diameter die with a 3" barrel and interchangeable plungers ranging in length from 2" to 3.5" was used. Photographs of the die set-up and the press are shown in Figure 3-1 and Figure 3-2, respectively. As shown in Figure 3-1, four guide rods were secured in both the top and bottom plates in order to insure that the plunger and barrel remained aligned and came together correctly. For larger samples, the powder was added in three stages to reduce the density gradient, so it was necessary to be able to remove the plunger. To do this, the base plate was removed and the four remaining guide rods were introduced through the bottom plate and screwed to the top plate. This allowed the guide rods to be pressed apart leaving the die in an open position, as shown in Figure 3-3. More powder could then be added into the barrel and the pressing resumed. To remove the sample, the base plate was removed and the sample was pressed all the way out through the barrel.

A variety of pressed samples were prepared. The desired lengths of the samples ranged from 2 mm for DTA/microscopy/XRD analysis to 2 in. for reverse anvil Taylor impact tests.

Figure 3-1: Photograph of ¼” die in closed position.

Figure 3-2: Photograph of ¼” die in Carver Press.

Figure 3-3: Photograph of ¼" die with all 8 guide rods used to open die.

3.2.1.3 Epoxy Cast-Curing

Samples of Ni+Al mixtures were also made by means of epoxy casting and curing. To prepare these samples, a mixture of Ni and Al/nano-Al powders was heated in an open container in a 120 °C furnace for several hours to eliminate any moisture. Simultaneously, Epon® Resin 826 (Miller-Stephenson; Danbury, CT) was heated at 120 °C to decrease its viscosity. After heating, the desired amount of Ni-Al/nano-Al powder was measured out and placed in a plastic container. The desired amount of resin (92.3wt% of epoxy) was then added to the powder mixture. The resin and powder were mixed for about 3 mins., using a mixing blade mounted on a drill. The mixture was then placed back into the 120 °C furnace (Fisher Oven) for about 15 mins. to aid the mixing by decreasing the viscosity of epoxy. After the resin and powders were fully mixed, the Diethanolamine hardener (Sigma-Aldrich; St. Louis, MO) (7.7wt% of epoxy) was added to the mixture and blended using the home-made mixing device. The mixture was again placed in the furnace for about 15 mins. If this mixture was not fluid enough that it could

be poured out of the container, a small amount of Toluene anhydrous, 99.8%, (Alfa Aesar; Ward Hill, MA) was added as a solvent and evaporated later. After the addition of Toluene, the mixture was placed back in furnace for an additional 15 mins. Next, the mixture was degassed in a desiccator for about 5 mins. (until a pressure of ~1-2 torr was achieved) to remove air bubbles and then it was placed back in the furnace for abut 30 mins., taking care not to stir it and introduce new air bubbles. Finally, the mixture was poured into molds (coated with grease (Dow Corning Corporation; Midland, MI) on the inside) of 0.6" diameter and 6" length, and placed in a 70-80 °C furnace (National Appliance Company) for 48 hrs. to cure. After the samples had cured, they were removed from the molds. Figure 3-4 shows an example of a sample in the mold after curing. The samples were then cut and machined into various sized rods for testing.

Figure 3-4: Photograph of Ni-Al + epoxy sample in open mold after curing.

3.2.1.4 Characterization of As-Processed Materials

After processing, all materials were characterized by density measurements and scanning electron microscopy. Density measurements were performed according to

ASTM Standard C914-95: Standard Test Method for Bulk Density and Volume of Solid Refractories by Wax Immersion [47]. This standard allows for determination of densities of samples which were slightly porous, without letting water permeate into the samples as in the traditional Archimedes method.

Five samples of each material were necessary for these measurements. The initial weight, W, of each sample was obtained from a balance with 0.1 mg resolution. Each sample was coated in paraffin wax (Gulf Oil Corporation; Houston, TX), taking care not to entrap any air bubbles. Next, the wax-coated sample weight, P, was obtained, followed by the weight, S, of the wax-coated sample suspended in water, which was obtained by placing the wax-coated sample in a wire dish hanging in distilled water. The temperature of the water was recorded and used to correct for the density of water, as a function of temperature.

The volume, V_1, of the sample including the wax was calculated as follows:

$$V_1 = \frac{P - S}{\rho_{H_2O}} \qquad (3\text{-}1)$$

The volume, V_2, of the wax coating was calculated as follows:

$$V_2 = \frac{P - W}{K}, \qquad (3\text{-}2)$$

where K = the density of the paraffin wax, 0.895 g/cm^3. The volume, V, of the sample is then obtained as:

$$V = V_1 - V_2 \qquad (3\text{-}3)$$

The bulk density, B, of the specimen is equal to the quotient of the wax coated weight and the volume of the sample:

$$B = \frac{W}{V} \qquad (3\text{-}4)$$

These measured bulk density values are reported in units of g/cm^3 to two decimal places.

Scanning Electron Microscopy was performed using a LEO 1530 (JEOL USA, Inc.; Peabody, MA) thermally-assisted field emission (TFE) scanning electron microscope (SEM). This microscope yields 1 nm resolution at 20 kV and 3 nm at 1 kV, and has an operating voltage range (200 V – 30 kV). The instrument also has a thin window energy dispersive spectrometer (EDS), for microanalysis.

SEM analysis was used to get a qualitative idea of particle distribution in each type of fabricated sample, as well as to compare the fracture surfaces of the different materials after mechanical testing.

3.2.2 Characterization of Reaction Energetics

To characterize the reaction energetics of the processed materials, differential thermal analysis was used to detect any endo- or exothermic reaction events. Samples were recovered following heating through completion of specific exothermic events and analyzed using x-ray diffraction to determine the reaction products.

Differential Thermal Analysis (DTA) was performed using a DTA 7 (Perkin Elmer; Boston, MA) on composites consisting of various combinations of Ni, Al, nano-Al, Teflon and epoxy. All of the starting materials were analyzed separately as well as in the mixtures used to make samples. Statically pressed and cast samples were also analyzed. The samples used were approximately 20 mg, and were covered with Al_2O_3 powder (Perkin Elmer; Boston, MA). Prior to each test, the furnace was set to 100 °C under flowing Ar gas. The tests were conducted up to 800 °C at a heating rate of 10

°C/min in a 4.948% H_2 + balance argon (Airgas; Radnor, PA) environment. The data from these tests were analyzed using Pyris Software (Perkin Elmer; Boston, MA), which generates plots of heat flow (measured as ΔT associated with temperature differentials between the reference and sample) vs. temperature or time.

X-Ray Diffraction (XRD) analysis was performed on an X-Pert PRO MPD (PANAlytical; Natick, MA) using a tungsten source and a copper target. Whenever possible, solid samples were ground into powder using a mortar and pestle. The powder was placed on a thin layer of grease on a zero-background silicon wafer (PANAlytical; Natick, MA) which was secured in a sample holder (PANAlytical; Natick, MA). Scans were performed from 20-100° 2-Theta. XRD data was analyzed using X'Pert High Score (PANAlytical; Natick, MA) software. For each scan, background was determined and a peak search was performed. Peaks were then matched using restrictions based on the sample, and by comparing d-spacings and peak intensities.

3.2.3 Mechanical Properties Characterization

To characterize the mechanical properties of the processed materials, both static and dynamic tests were performed. Static compression tests were performed to determine the elastic modulus and compressive yield strength. Dynamic reverse anvil Taylor impact tests were performed to determine dynamic yield stress and elastic wave speed. Prior to measurement of mechanical properties, theoretical values of elastic properties were calculated for each combination of fabricated material using literature values for Ni, Al, epoxy and Teflon [48] and the Rule of Mixtures. The literature values for wave speeds were used in conjunction with the following equations [49] to obtain

Elastic Modulus, E, Shear Modulus, μ, and Poisson's Ratio, ν. These values are listed in Table 3-2.

$$C_l = \left(\frac{\lambda + 2\mu}{\rho} \right)^{1/2} \qquad (3\text{-}5)$$

$$C_s = \left(\frac{\mu}{\rho} \right)^{1/2} \qquad (3\text{-}6)$$

$$\lambda = \frac{Ev}{(1+v)(1-2v)} \qquad (3\text{-}7)$$

$$\mu = \frac{E}{2(1+v)} \qquad (3\text{-}8)$$

Table 3-2: Theoretical values of elastic properties determined by the Rule of Mixtures.

Material	**Elastic Modulus (GPa)**	**Shear Modulus (GPa)**	**Bulk Modulus (GPa)**	**Poisson's Ratio**
Nickel	203.86	77.87	177.89	0.309
Aluminum	70.78	26.45	72.82	0.338
Teflon	1.04	0.36	2.78	0.438
Epoxy	4.40	1.60	6.07	0.379
Ni+Al	105.08	39.49	103.34	0.323
Ni+Al+20wt% epoxy	7.64	2.77	10.41	0.352
Ni+Al+30wt% epoxy	6.32	2.29	8.65	0.359
Ni+Al+10vol% Teflon	9.55	3.33	22.38	0.332

Static compression tests were performed according to ASTM Standard D 695-02a: Standard Test Method for Compressive Properties of Rigid Plastics [50]. Test specimens were in the form of cylindrical rods with a length to diameter ratio of 2:1. The cast epoxy based specimens were 0.6" in diameter and 1.2" in length, whereas the

pressed specimens were 0.25” in diameter and 0.5” in length. Tests were performed on five test specimens of each material.

Compression tests were performed using the SATEC^{TM} Universal Materials Testing Machine (Instron; Canton, MA) with a 22,000 lb loading capacity. Before each test started, the load cell was zeroed and brought down to the top surface of the sample with <100 lb of pre-load. The load was applied at a rate of 0.585 lb/min. and was stopped when the sample reached ~80% of its original length. The compliance of the load cell was tested by bringing the cross-hairs together and allowing them to compress. Data were recorded as load-position pairs, and converted to engineering stress-strain data. The compliance data was plotted as position vs. load and the resulting curve was fit with a polynomial. The resulting polynomial was subtracted from the load-position data for each sample before converting it to stress vs. strain.

3.2.4 Dynamic Mechanical Testing: Reverse Taylor Anvil Impact Tests

Reverse Taylor anvil impact tests were performed using a Helium-driven 80 mm barrel gas gun at velocities ranging from 61-152 m/s. The anvil projectiles consisted of a 2024 T351 Al 80 mm diameter sabot with a maraging steel flyer plate (~0.25” thickness, 3” diameter) secured to the front surface. Test specimens for Taylor Tests were in the form of cylindrical rods, with a 0.5” diameter and 2” length. The flat surfaces of the samples were lapped to < 0.0001” tilt to insure planar impact, and then polished with 15 μm diamond slurry. Each sample was mounted in a PMMA target ring using 5 minute epoxy such that about ¼ of the sample length was on the back side of the target ring, and the remaining ¾ was on the impact side. Two self-shorting crush pins (Dynasen; Goleta, CA) were used as trigger pins, and were mounted on the target about 1” away from the

sample to insure that both would be hit by the flyer plate (3" diameter) for trigger upon impact. One crush pin was used to trigger the camera, and the other to trigger the VISAR oscilloscope. The distance between the tip of each crush pin and the sample face was measured carefully using depth micrometers. Figure 3-5 show the set-up of the sample and trigger pins, and Figure 3-6 shows a photograph illustrating how the target is mounted in the experiment chamber.

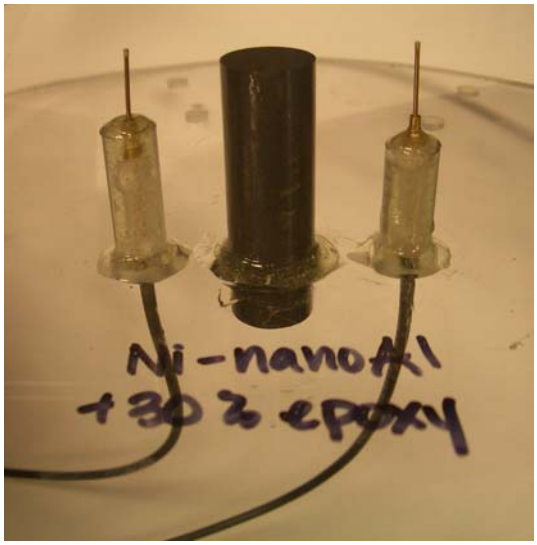

Figure 3-5: Photograph of sample and crush pins mounted in PMMA target ring.

A velocity measurement pin block with 5 pins, separated by a pre-measured distance, was mounted on the muzzle, as can be seen in Figure 3-6. The first pin was used to trigger the flash, and the remaining four were used to determine the impact velocity, based on the electrical signal recorded when the projectile grounds each pin. The distances between the pins were measured using depth micrometers. A schematic of the entire set-up for reverse Taylor anvil impact tests is shown in Figure 3-7.

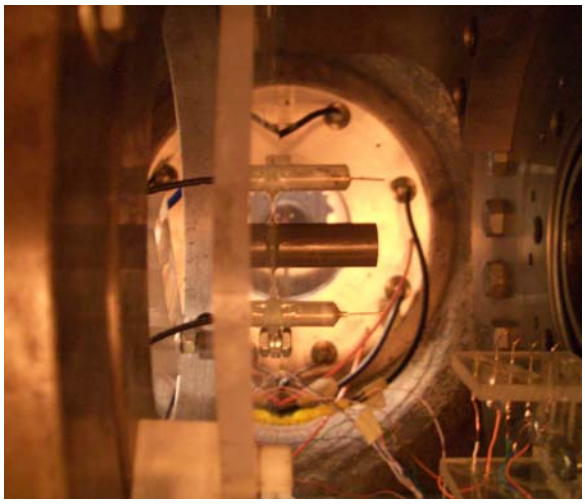

Figure 3-6: Photograph (from the flash side) of the target ring with sample and crush pins mounted in the gas gun chamber. The velocity block can be seen on the right.

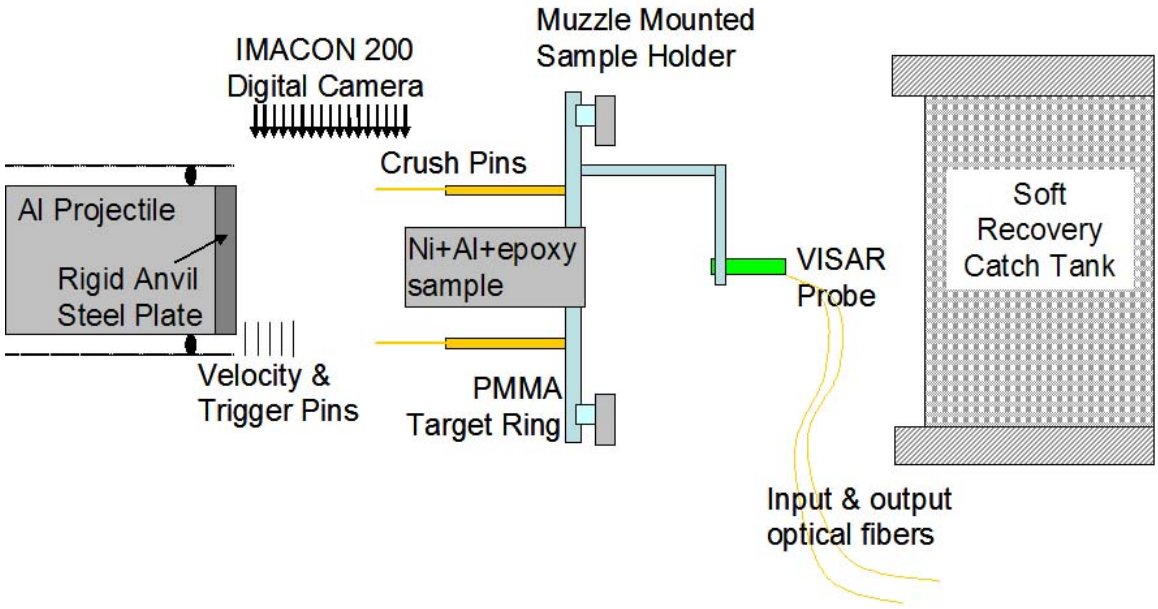

Figure 3-7: Schematic of reverse anvil Taylor impact test setup showing the sample and gas gun hardware with triggering and velocity measurement mechanisms, as well as image capturing tools.

An Imacon-200 High Speed Digital Camera (Imacon; Redmond, WA) was used to capture images of the deformation of the specimen upon impact with the projectile. The placement of the camera can be seen in the schematic in Figure 3-7. The camera has a capacity of recording 16 frames at a speed of 200,000,000 frames per second. These 16 image frames were timed based on impact conditions: one frame immediately before impact, one at impact, and the remaining 14 spread out until the projectile was about halfway through the sample length. Timing was essential since frames were only useful from the time the projectile impacted the sample until fracture occurred or the back surface of the sample moved out of the frame.

In order to analyze the deformation response using the House Analysis, the profile of the sample in each frame, an example of which is shown in Figure 3-8, was isolated to obtain its profile, as illustrated in Figure 3-9, using Adobe Photoshop (Adobe; San Jose, CA). Next, ImageJ software (NIH; Bethesda, MD) was used to create a vertical profile along the entire length of the sample, as shown in Figure 3-10. The values output by ImageJ were used in a spreadsheet for further calculations.

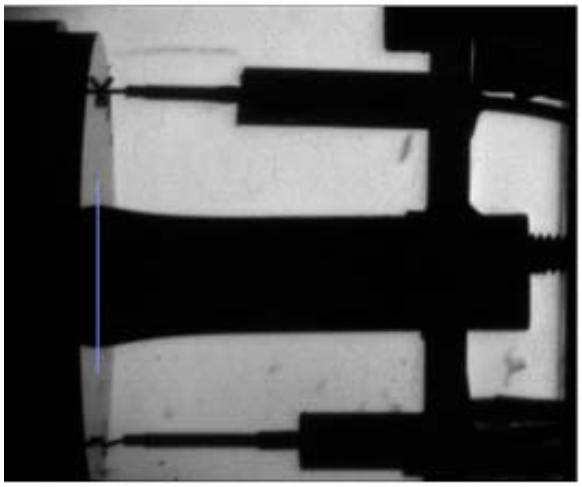

Figure 3-8: Example of an image frame captured during transient deformation occurring during a reverse anvil Taylor impact test.

Figure 3-9: The profile of the deforming sample shown in Figure 3-8 isolated in Photoshop for use in the House analysis.

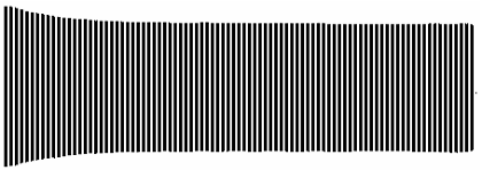

Figure 3-10: Vertical profile, done using ImageJ software, of the isolated sample shown in Figure 3-9.

The velocity interferometer system for any reflector (VISAR) (Valyn International; Albuquerque, NM) was used to obtain the velocity of the back surface of the sample during impact. Sample preparation for VISAR required obtaining a reflective

surface on the back of each sample. This was obtained on all Ni and Al-containing samples by polishing the back surface. In the case of the 100% epoxy sample, a 10 mm diameter glass window was polished, sputter coated with gold, and secured to the back surface of the sample rod with epoxy, as shown in Figure 3-11. The VISAR laser beam passed through the glass and reflected off of the gold coating, which was in close proximity to the free surface of the epoxy rod. In the case of the Ni- and Al-containing samples, the VISAR laser beam reflected directly off of the back surface of the sample. The surface treatment of each sample dictated the amount of light that was reflected, and therefore collected by the output fiber. The more reflective the surface was, the better the signal was. Table 3-3 lists the signal strength attained for each shot.

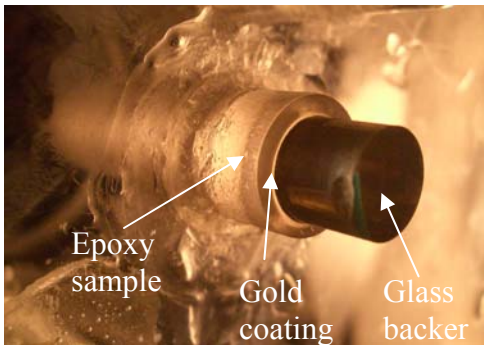

Figure 3-11: Photograph of a glass backer window and gold sputter coating layer on epoxy rod for VISAR.

Table 3-3: VISAR signal attained for each shot.

Shot	Sample	Signal Achieved
0423	Ni-nanoAl + 30wt% epoxy	~40 mV
0429	Ni-Al + 20 wt% epoxy	~40 mV
0430	Ni-nanoAl + 20wt% epoxy	~150 mV
0431	Ni-nanoAl + 30wt% epoxy	~25 mV
0434	Epoxy	~150 mV
0501	Epoxy	~200 mV

To set up the VISAR system, a laser supplied a signal light (0.1-0.5 W) and a Valyn fiber optic system collected the light into an optical fiber, which transported it to a mirrored surface used to find the fringes. After the fringes were found, fringe viewers were placed over the beam splitters and the signal was optimized. The fringe viewers were then removed and the signal was optimized again by adjusting the fibers over the collimation lenses. The ramp driver piezoelectric mirrors were then adjusted to optimize the signal again. The photomultiplier units were used to adjust the signal to the desired amplitude (<30mV). This process of signal optimization was repeated for a diffuse surface, while also optimizing the probe by adjusting its tilt. The probe was then mounted on the target ring with a 30 mm standoff distance from the back surface of the sample, centered as well as possible. The signal optimization was repeated again for the sample's back surface and the laser intensity was increased up to 1.0 W if necessary. A photograph of the back of the sample taken during setup of a reverse anvil Taylor impact experiment showing the VISAR optical fibers and probe is shown in Figure 3-12, and can be seen in the schematic in Figure 3-7. Table 3-4 summarizes the sample preparation and set-up details necessary for VISAR during each shot.

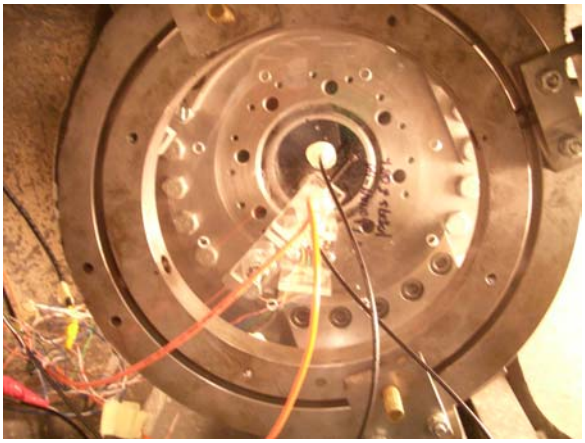

Figure 3-12: Photograph from back of sample showing VISAR optical fibers and probe.

Table 3-4: Sample preparation and set-up details for VISAR

Shot	Sample	Surface Treatment	Window	VPF Constant
0423	Ni-nanoAl + 30wt% epoxy	Lap & Polish (15 μm diamond)	None	94.8 m/s
0429	Ni-Al + 20 wt% epoxy	Lap & Polish (15 μm diamond)	None	94.8 m/s
0430	Ni-nanoAl + 20wt% epoxy	Lap & Polish (15 μm diamond)	None	94.8 m/s
0431	Ni-nanoAl + 30wt% epoxy	Lap & Polish (15 μm diamond)	None	94.8 m/s
0434	epoxy	Lap, epoxy to polished glass window with gold sputter layer	Glass	91 m/s
0501	epoxy	Lap, epoxy to polished glass window with gold sputter layer	Glass	91 m/s

Two optical fibers were run to the back of the sample: one input and one output. The input fiber carried a laser to the back of the sample, and the fiber optic system collected some of the light reflected by the sample into the output fiber and transported it back to the VISAR interferometer. When the laser light was reflected from the specimen surface, it underwent a doppler shift in frequency proportional to the specimen's velocity.

The interferometer changed the doppler shift in frequency into light fringes, which are oscillations between bright and dark output from the interferometer. The changes in light amplitude were transduced into changes in electrical voltage by the photomultiplier units, and the electrical voltage histories were recorded by digitizing oscilloscopes. The schematic shown in Figure 3-13 describes the mechanisms of the VISAR velocity interferometry system [51]. For each shot, the two electrical voltage traces were output and these were analyzed in PlotData to obtain the velocity trace, as seen in the schematic below.

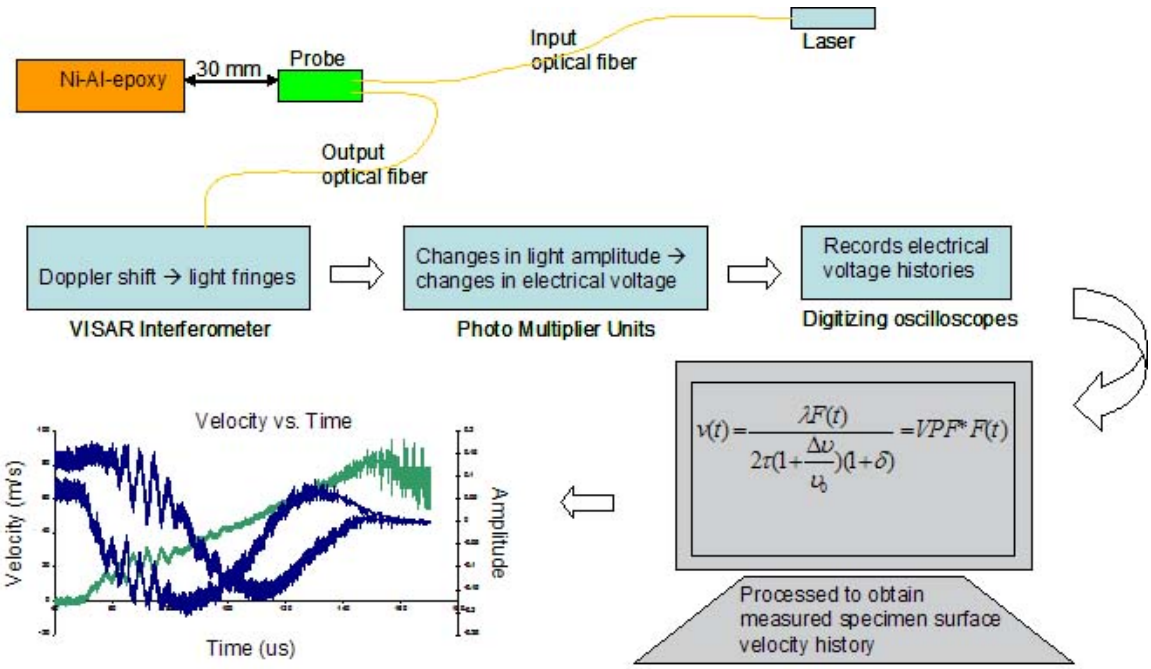

Figure 3-13: Schematic of VISAR system

The recorded voltage histories were processed to obtain the measured sample surface velocity history using PlotData software (Sandia National Laboratories;

Albuquerque, NM). The two data traces were input as *.wfm files of amplitude-time data and converted to a plot of velocity vs. time by adjusting the velocity per fringe (VPF) constant and centering the Lissajous.

CHAPTER 4

RESULTS

In this chapter, the processing and characteristics of Ni-Al based multifunctional structural energetic reinforced polymer composite materials will be described. The results from the energetic/reactive response characterization based on DTA and XRD analysis will also be presented, along with the static and dynamic mechanical properties of the fabricated structural energetic materials.

4.1 Processing and Initial Characterization

Multifunctional energetic structural materials, consisting of Ni+Al and Teflon or epoxy, were fabricated by static pressing and casting, repsectively. In addition to density measurements, XRD and SEM analyses were used to qualitatively characterize the composition and distribution of constituents as well as the characteristics of fracture surfaces of intentionally statically fractured as-processed materials. Samples attained from the cast/pressed rods were used to evaluate the reactive and mechanical properties of the fabricated multifunctional energetic structural materials.

Commercial Ni and Al/nano Al powders were mixed in a 1:1 volumetric ratio (76.66wt% Ni, 23.34wt% Al) using a V-blender. In one batch of Ni+Al powder mixtures, 10vol% Teflon powder was added, and the powders were pressed into cylindrical rods of 0.25" diameter and ~1" length. For other samples, 20 or 30wt% epoxy (55.7 or 68.3vol%) was added and the mixtures were cast and cured into cylindrical rods of 0.6" diameter. Table 4-1 below lists corresponding volume and weight percentages for all fabricated samples.

Table 4-1: Volume and weight percentages of components of all fabricated samples.

Material	**Vol% Ni**	**Wt% Ni**	**Vol% Al**	**Wt% Al**	**Vol% Binder**	**Wt% Binder**
Pressed Ni+Al	50	76.66	50	23.34	0	0
Pressed Ni+Al+ 10vol% Teflon	45	73.63	45	22.42	10	3.95
Cast Ni+Al+ 20wt% epoxy	22.15	61.33	22.15	18.67	55.7	20
Cast Ni+Al+ 30wt% epoxy	15.85	53.66	15.85	16.34	68.3	30

Static pressing of Ni+Al and Ni+Al+10vol% Teflon powder mixtures yielded rods with a 0.25" diameter and 1" length. Pressing of longer rods was not possible with the die set-up being used, due to the difficulty in removing the sample rod from the die, so pressed materials were not used for reverse anvil Taylor impact tests, which require 2" long samples. When pressing mixtures containing nano Al powder, the compact would not densify into rods and came out in flakes, thus the nano Al-containing materials were not used for any mechanical properties characterization.

The cast samples, an example of which is shown in Figure 3-4, were fabricated in the following combinations: Ni+Al+20wt% epoxy, Ni+nano Al+20wt% epoxy, Ni+nano Al+30wt% epoxy, and pure epoxy. The three types of cast samples containing metallic powders allowed for comparison between micron-sized Al and nano Al as well as between different amounts of epoxy binder. The plain epoxy sample provided a baseline for comparison with the Ni and Al-containing composites.

4.1.1 Microstructural Characteristics of Precursor Mixtures and Processed Samples

SEM analysis was used to characterize the starting precursor powders, as well as processed materials. The morphology of the as-received -325 mesh Ni and Al powders, after mixing for 24 hours in a V-blender in a 1:1 volumetric ratio, is shown in Figure 4-1a. The Al particles have a darker contrast and relatively smooth surfaces, whereas the Ni particles are brighter and have rougher surfaces. Both the Ni and the Al particles have an average size of ~10-15 μm. The range of particle sizes can be seen in Figure 4-1a, from particles only slightly over 1 μm, to those near 45 μm. Figure 4-1b shows the surface of the Ni particles at a higher magnification.

Images of the mixture of Ni (-325 mesh size) and nano Al (average of ~56.3 nm) show that the Al particles adhere to the surface of the Ni particles and form a powder dusting, as illustrated in Figure 4-1c. A higher magnification image of the spherically-shaped Al particles is shown in Figure 4-1d.

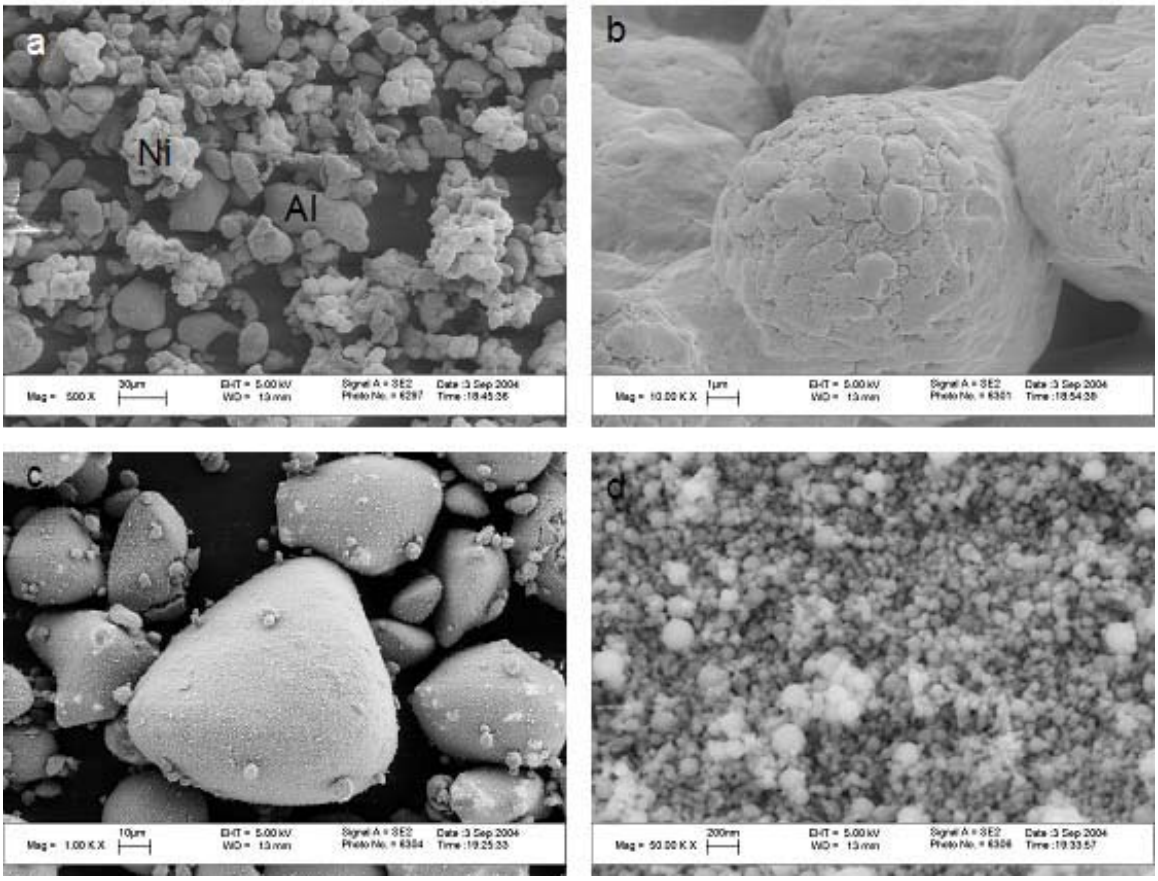

Figure 4-1: SEM images of as-mixed Ni and Al/nano Al powders. (a) Ni and Al powders (both -325 mesh) mixed 1:1 by volume in a V-blender. Ni particles are of lighter contrast and have rougher surfaces, whereas Al particles are of darker contrast and have smoother surfaces. (b) Surface of Ni powder (-325 mesh). (c) Ni and nano Al powder (-325 mesh Ni, ~56.3 nm Al) mixed 1:1 by volume. This image shows adhesion of the nano Al particles to the surface of the larger Ni particles. (d) Nano Al powder dusting the surface of a Ni particle.

The commercial Teflon powder, classified to be of 4 μm size, was found to actually be in the range of 200 nm sized particles, as evidenced in the SEM image in Figure 4-2. The powder appears to be quite spherical and very uniform in both shape and size.

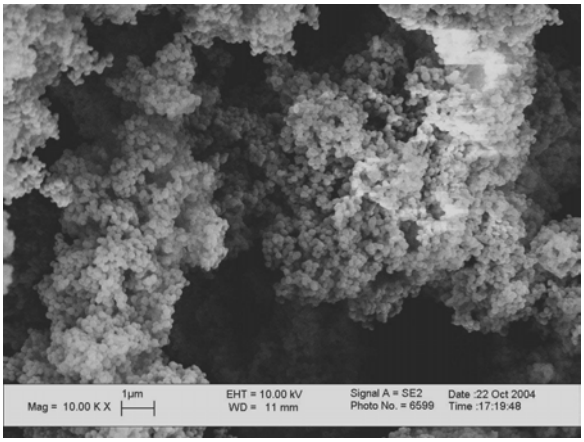

Figure 4-2: SEM image of Teflon powder showing the size and morphology of the particles.

SEM of the pressed Ni+Al powder mixture, shown in Figure 4-3a, illustrates good contact between the packed particles, with a uniform distribution of Ni and Al. The higher magnification SEM image shown in Figure 4-3b reveals deformation features in both types of particles, as well as presence of pores.

SEM images of pressed Ni+nano Al, as shown in Figure 4-3c, reveal that the nano Al particles form agglomerates and fill in the spaces around the Ni particles.

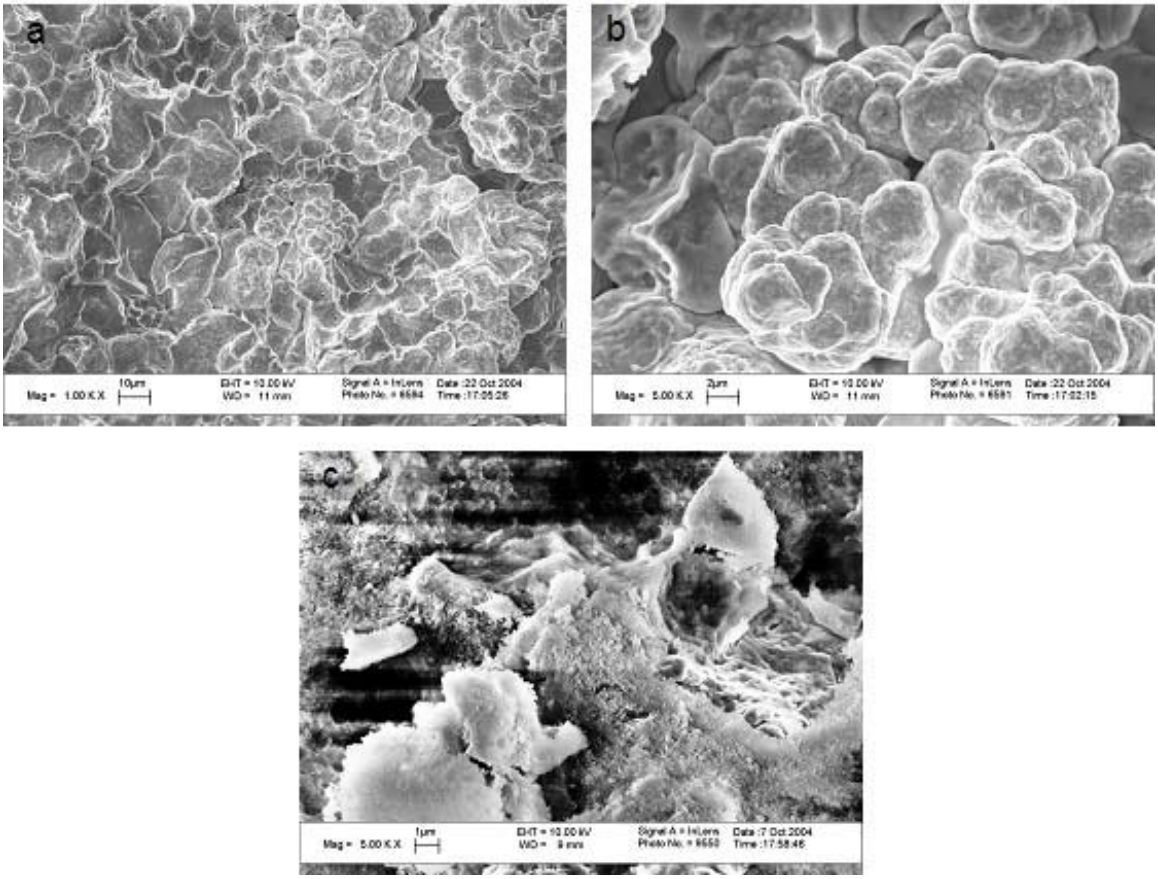

Figure 4-3: SEM images of pressed Ni+Al/nano Al powders. (a) Pressed Ni+Al fracture surface. (b) Pressed Ni+Al fracture surface showing deformation of the particles, and porosity between them. (c) Pressed Ni+nano Al fracture surface showing nano Al agglomerates.

When Teflon is added to the powder mixtures, it acts as a binder to fill in pores between the Ni and Al, as can be seen in Figure 4-4a and Figure 4-4b. The deformation of an Al particle can be seen in Figure 4-4b. In Figure 4-4c, Teflon particles show deformation from their original spherical shapes, and porosity between the Teflon particles can be seen.

Pressed samples of Ni+nano Al+10vol% Teflon show that the nano Al particles and Teflon particles tend to form agglomerates and clusters between the much larger Ni

particles, as shown in Figure 4-4d and Figure 4-4e. These agglomerates essentially create a matrix for the Ni particles, with the final pores being at the size scale of the Al and Teflon particles.

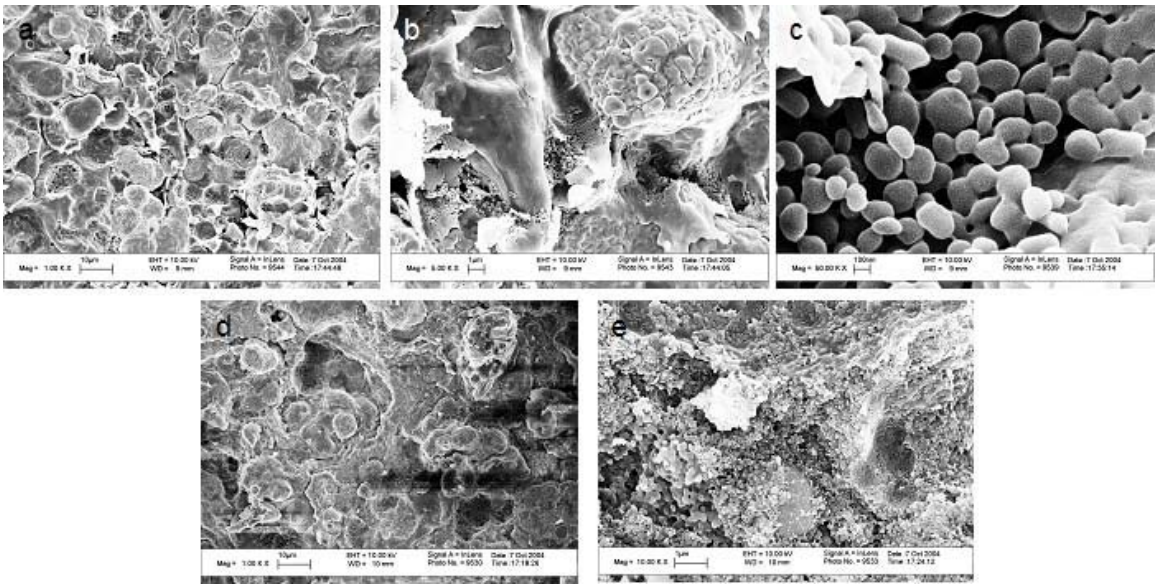

Figure 4-4: SEM images of pressed Ni+Al/nano Al+Teflon powders. (a) Pressed Ni+Al+10vol% Teflon fracture surface. (b) Pressed Ni+Al+10vol% Teflon fracture surface. (c) Teflon particles on the fracture surface of pressed Ni+Al+10vol% Teflon. (d) Pressed Ni+nano Al+10vol% Teflon fracture surface. (e) Pressed Ni+nano Al+10vol% Teflon fracture surface.

SEM analysis of the fracture surface of the cast samples reveal a much different fracture surface than the pressed samples. Samples of Ni+Al+20wt% epoxy shown in Figure 4-5a and Figure 4-5b reveal a glassy brittle fracture in the epoxy matrix. The fracture occurs around the Ni and Al particles, and no fracture of the particles themselves is seen. There is also evidence of pullout of both types of particles.

When nano Al particles were used they dispersed in the epoxy and they together formed a matrix for the Ni particles, as shown in Figure 4-5c. In this figure, the Ni

particles are of lighter contrast, and the darker contrast is the epoxy+nano Al matrix. This figure also shows locations where Ni particles have pulled out of the matrix. There does not appear to be any fracture through the Ni particles. Figure 4-5d shows a higher magnification image of two locations where Ni particles have pulled out of the matrix and formed voids. This figure also shows that the nano Al particles have formed agglomerates with the epoxy. At an even higher magnification (Figure 4-5e), the glassy fracture of the epoxy can be seen, as well as the presence of Al agglomerates. The Al particles still appear to maintain their spherical shape, and do not appear to be deformed or fractured.

Cast samples containing Ni+nano Al+30wt% epoxy have similar fracture surfaces to those containing only 20wt% epoxy, so a polished cross-section was examined instead. As shown in Figure 4-5f, this cross section shows a uniform distribution of Ni particles in the epoxy+nano Al matrix. In this case, however, there is no visible pullout of Ni particles. In Figure 4-5g, an agglomerate of Al particles can be seen in the epoxy matrix. Figure 4-5h is a higher magnification view of the nano Al particles.

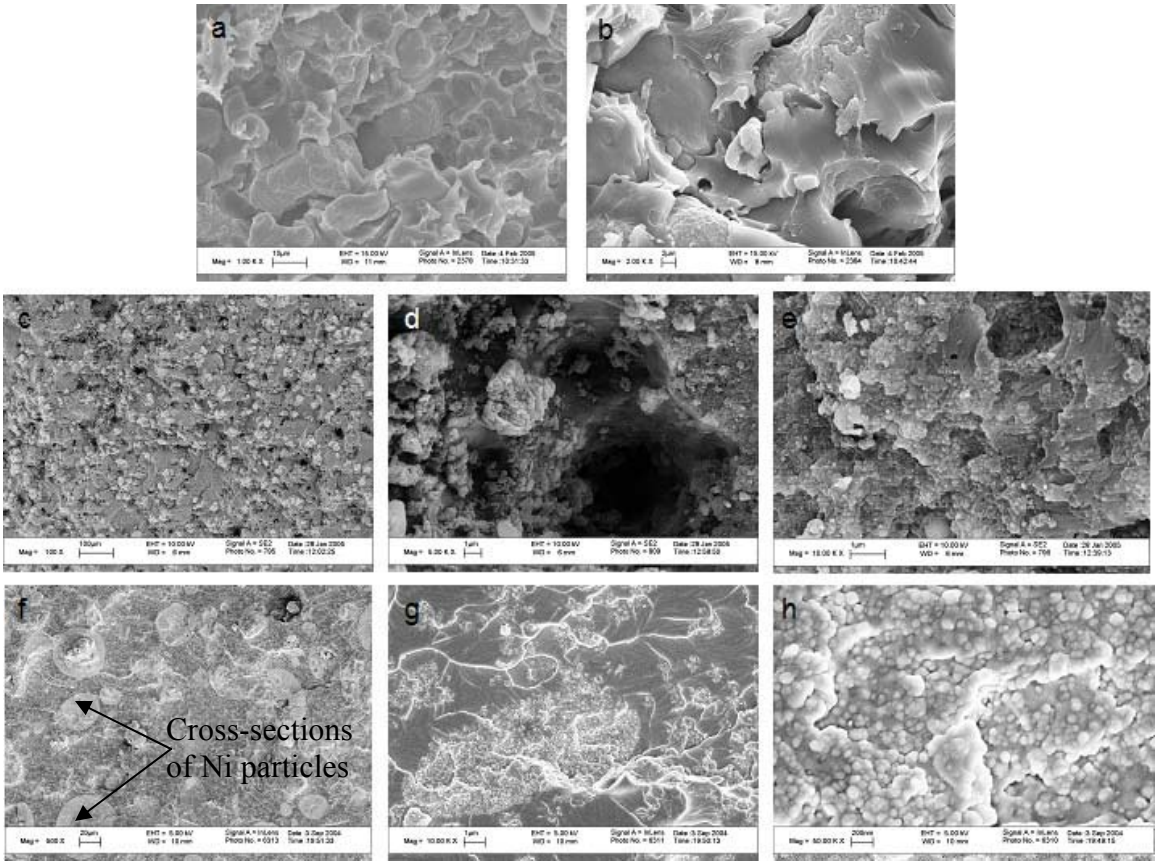

Figure 4-5: SEM images of as-cast Ni+Al/nano Al+epoxy specimens. (a) Cast Ni+Al+20wt% epoxy fracture surface. (b) Cast Ni+Al+20wt% epoxy fracture surface showing glassy fracture in the epoxy matrix. (c) Cast Ni+nano Al+20wt% epoxy fracture surface. (d) Cast Ni+nano Al+20wt% epoxy fracture surface showing voids where Ni particles have pulled out. (e) Cast Ni+nano Al+20wt% epoxy fracture surface showing nano Al agglomerates and fracture in epoxy. (f) Cast Ni+nano Al+30wt% epoxy polished surface showing Ni cross-sections in a nano Al+epoxy matrix. (g) Cast Ni+nano Al+30wt% epoxy polished surface showing Al agglomerates. (h) Cast Ni+nano Al+30wt% epoxy polished surface.

4.1.2 Density Measurements

Density measurements were made following the procedure outlined in Section 3.2.1.4. The experimentally determined values were compared to theoretical values calculated using literature values of components, which are listed in Table 4-2, and the Voigt Rule of Mixtures. From this comparison, the percentage of theoretical maximum

density was calculated and porosity of the pressed and cast samples was determined. The theoretical density values, measured density values, % TMD and % porosity are listed in Table 4-3 and also shown as a bar graph in Figure 4-6.

Table 4-2: Densities of starting materials.

Material	**Density (g/cm^3)**
Ni	8.874
Al	2.785
Ni-Al (1:1 by volume)	5.830
Teflon	2.16
Epoxy	1.19

Table 4-3: Measured and Theoretical Density Values, %Theoretical Maximum Density, and % Porosity for all fabricated samples.

Material	Theoretical Density (g/cm^3)	Measured Density (g/cm^3)	% TMD	% Porosity
Ni+Al	5.83	5.46 ± 0.06	93.7	6.3
Ni+nano Al	5.83	5.01 ± 0.32	85.9	14.1
Ni+Al+10vol% Teflon	5.46	4.99 ± 0.06	91.3	8.7
Ni+nano Al+10vol% Teflon	5.46	4.38 ± 0.11	80.2	19.8
Ni+Al+20wt% epoxy	3.25	3.50 ± 0.13	100	0
Ni+nano Al+20wt% epoxy	3.25	3.26 ± 0.01	100	0
Ni+nano Al+30wt% epoxy	2.84	2.67 ± 0.07	94.0	6.0

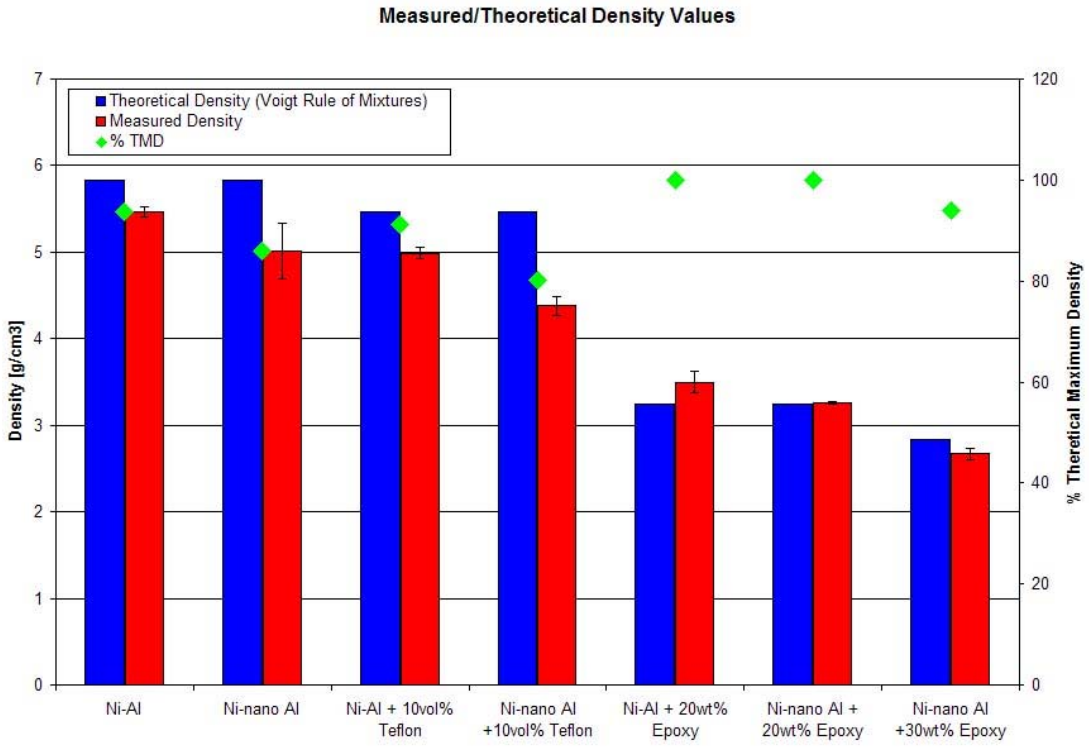

Figure 4-6: Theoretical vs. measured density values for all fabricated materials, as well as %TMD, which is related to porosity.

A comparison of the density of materials containing -325 mesh Al particles with that of materials containing nano Al shows that the nano Al-containing materials are less dense (Ni+Al was 6.3% porous, whereas Ni+nano Al was 14.15% porous). This can be attributed to a less efficient packing of the particles since there are many nano-sized pores created between the Al particles in addition to the larger pores between the Ni particles. The addition of Teflon lowers the theoretical density of the bulk material; this is expected due to the low density of Teflon. What is unexpected, however, is that the addition of a binder would lower the percentage of TMD, or increase the percentage of porosity in the powder pressed samples (Ni+Al was 6.3% porous, whereas Ni+Al+Teflon was 8.7% porous) when pressed at the same static pressure. It seems that although Teflon does act as a binder in holding the powders together more securely, it does not fill all of the voids in the material, but instead small pores are created between the Teflon particles. While the Teflon-containing samples ranged from 8.7 to 19.8% porosity, the cast samples ranged from only 0 to 6% porosity. The samples with an epoxy binder were essentially 100% dense, except for the sample containing 30% epoxy, which was ~6% porous. The ~6% porosity in the higher epoxy content material can be attributed to air bubbles formed during the casting process, even though the samples were degassed. Although the epoxy-filled samples achieved a higher percentage of their TMD, their overall densities are much lower than the plain Ni+Al or Teflon-filled materials due to the large percentage of epoxy and its low density.

4.2 Characterization of Reaction Energetics

Differential Thermal Analysis (DTA) was used to characterize the energetics of thermally initiated reactions in Ni-Al-polymer multifunctional energetic structural

materials. In addition to determining the temperatures of endothermic and exothermic events recorded by the DTA, the samples were also examined by x-ray diffraction (XRD) analysis at temperatures corresponding to the endothermic and exothermic events to determine thermally initiated reaction products of Ni and Al, and Ni+Al with the polymer binders.

4.2.1 Differential Thermal Analysis

DTA was performed on precursor mixture materials and fabricated materials in every combination of particle size and binder content that was used in this study. This allowed for a complete analysis of thermally initiated reaction behavior of powders, pressed powders, and cast materials.

4.2.1.1 DTA of Starting Reactants

Figure 4-7 shows results of DTA performed on the individual starting powders (Ni, Al, nano Al, Teflon) to identify endothermic/exothermic events occurring due to melting or decomposition, or reactions with any absorbed gas. The Heat Flow vs. Temperature graphs showed no peaks in the case of Ni powder (Figure 4-7, Trace 'a'), as expected upon heating to 800 °C. However, Al powder (Figure 4-7, Trace 'b') showed a large endotherm at its melting temperature (~660 °C). Nano Al (Figure 4-7, Trace 'c') also showed an endotherm at its melting point, however with a slightly lower onset temperature. Teflon (Figure 4-7, Trace 'd') showed two endotherms, one at ~315 °C and one at 530 °C, corresponding to its decomposition.

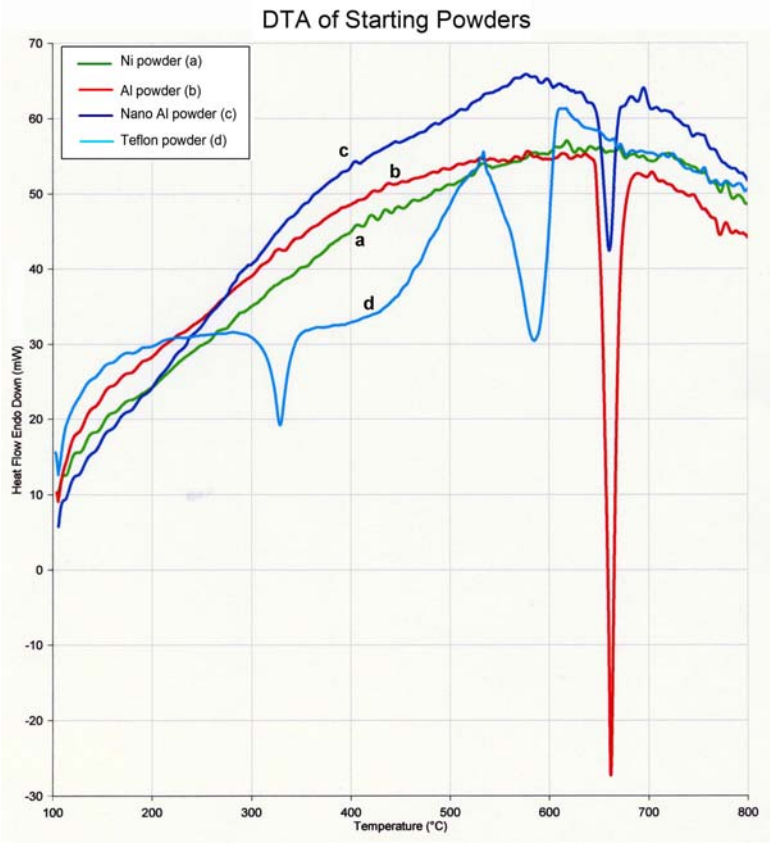

Figure 4-7: Heat Flow vs. Sample Temperature graph of starting powders obtained by DTA. An endotherm can be seen at the melting temperature of Al, for both sizes of Al powders. Ni does not show any evidence of phase changes in the temperature range investigated. Teflon powder shows two endotherms corresponding to its decomposition.

4.2.1.2 DTA of As-Mixed Powder Precursors

DTA was also performed on several combinations of mixed powders; the resulting traces are shown in Figure 4-8. The mixture of Ni and Al powders (Figure 4-8, Trace 'a') revealed a large reaction exotherm, at a temperature slightly lower than the melting temperature of Al ($T_{m,Al}$) that was seen in Trace 'a' of Figure 4-7, indicating that the reaction between Ni and Al initiates at the eutectic temperature. In contrast, the Ni+nano Al mixture (Figure 4-8, Trace 'b') showed a small endotherm corresponding to the melting of Al, immediately followed by a small exotherm corresponding to reaction.

The onset temperature of these two peaks was at a slightly higher temperature than that observed in the case of the micron-sized particles.

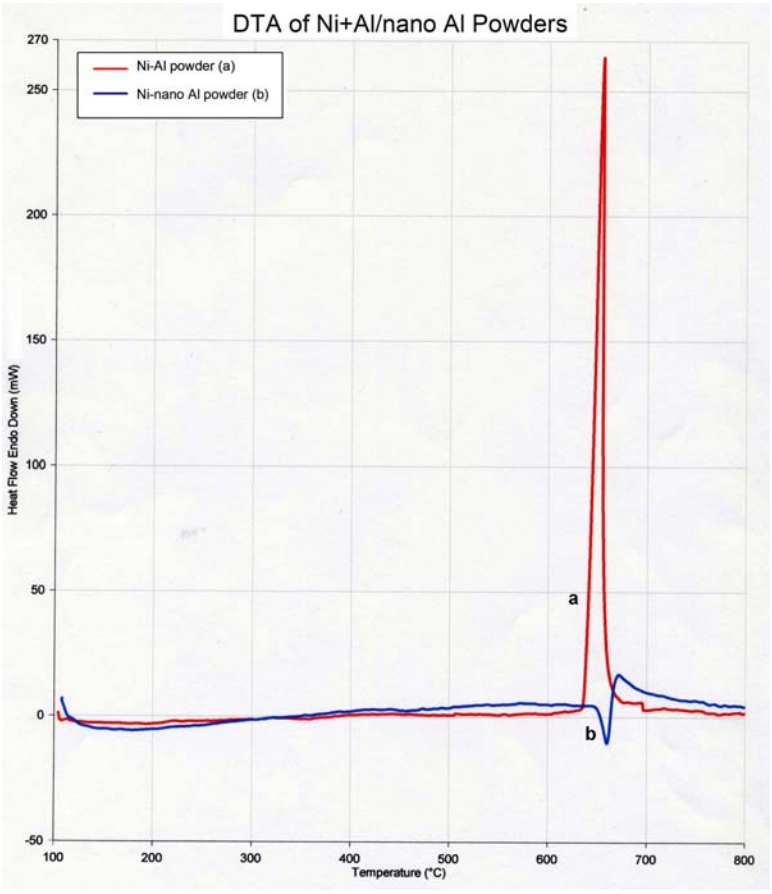

Figure 4-8: Heat Flow vs. Sample Temperature graph of Ni + Al/nano Al powders obtained by DTA. Ni+Al show a reaction exotherm at $T_{m,Al}$. Ni+nano Al shows an endotherm followed by a reaction exotherm at $T_{m,Al}$.

DTA results of the Teflon-containing loose powder mixtures are shown in Figure 4-9. The Ni+Al+Teflon mixture (Figure 4-9, Trace 'a') showed an exotherm at a temperature slightly less than that of the second decomposition exotherm of Teflon (~530 °C, as shown in Figure 4-7, Trace 'd'), and was immediately followed by a second

exotherm at the melting temperature of Al. These exotherms indicate possible reactions of Ni with Al, and of Ni+Al with Teflon. The Ni+nano Al+Teflon mixture (Figure 4-9, Trace 'b'), showed an exotherm at a temperature corresponding to Teflon's second decomposition, just as in the case with micron-sized powders, and an additional exotherm above the temperature of Teflon's first decomposition peak, indicating two reactions of Ni+Al with Teflon. The Ni+nano Al mixture also showed an endotherm at $T_{m,Al}$, indicating the melting of Al, but no evidence of reaction between Ni and nano Al.

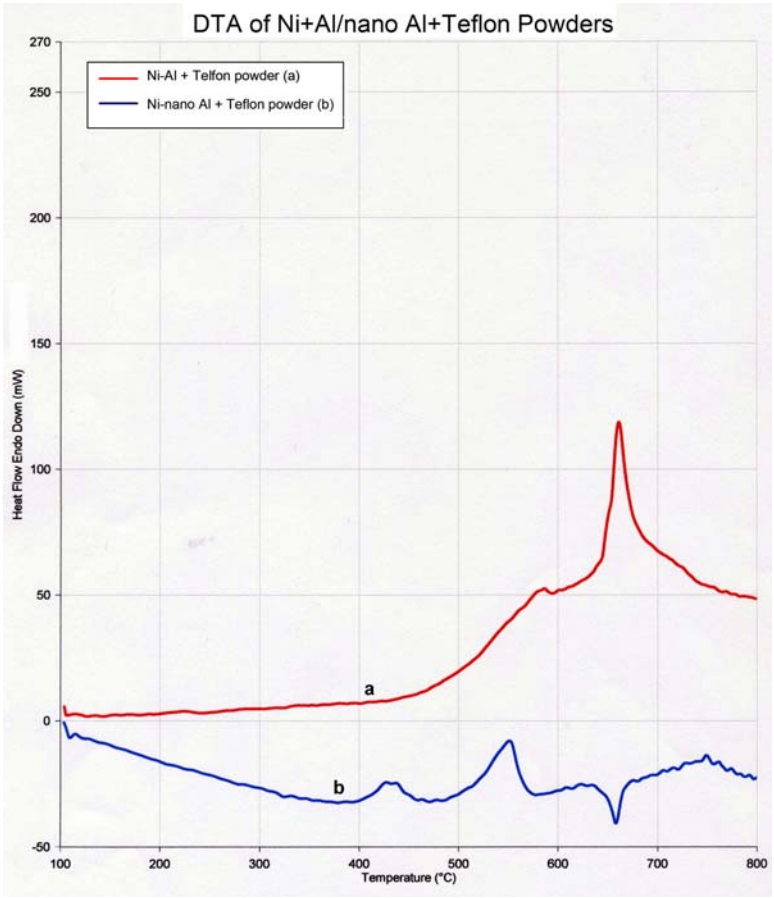

Figure 4-9: Heat Flow vs. Sample Temperature graph of Ni + Al/nano Al + Teflon powders obtained by DTA. Ni+Al+Teflon shows one reaction exotherm at a temperature corresponding to Teflon's second decomposition, and another exotherm at $T_{m,Al}$. Ni+nano Al+Teflon shows reaction exotherms at both temperatures where Teflon showed decomposition. This mixture showed only an endotherm at $T_{m,Al}$.

DTA was also performed on mixtures of Al+Teflon and nano Al+Teflon, as shown in Figure 4-10, to determine if the exotherms observed in the Ni-Al-Teflon mixtures at temperatures in the ranges of the decomposition peaks of Teflon were reactions between Al+Teflon, Ni+Teflon, or Ni+Al+Teflon. DTA traces of Al with Teflon (Figure 4-10, Trace 'a') revealed an exothermic reaction between Al and Teflon at a temperature corresponding to the second decomposition of Teflon (Figure 4-7, Trace'd'), similar to what was seen in the case where Ni was also present (Figure 4-8, Trace 'a'). At $T_{m,Al}$, the Al+Teflon mixture showed only an endotherm, implying that in the Ni+Al+Teflon mixture (Figure 4-9, Trace 'a') the reaction was between Ni and Al only. In the case of nano Al+Teflon (Figure 4-10, Trace 'b'), exotherms were seen at both temperatures where Teflon decomposed, and an endotherm at $T_{m,Al}$. Since the Al+Teflon mixtures showed the same exotherms as the Ni+Al+Teflon mixtures, the reactions were believed to be between Al and Teflon.

DTA results on the powder mixtures illustrate that in the absence of Teflon, Ni reacts strongly with micron-sized Al at the melting temperature of Al, but it reacts to a lesser degree with nano Al. Micron-sized Al reacts with Teflon following its second decomposition at ~530 °C, whereas nano-Al reacts with Teflon at both temperatures where Teflon decomposes.

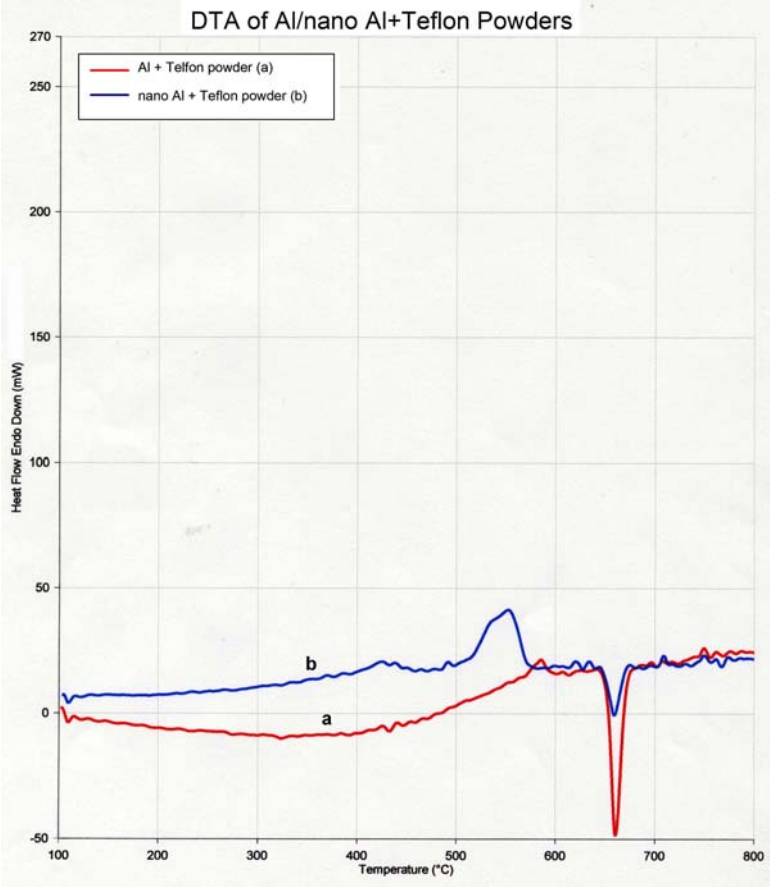

Figure 4-10: Heat Flow vs. Sample Temperature graph of Al/nano Al + Teflon powders obtained by DTA. Al+Teflon shows an exotherm near Teflon's second decomposition temperature and an exotherm at $T_{m,Al}$. Nano Al+Teflon shows exotherms near both Teflon decomposition temperatures, and an endotherm at $T_{m,Al}$.

4.2.1.3 DTA of Pressed Powders

As shown in Figure 4-11, DTA was also performed on powder mixtures after they were pressed into cylindrical rods. This was done to determine the effect of a more compact density on the reaction behavior of these materials. Pressed Ni+Al (Figure 4-11, Trace 'a') showed the same large exotherm as in the case of the unpressed powders, but it also showed a small "pre-initiation" exotherm around 560 °C as seen in studies by Hammetter *et al.* [20]. This pre-initiation exotherm is believed to be caused by reaction

occurring due to solid state diffusion, prior to the more catastrophic reaction occurring upon melting of Al. Pressed Ni+nano Al (Figure 4-11, Trace 'b') did not show the same large exotherm as in the case with micron-scale Al. Instead, this combination showed a pre-initiation exotherm that merged into a small reaction exotherm at the melting temperature of Al.

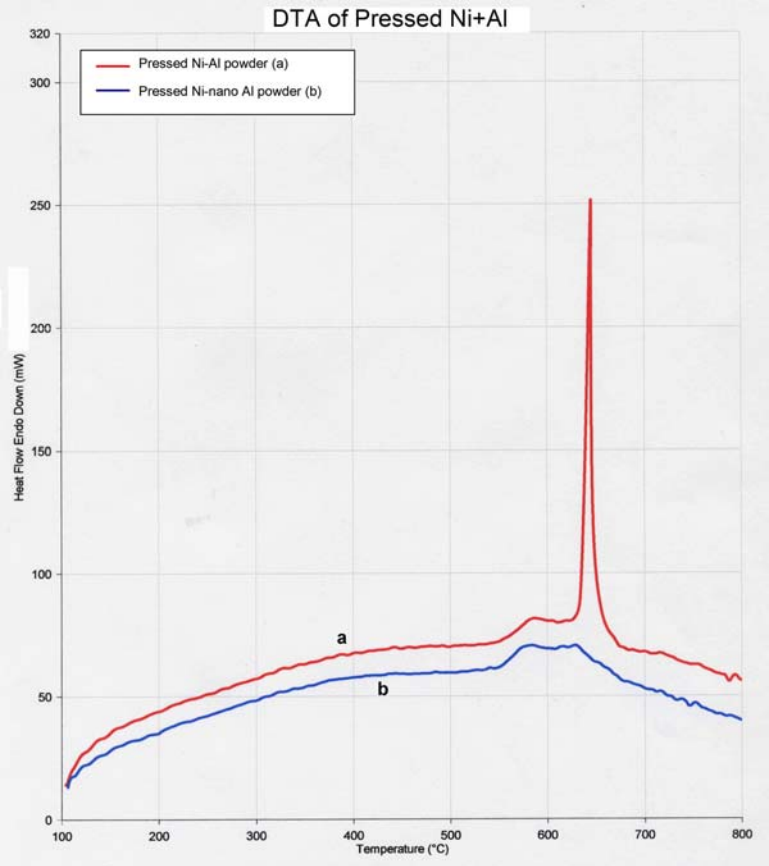

Figure 4-11: Heat Flow vs. Sample Temperature graph of pressed Ni + Al/nano Al powders obtained by DTA. Both samples show an additional "pre-initiaiton" exotherm prior to the main reaction exotherm that is due to enhanced solid state diffusion. The sample containing micron-scale Al shows a much more pronounced reaction exotherm when compared with the nano Al-containing material.

When Teflon was added to the pressed Ni+Al powder mixture (Figure 4-12, Trace 'a'), the DTA traces were similar to those seen in the unpressed Ni+Al+Teflon powder (Figure 4-9, Trace 'a'). The Ni+Al+Teflon pressed sample (Figure 4-12, Trace 'a') showed a small exotherm in the range of a pre-initiation peak, in addition to a large exotherm indicating reaction between Ni+Al. The pressed Ni+nano Al+Teflon material (Figure 4-12, Trace 'b') showed exotherms at both temperatures where Teflon decomposes (as determined by DTA of Teflon alone), indicating two reactions between nano Al and Teflon, as also seen in the unpressed powders.

Hence, the DTA results on pressed powders are very similar to those seen in the same mixtures of unpressed powders. Again, it can be noted that the nano Al reacts with Ni only when there are no other materials present, while micron-sized Al reacts with Ni regardless of the presence of a Teflon binder. The major difference between the pressed and unpressed powders is evidence of the pre-initiation peak (around 550 °C), believed to be due to a solid state diffusion reaction, which is expected to be favored by powder densification.

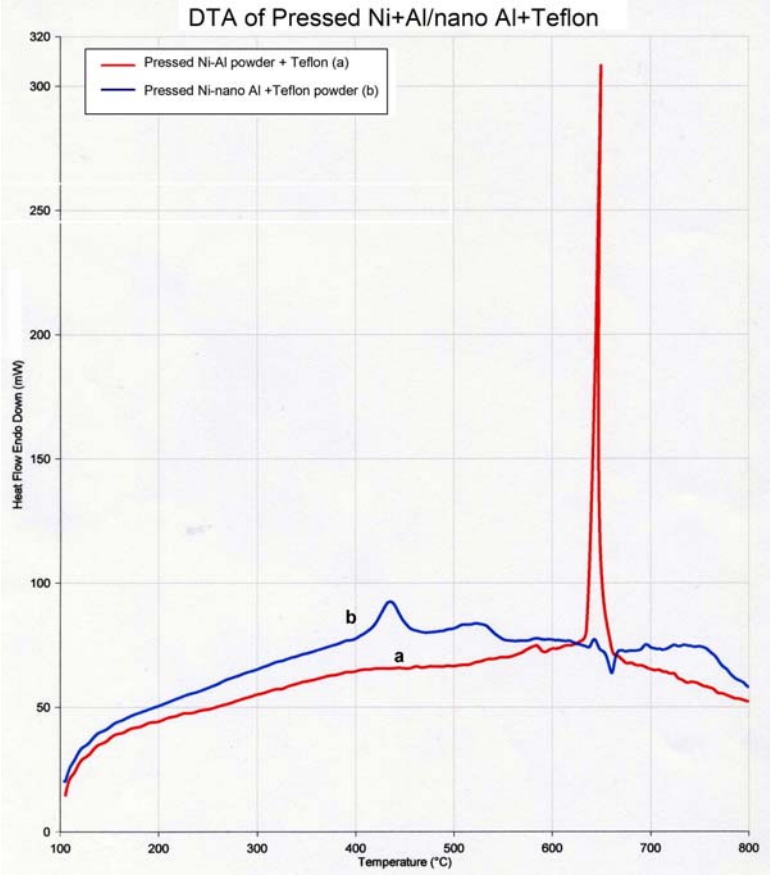

Figure 4-12: Heat Flow vs. Sample Temperature graph of pressed Ni+Al/nano Al+Teflon powders obtained by DTA. Pressed Ni+Al+Teflon showed a pre-initiation exotherm and a main reaction exotherm. Pressed Ni+nano Al+Teflon shows two exotherms at the temperatures where Teflon decomposes, as well as a small exotherm and endotherm at $T_{m,Al}$.

4.2.1.4 DTA of Epoxy-Cast Materials

Reactivity of cast materials consisting of Ni+Al/nano Al+epoxy was also analyzed using DTA, as shown in Figure 4-13a. DTA of epoxy alone (Figure 4-13a, Trace 'a') showed a reaction exotherm near 340 °C, which corresponded to crystallization. DTA of the Ni+Al+20wt% epoxy (Figure 4-13a, Trace 'b') showed a slight exotherm at a temperature corresponding to that seen in the epoxy (~340 °C), as well as a large exotherm corresponding to reaction between Ni and Al. There were no pre-initiation

peaks in these materials in contrast to those observed in the pressed materials. DTA of the Ni+nano Al+20wt% epoxy (Figure 4-13a, Trace 'c') also showed the slight epoxy exotherm. However, there was no evidence of reaction between Ni and nano Al, only an endotherm corresponding to melting of Al. Similarly, Ni+nano Al+30wt% epoxy (Figure 4-13a, Trace 'd') showed similar endothermic and exothermic events with no reaction between Ni and nano Al.

The epoxy-cast materials showed no reaction between Ni+nano Al, but did show reaction between Ni+micron-sized Al. The presence of a polymer binder appears to affect the reaction between Ni and nano Al in both the pressed and epoxy-cast samples. It is unclear if Ni+Al/nano Al participate in the reaction with epoxy near ~340 °C.

Cast materials recovered from reverse Taylor anvil impact tests were also analyzed using DTA to determine if dynamic deformation of the samples had any effect on their reaction behavior. The DTA traces, as shown in Figure 4-13b, did not show any exothermic or endothermic events that were different from those observed in the as-cast samples. It can be concluded that the deformation conditions achieved during the Taylor impact tests did not alter the reaction characteristics of these cast materials.

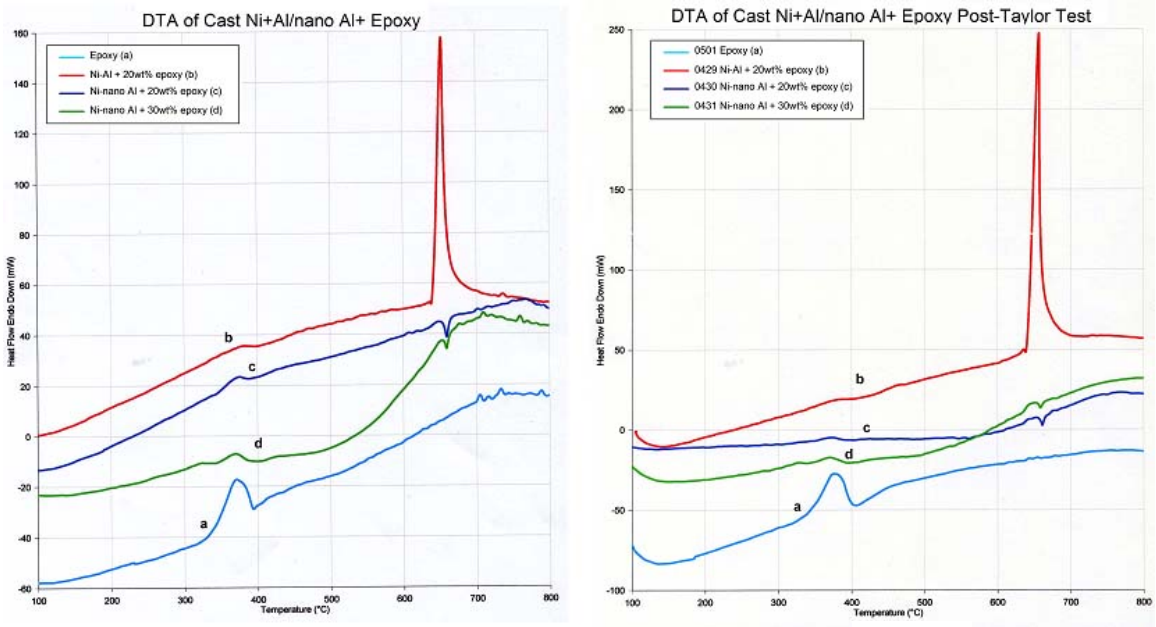

(a) (b)

Figure 4-13: Heat Flow vs. Sample Temperature graph of cast materials obtained by DTA: (a) as-cast specimens and (b) post-impact cast specimens. Epoxy shows an exotherm at ~340 °C; this same exotherm is seen in the Ni and Al-containing cast samples as well. The nano Al-containing cast materials do not show a main reaction exotherm, indicating that there is no reaction between Ni and nano Al in these samples. The qualitative aspects of these traces are similar, indicating that the impact had no effect on the reactivity of the materials.

4.2.2 X-Ray Diffraction Characterization of Reaction Products

X-ray diffraction analysis was performed on all materials in the as-fabricated state and after heating to various temperatures. The temperatures to which the materials were heated before performing x-ray diffraction were determined from the reaction exotherms in DTA traces. For each reaction, the sample was heated in the DTA to a temperature at which the reaction was complete, and the sample was subsequently characterized by XRD analysis to determine the products from each reaction. XRD traces are shown in Appendix A.1 and are organized according to the corresponding reaction exotherm, and therefore the heating temperature. There were reactions observed near the melting

temperature of Al, the "pre-initiation" peak prior to the melting of Al, the crystallization of epoxy, and the two decomposition reactions of Teflon. Table 4-5, Table 4-6 and Table 4-7 summarize the approximate onset temperatures and heat flow directions of each peak observed in DTA, as well as the temperatures that the materials were heated to in order to insure complete reaction before XRD analysis. Also, the tables include a summary of the reaction products formed from Ni-Al mixtures, Teflon-containing materials, and epoxy-cast materials during each exotherm.

4.2.2.1 XRD of Ni+Al/nano Al Materials

The mixtures of Ni+Al/nano Al starting powders used in fabrication of the MESMs revealed the XRD peaks shown in the Appendix in Figure A-1 and listed in Table 4-4. As shown in Figure A-2, the Ni and Al peaks are consistent even after heating to 800 °C, which encompasses the full temperature range used for this analysis. The presence of Al_2O_3 in the nano Al powder upon heating should be noted. This is due to the oxide coating on the nanoparticles.

Table 4-4: Locations of XRD peaks for Ni and Al.

	hkl	2Theta
Nickel	111	45
	200	52
	220	77
	311	93
	222	98
Aluminum	111	39
	200	45
	220	65
	311	78
	222	82

Table 4-5, which summarizes the reactions taking place in Ni and Al mixtures, corresponds to the XRD traces in Appendix A.1.1. Samples that showed a "pre-initiation" exotherm were heated to 620 °C and x-ray diffraction was performed (Figure A-3). Pressed Ni+Al showed evidence of formation of Ni_2Al_3 and Ni_5Al_3 after being heated to 620 °C. Pressed Ni+nano Al formed only Ni_2Al_3 after being heated to 620 °C, but also showed Al_2O_3 peaks since the nano Al has an oxide coating. Both of these materials also showed Ni and Al peaks indicating that the individual constituents were not fully reacted at this stage.

In Ni+Al/nano Al mixtures, the only other reaction exotherm seen was at the melting temperature of Al. To investigate the reaction products formed at this stage, the samples were heated to 800 °C and XRD analysis was performed (Figure A-4). Ni+Al powder heated to 800 °C reacted to form NiAl, the main reaction product expected from a 1:1 volumetric mixture (76.66wt% Ni, 23.34wt% Al) of Ni and Al according to the Ni-Al phase diagram shown in Figure 2-1. Ni_3Al was also formed from Ni+Al powder after heating to 800 °C. There were Ni peaks present, but no Al peaks, indicating that Al had fully reacted. When this same material combination was pressed and heated to 800 °C, the reaction products were the same as formed by the unpressed powder, with the addition of Ni_2Al_3. Since Ni_5Al_3 had been a product of Ni+Al powder at 620 °C, but not at 800 °C, this indicates that it formed during the pre-initiation and then reacted again when Al melted.

Ni_3Al was formed when the Ni+nano Al powder mixtures was heated, similar to the case of its micron-sized counterpart; Ni_5Al_3 was also formed, but no NiAl. When pressed, the Ni+nano Al formed NiAl, $NiAl_3$ and Ni_2Al_3 after heating to 800 °C, which

are the same products formed with the micron-sized Al and the same treatment. Both the pressed and loose powder samples containing nano-sized Al particles showed both Ni and Al peaks after heating to 800 °C, indicating that the Al had not fully reacted as it had in the micron-sized counterparts.

Table 4-5: Reaction products formed at various stages in Ni-Al mixtures.

Event / Sample	Pre-initiation (DTA to 620 °C)	Melting of Al (DTA to 800 °C)
Ni+Al Powder	N/A	T_{exo}: 640 °C Products: Ni, NiAl, Ni_3Al
Ni+nano Al Powder	N/A	T_{endo}: 650 °C T_{exo}: 670 °C Products: Ni, Al, Ni_3Al, Ni_5Al_3
Pressed Ni+Al	T_{exo}: 560 °C Products: Ni, Al Ni_2Al_3, Ni_5Al_3	T_{exo}: 630 °C Products: Ni, NiAl, Ni_3Al, Ni_2Al_3
Pressed Ni+nano Al	T_{exo}: 560 °C Products: Ni, Al, Ni_2Al_3, Al_2O_3	T_{exo}: 610 °C Products: Ni, Al, NiAl, Ni_3Al, Ni_2Al_3

4.2.2.2 XRD of Epoxy-Cast Materials

XRD traces of the cast materials are shown in Appendix A.1.2. The corresponding summary of events and reaction products is presented in Table 4-6. XRD traces of the as-cast materials are presented in Figure A-5. Epoxy alone does not show any distinct peaks at room temperature since it is amorphous at T<340 °C, but the Ni and Al peaks are consistent with those seen in the materials without epoxy.

In DTA traces, epoxy showed a reaction exotherm near 340 °C corresponding to crystallization. This exotherm was observed in all cast materials, so XRD analysis was

performed after heating to 400 °C to allow for completion of this reaction. Analysis of the XRD traces (Figure A-6) corresponding to this epoxy crystallization exotherm did not reveal any peaks indicative of reaction between Ni and/or Al/nano Al and epoxy. Since the DTA trace of epoxy alone showed a reaction exotherm, there is no clear evidence that the exotherms observed when Ni and Al were also present were related to anything other than the epoxy. Another indication that the reaction exotherm observed near 340 °C may be due entirely to epoxy is that the exotherm was observed at the same temperature for each sample, whereas if Ni and Al participated in the reaction, they would be likely to alter the onset temperature of the reaction.

After heating to 800 °C, XRD analysis of the cast samples (Figure A-7) revealed Ni+Al products only in the case of the Ni+Al+20% epoxy sample. The Ni+Al+20% epoxy sample reacted to from Ni_3Al and Ni_2Al_3 after heating to 800°C. Neither of the samples containing nano Al showed any reaction between Ni and nano Al, which is consistent with the DTA results of the mixtures, which suggested that nano Al prefers to react with the polymer binder than Ni. However, there were not any peaks indicative of reaction between nano Al and epoxy either. Additionally, these nano Al-containing samples showed Al peaks indicating incomplete reaction, whereas the micro-powder sample did not show any remaining Al peaks.

Table 4-6: Reaction products formed at various stages in epoxy-cast Ni+Al/nano Al mixtures.

Sample \ Event	Epoxy Decomposition (DTA to 400 °C)	Melting of Al (DTA to 800 °C)
Epoxy	T_{exo}: 340 °C Products: epoxy constituents	N/A
Ni+Al+20wt% epoxy	T_{exo}: 340 °C Products: Ni, Al, epoxy constituents	T_{exo}: 650 °C Products: Ni, epoxy constituents, Ni_3Al, Ni_2Al_3
Ni+nano Al+20wt% epoxy	T_{exo}: 340 °C Products: Ni, Al, epoxy constituents	T_{endo}: 650 °C Products: Ni, Al, epoxy constituents
Ni+nano Al+30wt% epoxy	T_{exo}: 340 °C Products: Ni, Al, epoxy constituents	T_{endo}: 650 °C Products: Ni, Al, epoxy constituents

4.2.2.3 XRD of Teflon-Containing Materials

The third grouping of materials studied using XRD analysis was the Teflon-containing materials. The results from this analysis are summarized in Table 4-7 and correspond to the XRD traces in Appendix A.1.3. XRD was performed on Teflon starting powder, as well as Ni+Al/nano Al mixtures containing Teflon (Figure A-8). Teflon starting powder exhibited one peak around 18 °2Θ, and the starting mixtures showed Ni and Al peaks consistent with those presented in Table 4-4, indicating that the mixtures have no effect on the placement of the peaks. After heating to 800 °C, Teflon showed many peaks (Figure A-9) corresponding to C and F compounds, which could not be identified precisely. These compounds were formed during the two endothermic events (corresponding to decomposition) seen when DTA was done on Teflon alone.

XRD of samples heated to the temperature where Teflon first decomposed (400-500 °C depending on the exact position of the peak for each sample) revealed the separate, unreacted Ni (when present) and Al peaks, as well as many peaks corresponding to C and F compounds (Figure A-10). There were no remaining peaks indicative of reaction between Ni and/or Al with Teflon. Peaks corresponding to AlF_3 overlap with the peaks of the C and F compounds, so AlF_3 is a possible product at this stage, but its presence cannot be definitely determined from these traces. It is expected, however, that there is a reaction between Al and Teflon due to the exothermic peaks observed during DTA when only these two materials were present.

XRD of materials showing reaction at Teflon's second decomposition peak (Figure A-11) revealed peaks very similar to those seen when reactions at temperatures corresponding to Teflon's first decomposition peak were analyzed. Again, there are no peaks indicative of reaction between Al and Teflon, but AlF_3 is a possible product.

The only Teflon-containing material that showed a "pre-initiation" exotherm was the pressed Ni+Al+Teflon material. This was heated to 620 °C and XRD analysis was performed (Figure A-12). There was no evidence of reaction of any kind in this sample, contradictory to the pressed Ni+Al material without Teflon.

Aluminum melts near 660 °C, and at this temperature reactions take place between Ni and Al, and possibly also with Teflon. To investigate this, samples were heated to 800 °C to insure that the reaction had taken place, and then XRD analysis was performed (Figure A-13). The Al+Teflon powder mixture showed only Al peaks and C and F compound peaks. As with lower temperatures, there was no evidence besides the DTA trace that Al and Teflon had reacted, but again AlF_3 is possible. The Ni+Al+Teflon

powder mixture showed the same products as formed with only Ni and Al powders: Ni, NiAl and Ni_3Al. However, pressed Ni+Al+Teflon showed NiAl, Ni_3Al, and Ni_2Al_3, in addition to some evidence of NiC_x and NiF_3. These Ni-based products are unexpected since the DTA traces showed reaction occurred between Al and Teflon.

In the case of the materials containing nano Al powder, some slightly different products were formed after heating to 800°C (Figure A-13). XRD of nano Al+Teflon showed no distinct evidence of reaction, similar to all other Al+Teflon mixtures. When Ni was added to the mixture, the products were Ni, Ni_3Al and Ni_5Al_3 (just as in the case when Teflon was not present), in addition to evidence of NiC_x. There were no Al peaks present in this case, which suggests that the presence of Teflon may cause the nano Al to react fully, which is another indication that Teflon may be reacting with Al. When pressed, Ni+nano Al+Teflon reacted to form NiAl, $NiAl_3$ and Ni_2Al_3, and there was no distinct evidence of reaction with Teflon.

Table 4-7: Reaction products formed at various stages in Teflon-containing Ni-Al mixtures.

Event / Sample	Teflon Decomposition 1 (DTA to 400-500 °C)	Teflon Decomposition 2 (DTA to 600-650 °C)	Pre-initiation (DTA to 620 °C)	Melting of Al (DTA to 800 °C)
Teflon	T_{endo}: 315 °C Products: C & F compounds	T_{endo}: 530 °C Products: C & F compounds	N/A	N/A
Al+Teflon Powder	N/A	T_{exo}: 570 °C Products: Al, C & F compounds, possible AlF_3	N/A	T_{endo}: 640 °C Products: Al, C & F compounds, possible AlF_3
Nano Al+Teflon Powder	T_{exo}: 400 °C Products: Al, C & F compounds, possible AlF_3	T_{exo}: 510 °C Products: Al, C & F compounds, possible AlF_3	N/A	T_{exo}: 640 °C Products: Al, C & F compounds, possible AlF_3
Ni+Al+ Teflon Powder	N/A	T_{exo}: 510 °C Products: Ni, Al, C & F compounds, possible AlF_3	N/A	T_{exo}: 640 °C Products: Ni, NiAl, Ni_3Al
Ni+nano Al+Teflon Powder	T_{exo}: 400 °C Products: Ni, Al, C & F compounds, possible AlF_3	T_{exo}: 500 °C Products: Al, C & F compounds, possible AlF_3	N/A	T_{exo}: 640 °C Products: Ni, Ni_3Al, Ni_5Al_3, NiC_x
Pressed Ni+Al+ Teflon	N/A	N/A	T_{exo}: 570 °C Products: Ni, Al, C & F compounds	T_{exo}: 640 °C Products: Ni, NiAl, Ni_2Al_3, Ni_3Al, Ni_5Al_3, NiC_x, NiF_3
Pressed Ni+nano Al+Teflon	T_{exo}: 400 °C Products: Al, C & F compounds, possible AlF_3	T_{exo}: 500 °C Products: Al, C & F compounds, possible AlF_3	N/A	T_{exo}: 640 °C T_{endo}: 650 °C Products: Ni, NiAl, Ni_2Al_3, Ni_3Al

Although some aspects of the reaction behavior in these Ni-Al-polymer systems still remains unclear, some trends appear to clearly emerge. Nano Al shows Al_2O_3 peaks when it is heated to 800 °C. NiAl is the main reaction product formed during the reaction at 660 °C, except in epoxy-cast materials and unpressed powders containing nano Al. Ni_5Al_3 is a final reaction product in unpressed powders containing nano Al, and is an intermediate product in pressed Ni+Al. Ni_2Al_3 is a product formed only when powders are pressed (and in cast Ni+Al+20% epoxy). Ni and Al react when in an epoxy matrix, but Ni and nano Al do not. It is unclear from XRD if Al reacts with Teflon, but there is evidence of reaction between Ni and Teflon. Likewise there is no evidence that reaction products of Ni+Al/nano Al further react with epoxy of Teflon in the temperature range investigated.

4.3 Mechanical Properties Characterization

Mechanical properties of epoxy-cast multifunctional energetic structural materials were evaluated both statically and dynamically. Static compression tests were used to generate stress-strain curves and to determine the elastic modulus and yield strength for each material. The experimentally determined properties of the materials were compared to theoretical values calculated using the Rule of Mixtures and values of the constituents, which were obtained from literature (Table 3-2). Finally, dynamic mechanical properties were determined using reverse anvil Taylor impact tests. It should be noted that due to difficulties in obtaining pressed samples with Teflon binder, dynamic mechanical properties were not evaluated for those materials.

4.3.1 Static Mechanical Compression Testing

Compression tests were performed on all cast materials as well as on Ni+Al+Teflon. The engineering stress vs. strain curves produced, illustrated in Figure 4-14, show that both the yield strength and elastic modulus varied according to the exact make-up of the material.

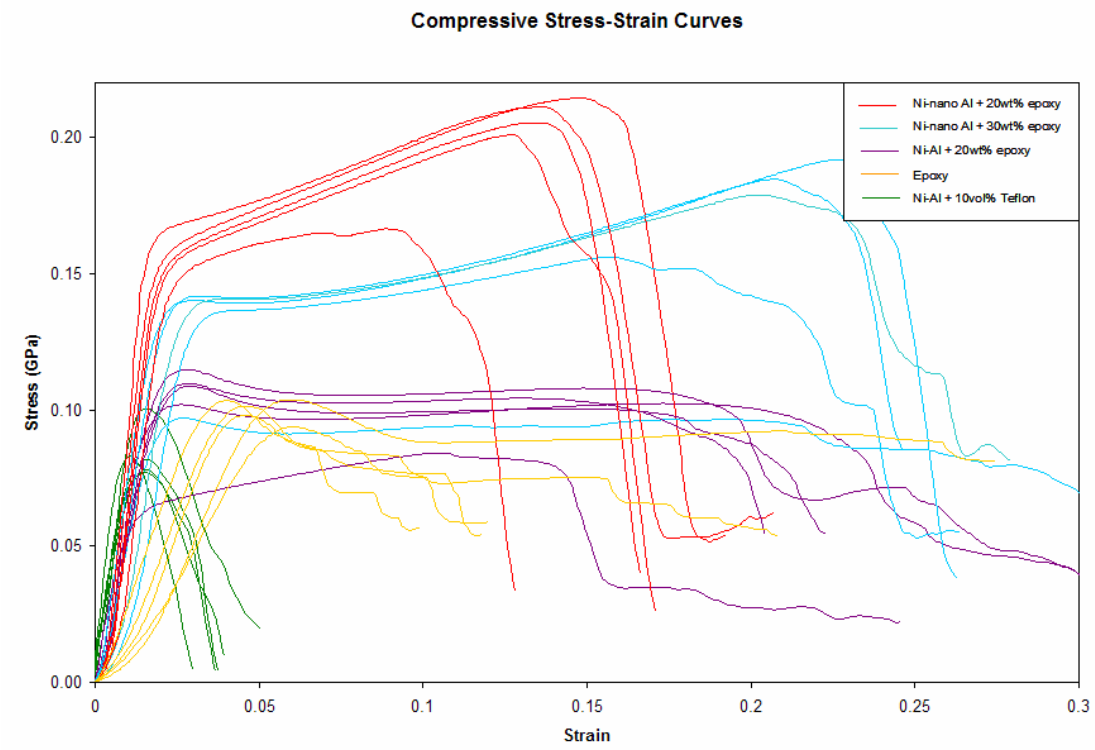

Figure 4-14: Stress-Strain curves generated during compression testing. The Ni+nano Al+20wt% epoxy samples (red curves) show the most superior static mechanical behavior in that they displayed the highest Elastic Modulus and compressive yield strength.

The stress-strain curves generated from compression tests show Ni+nano Al+20% epoxy has the highest yield strength, followed by Ni+nano Al+30% epoxy, Ni+Al+20% epoxy, pure epoxy, and finally Ni+Al+10% Teflon. Samples containing Teflon failed

immediately after their yield point, whereas those containing epoxy failed following some plastic deformation past the yield point. The cast samples containing nano Al particles show strain hardening, whereas those containing micron Al show negligible hardening effects. When comparing the two samples containing nano-particles, it can be seen that although the material with 30% epoxy has a lower compressive yield strength, it exhibits a higher strain to failure. Hence, while increasing epoxy content lowers the strength, it causes an increase in ductile behavior. The Ni+nano Al+20% epoxy sample showed the highest yield and ultimate strength when compared to the other samples.

Table 4-8: Elastic Modulus and Yield Strength values obtained from compression tests.

Material	**Theoretical Elastic Modulus (GPa)**	**Measured Elastic Modulus (GPa)**	**Theoretical Yield Strength (MPa)**	**Measured Yield Strength (MPa)**
Epoxy	4.4	3.01 ± 0.46	N/A	99.96 ± 4.11
Ni+Al+ 20wt% epoxy	7.64	7.47 ± 0.83	127.9	103.80 ± 12.15
Ni+nano Al+ 20wt% epoxy	7.64	11.43 ± 1.32	127.9	156.80 ± 4.44
Ni+nano Al+ 30wt% epoxy	6.32	7.21 ± 0.75	118.5	130.20 ± 19.24
Ni+Al+ 10vol% Teflon	9.55	8.86 ± 1.66	N/A	83.84 ± 9.33

Table 4-8 summarizes the static mechanical properties results and theoretical values for the elastic modulus and compressive yield strength, which were calculated using literature values of the constituents and the Reuss Rule of Mixtures. Theoretical yield strength values for the polymers do not exist since these properties can change drastically with different processing parameters, so the experimentally measured yield

strength of epoxy was used in the Rule of Mixtures. A comparison of the theoretical and measured values is shown in a bar graph in Figure 4-15.

The yield strength of epoxy was found to be only slightly improved by the addition of Ni+micron Al powders, but was greatly improved when Ni+nano Al powders were added. Ni+nano Al+20% epoxy had the highest yield strength (~157% of the yield strength of epoxy), followed by Ni+nano Al+30% epoxy (~130% of the yield strength of epoxy), and then Ni+Al+20% epoxy (~100% of the yield strength of epoxy). These values show a trend indicating that nano particles exhibit higher strength than micro-sized particles, and increasing epoxy content results in lower strength. The Ni+Al+10% Teflon samples had a yield strength lower than that of epoxy, and much lower than that of the reinforced epoxy samples. The elastic modulus values followed a similar trend as yield strength. Ni+nano Al+20% epoxy exhibited the highest elastic modulus, followed by the other two reinforced epoxy samples. The elastic modulus of the sample with Teflon is slightly higher than that of some epoxy samples, but also has a higher standard deviation.

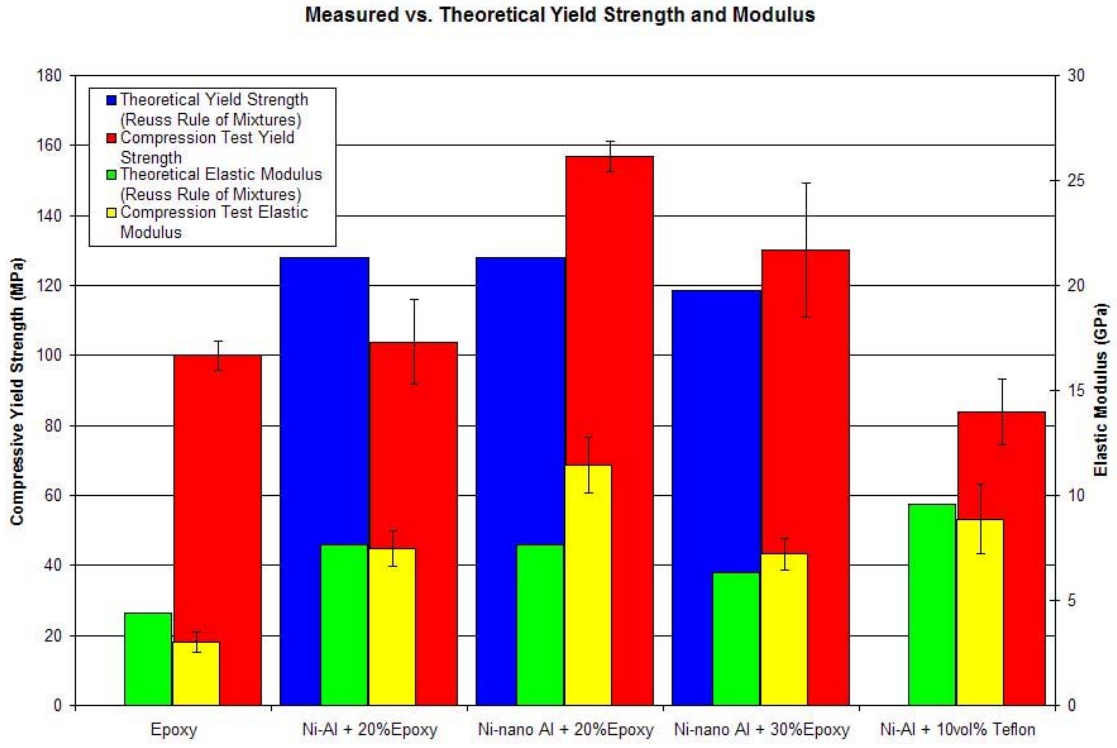

Figure 4-15: Elastic Modulus and Yield Strength values obtained from Compression Tests compared with Rule of Mixtures values. The superior mechanical properties exhibited by Ni+nano Al+20wt% epoxy are evident.

Figure 4-15 shows a plot comparing the elastic modulus and yield strength values obtained from compression tests with the values calculated using the Rule of Mixtures and literature values for the constituents. The elastic modulus value for epoxy measured from compression tests was below its calculated value. Compression test of Ni+Al+20% epoxy showed good agreement with calculated values, Ni+nano Al+30% epoxy was only slightly higher than calculated, and Ni+Al+10% Teflon was slightly lower, but had more variance. On the other hand, Ni+nano Al+20% epoxy exhibited an elastic modulus much higher than its calculated value. It can be seen that the compressive yield strength values follow a trend similar to that of the Elastic Moduli.

A photograph of typical compression samples after testing is shown in Figure 4-16. Samples exhibited barreling, which is typical in compression.

Figure 4-16: Photograph of Ni+nano Al+30wt% epoxy samples after compression testing. These show typical characteristics of the cast samples after compression tests.

Analysis of the fracture surfaces of the cast samples that were compression tested strongly resembled the fracture surfaces of intentionally fractured as-processed materials. The Ni+Al+20wt% epoxy samples showed a glassy fracture of the epoxy matrix around the Ni and Al particles, as seen in Figure 4-17a.

Figure 4-17b-e are images of samples containing nano Al particles; these images show a matrix composed of epoxy and nano Al. All of the deformation seen in these samples was within the epoxy matrix, which fractured around the Ni particles. In both the 20 and 30wt% epoxy samples, there are many locations where Ni pullout is evident.

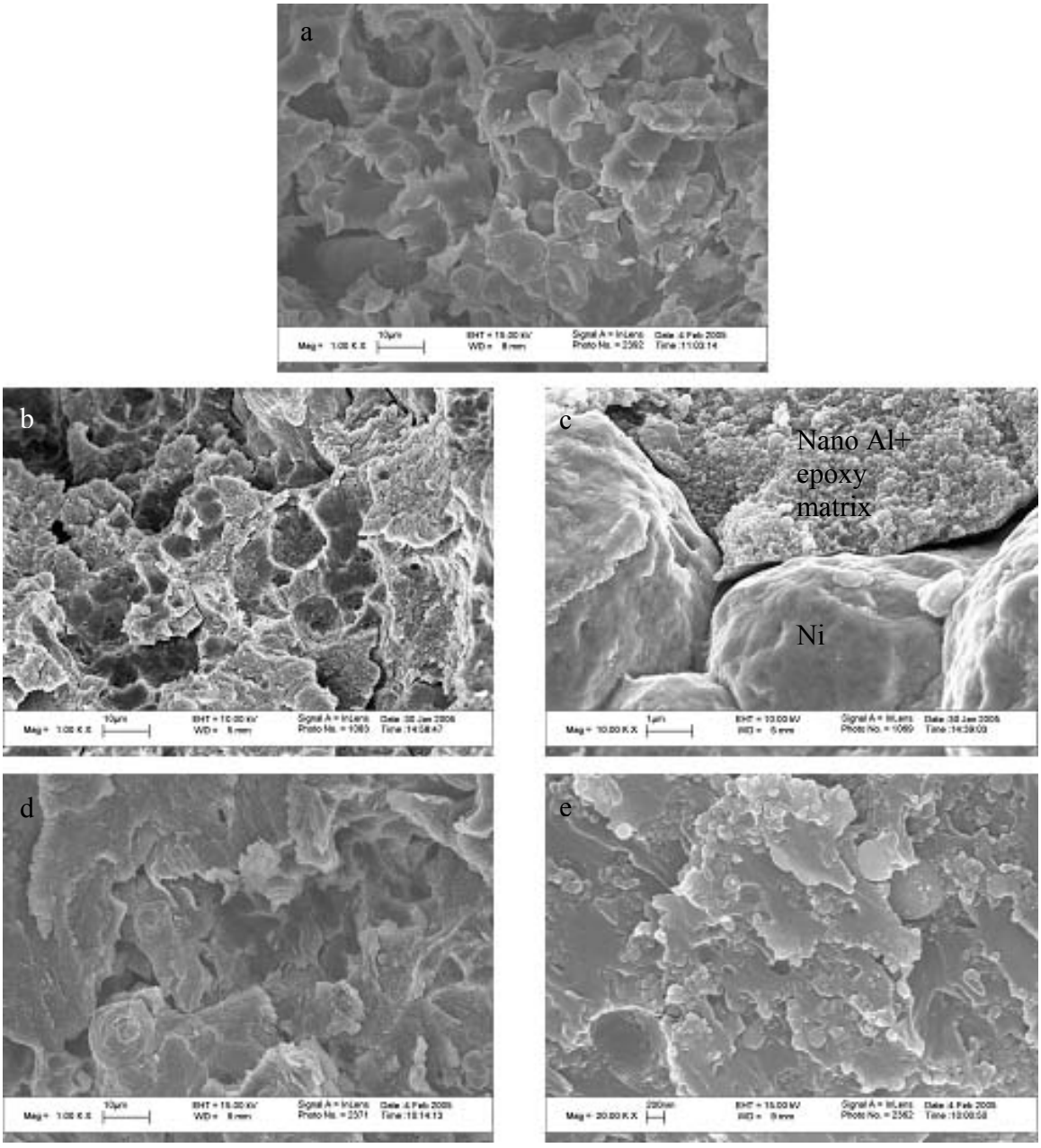

Figure 4-17: SEM images of fracture surfaces of Ni+Al/nano Al+epoxy compression test samples. (a) Ni+Al+20wt% epoxy compression sample fracture surface. (b) Ni+nano Al+20wt% epoxy compression sample fracture surface showing evidence of pullout of Ni particles. (c) Ni+nano Al+20wt% epoxy compression sample fracture surface showing fracture in epoxy matrix, around Ni particles. (d) Ni+nano Al+30wt% epoxy compression sample fracture surface. (e) Ni+nano Al+30wt% epoxy compression sample fracture surface showing fracture in epoxy matrix and pullout of nano Al particles.

4.3.2 Dynamic Mechanical Testing: Reverse Taylor Impact Tests

Six reverse anvil Taylor impact tests were performed on cast materials. For each test, digital images were taken to observe the transient deformation, and an analysis of the images was performed to obtain information about the dynamic mechanical properties of the materials. Velocity interferometry measurements were also taken, and the samples were recovered and analyzed after impact.

4.3.2.1 General Characteristics of Reverse Anvil Taylor Impact Test Results

The test specimens, listed in Table 4-9, were chosen to allow for comparison between Ni+Al+20wt% epoxy and Ni+nano Al+20wt% epoxy to determine the effects of Al particle size, and Ni+nano Al+20wt% epoxy and Ni+nano Al+30wt% epoxy to determine the effect of varying amounts of epoxy. Pure epoxy samples were tested in order to have a baseline for comparison since the reinforced composite materials were expected to behave in a similar manner to epoxy. Table 4-9 also lists the corresponding shot numbers, samples, and impact velocities.

Table 4-9: Shot number, material and impact velocity.

Shot	Sample	Impact Velocity
0423	Ni+nano Al + 30wt% epoxy	61 m/s
0429	Ni+Al + 20wt% epoxy	89 m/s
0430	Ni+nano Al + 20wt% epoxy	100 m/s
0431	Ni+nano Al + 30wt% epoxy	100 m/s
0434	epoxy	85 m/s
0501	epoxy	152 m/s

Experiments corresponding to shots 0423 and 0434 were performed at velocities insufficient to cause deformation. In each case, another shot was done using the same

sample material at a velocity adequate to generate deformation. Shots 0429, 0430, 0431 and 0501 all showed deformation.

For each shot, the Imacon high-speed digital camera was used to capture 16 images taken starting immediately before impact. The images from each shot are shown below in Figure 4-18, Figure 4-19, Figure 4-20, Figure 4-21, Figure 4-22, and Figure 4-23. The time after impact at which each image was taken is in the lower left hand corner of the frame. In each frame, the Al projectile with the steel flyer plate attached to the front can be seen coming from the left. The sample is the smaller cylinder in the center of the frame, and it is held in place by the PMMA target ring. In some cases, crush pins used to trigger the camera and the VISAR system can be seen above and below the sample.

Shot 0434, Epoxy sample, velocity = 85 m/s

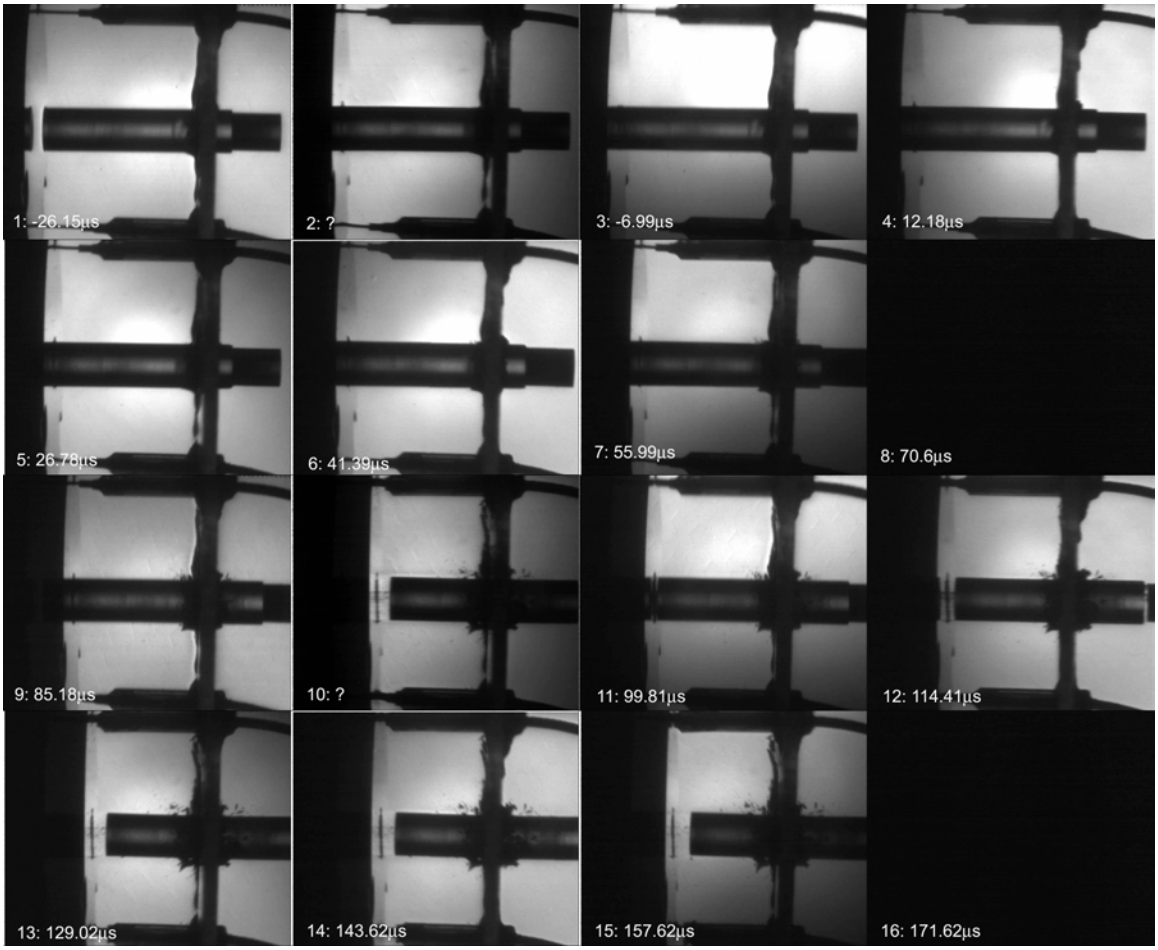

Figure 4-18: Images from Shot 0434. The lower left hand corner of each frame shows the frame number and the amount of time after impact at which the image was captured. This sample was at a low enough velocity that it did not deform. After impact, the sample appears to accelerate enough to pull away from the projectile.

The pure epoxy samples impacted at 85 m/s showed no deformation, as can be seen in Figure 4-18. The acceleration of the sample to a higher velocity than that of the projectile can be seen in these images. Following impact, this sample was not recovered as a full rod, but the fracture that did occur can most likely be attributed to the sample being hit by the projectile once inside the catch tank.

Shot 0501, Epoxy sample, velocity = 152 m/s

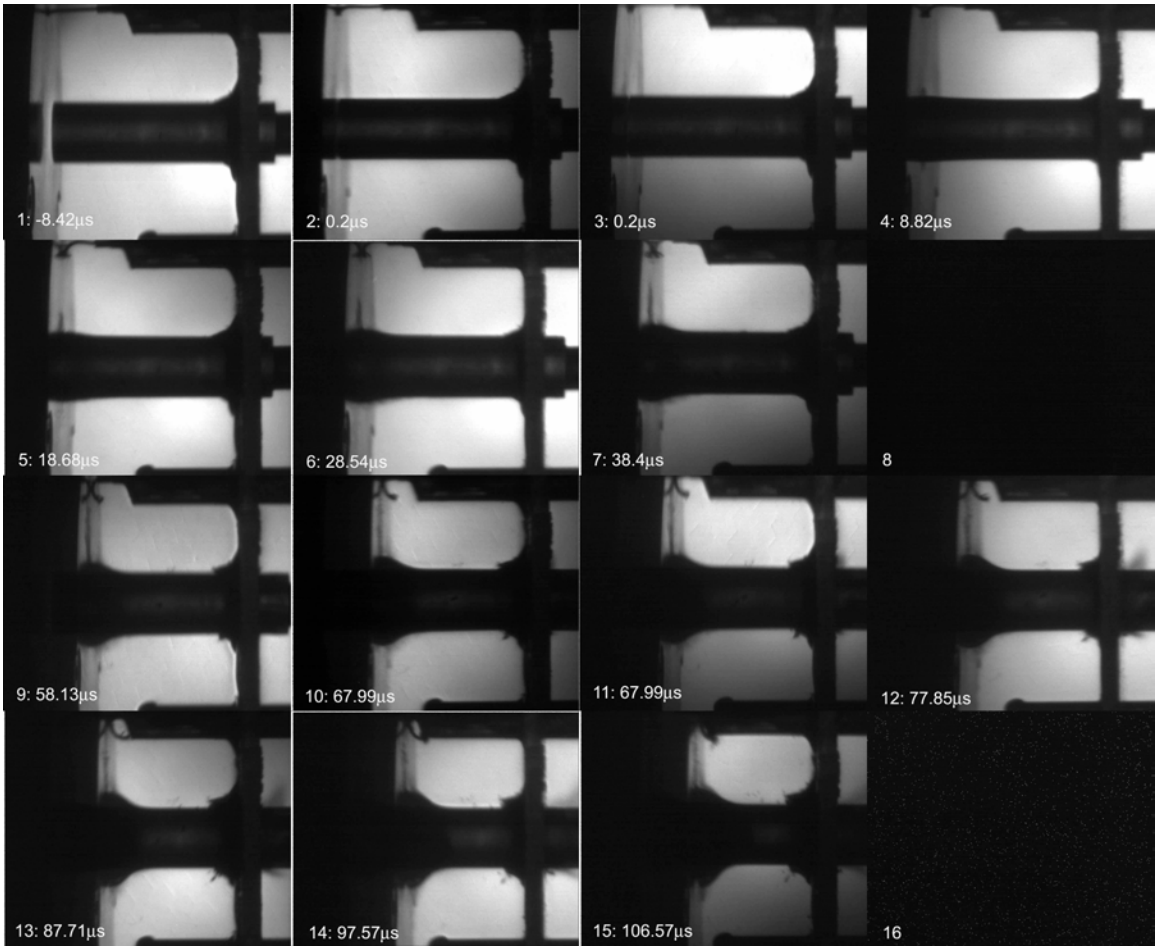

Figure 4-19: Images from Shot 0501. The epoxy sample shows mushrooming typical of deformation in the Taylor test. There is no evident fracture at the impact face within the time frame of the images.

In order to insure deformation in the pure epoxy sample, this shot was done at an impact velocity of 152 m/s. The images in Figure 4-19 show mushrooming of the impact face beginning around frame 4 (8.82 μs after impact), which continues throughout the extent of the images and appears to be approximately symmetric, indicating planar impact. There is no visible fracture at the impact face, which means that epoxy behavior is relatively ductile at this impact velocity. However, the sample fractured during recovery in the catch tank.

Shot 0429, Ni+Al+20wt% epoxy sample, velocity = 89 m/s

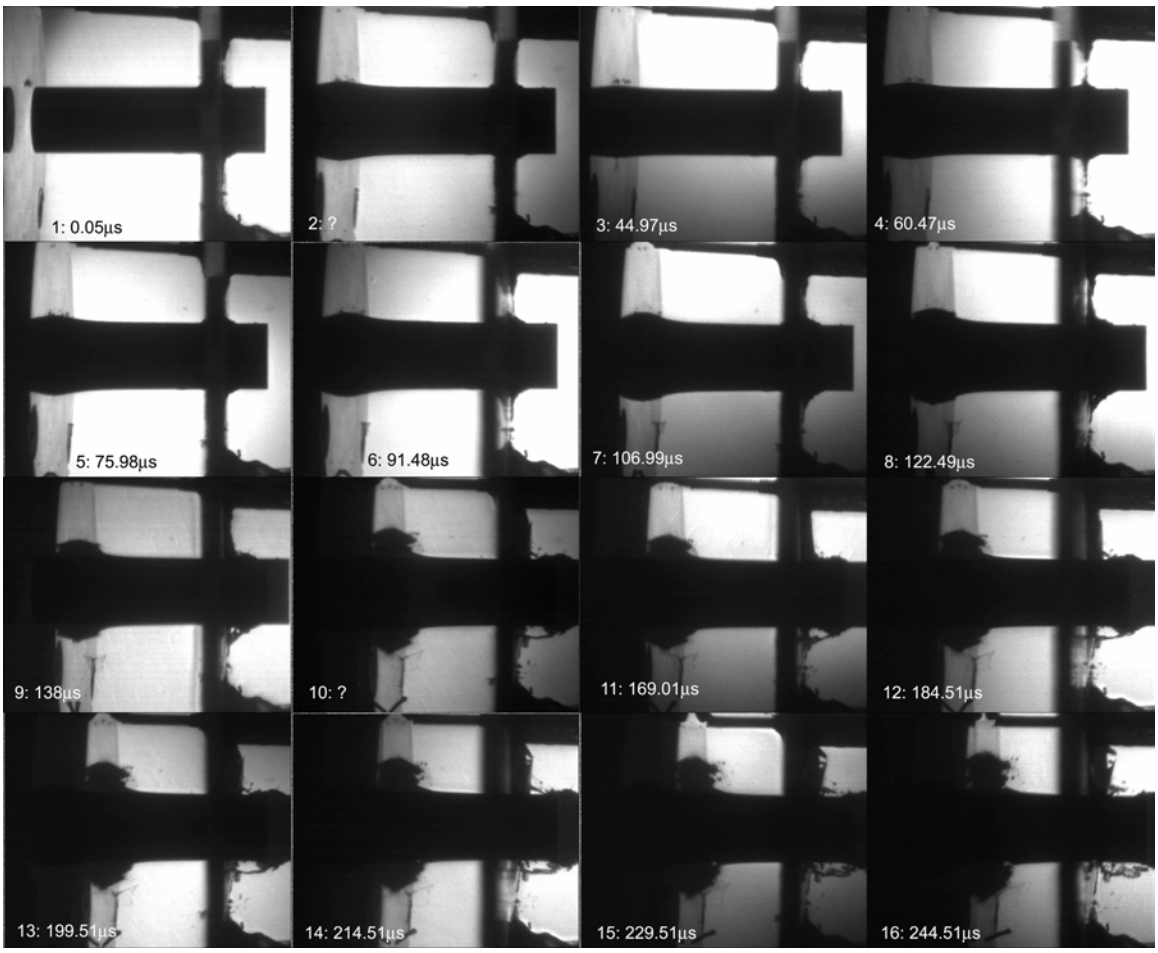

Figure 4-20: Images from Shot 0429. (Note: Framing times for 0429 are from camera trigger, not impact.) Mushrooming is seen in the early stages of deformation of this Ni+Al+20wt% epoxy sample, but there is fracture at the impact face in contrast to the deformation of the pure epoxy sample.

The Ni+Al+20% epoxy sample impacted at 89 m/s showed deformation, as illustrated in Figure 4-20. It should be noted that the times of these images are from camera trigger rather than impact since the standoff distance of the trigger pin was unknown. Also, frames 2 and 10 were taken out of sequence, so the timing on those is unknown. The early frames show mushrooming typical of Taylor test specimens. Deformation of the sample appears to be symmetric in these early stages. Starting around frame 9 (138 μs after camera trigger), fracture of the mushroomed region can be seen. The extent of fracture greatly increases through the last frame. Since fracture is seen in this sample, which was impacted at a low velocity, it can be assumed that the addition of Ni and Al to the epoxy causes a tendency toward more brittle behavior under dynamic impact loading.

Shot 0430, Ni+Al+20wt% epoxy sample, velocity = 100 m/s

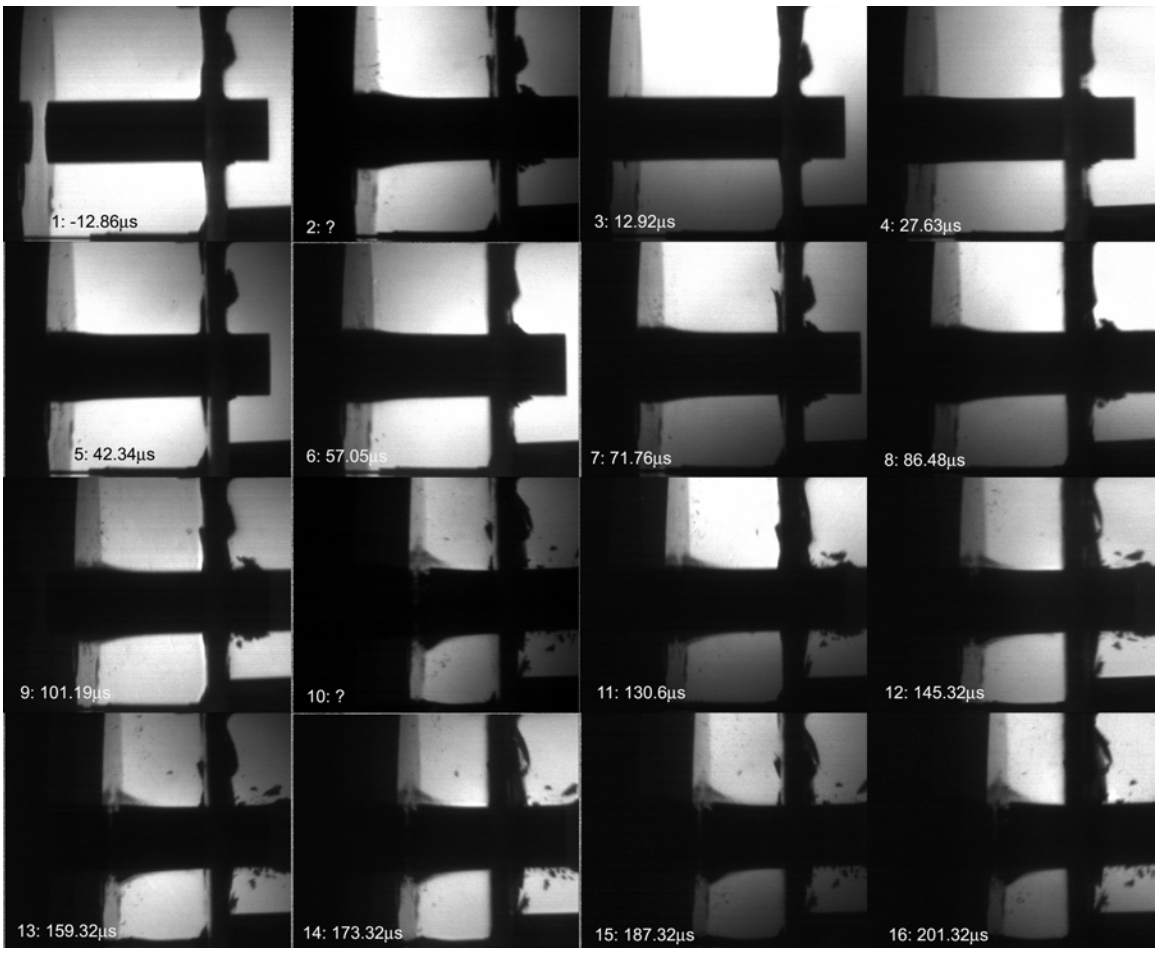

Figure 4-21: Images from Shot 0430 of Ni+nano Al+20wt% epoxy. Mushrooming is evident, but there is no obvious fracture at the impact face.

The Ni+nano Al+20% epoxy sample impacted at 100 m/s also showed deformation, as illustrated in Figure 4-21. In this case, mushrooming is also seen and appears to be approximately symmetric. There does not seem to be any obvious fracture at the impact face and the sample continues to mushroom, although there are fractured pieces where the sample is breaking away from the target ring. Consistent with the results of the static mechanical properties, it appears that the Ni+nano Al+20wt% epoxy cast sample is more fracture resistant than the sample containing the micron Al powder.

Shot 0423, Ni+nano Al+30wt% epoxy sample, velocity = 61 m/s

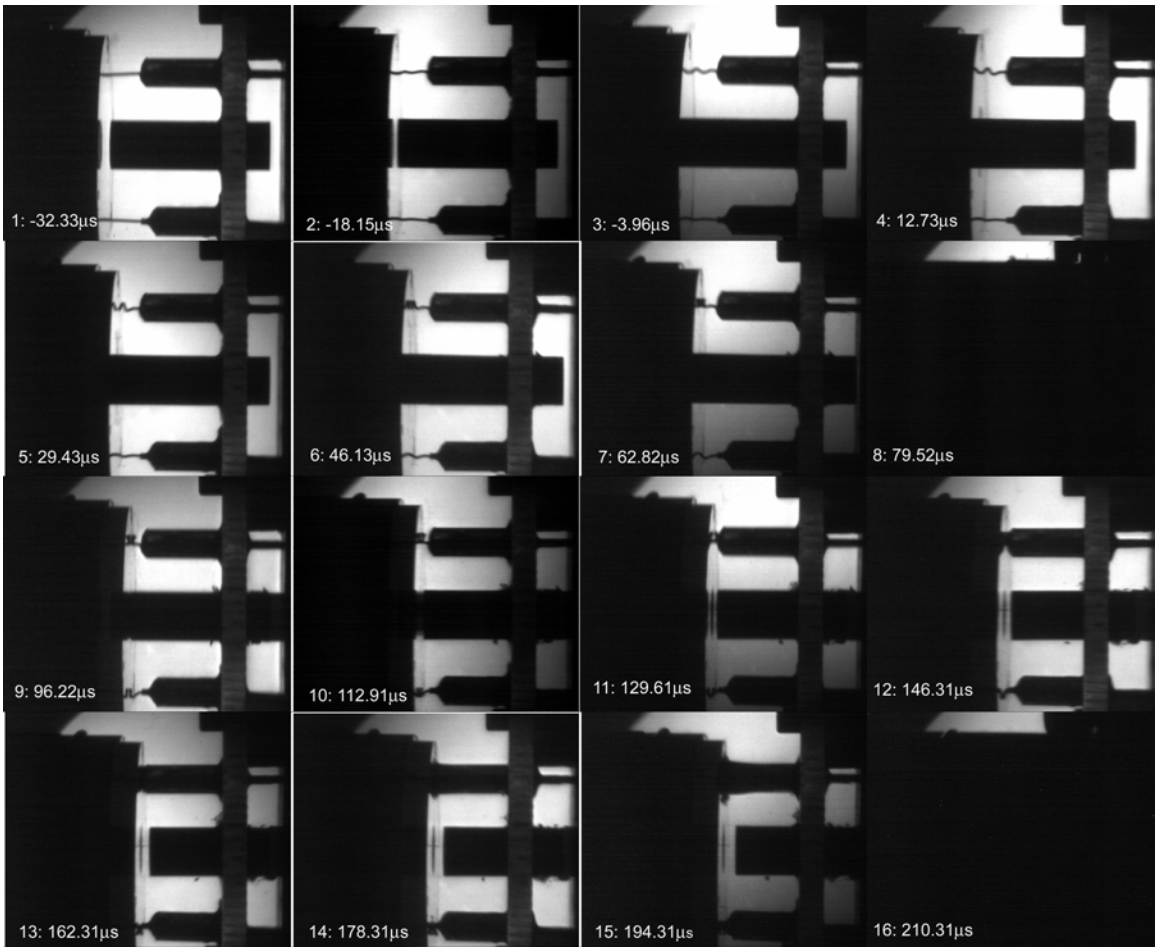

Figure 4-22: Images from Shot 0423. This Ni+nano Al+30wt% epoxy sample does not show deformation. The sample accelerates to a velocity higher than the impact velocity and pulls ahead of the projectile.

The Ni+nano Al+30% epoxy sample impacted at 61 m/s showed no deformation, as can be seen in the images in Figure 4-22. It can also be seen that after impact, the velocity of the sample increased to a velocity higher than that of the projectile, and the sample pulled away from the projectile as both continued to move. This gives the appearance that the sample has bounced of the face of the projectile.

Shot 0431, Ni+nano Al+30wt% epoxy sample, velocity = 100 m/s

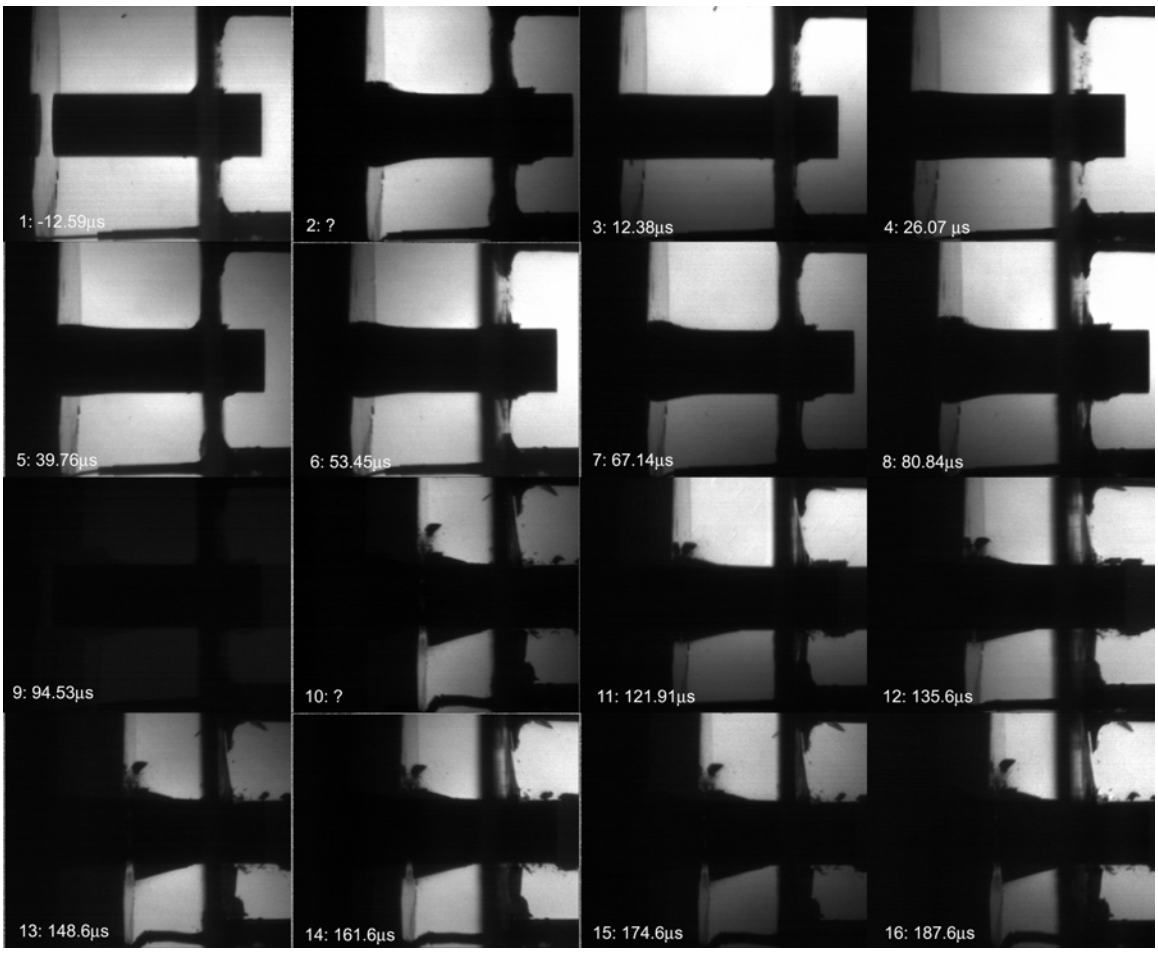

Figure 4-23: Images from Shot 0431. The Ni+nano Al+30wt% epoxy sample shows mushrooming, followed by large fracture pieces coming from the impact face.

The Ni+nano Al+30% epoxy sample impacted at 100 m/s, shows the symmetric mushrooming at early stages of deformation. With continued deformation, relatively large fractured pieces appear to be coming off the deformed region starting around frame 11 (121.91 μs), as shown in Figure 4-23. The occurrence of fracture in this sample (in contrast to the Ni+nano Al+20wt% epoxy sample impacted at a similar velocity) illustrates that increasing epoxy content reduces the strain to failure and promotes fracture. However, this contradicts the ductile behavior seen in pure epoxy, which did not show any signs of fracture at 152 m/s.

Overall, it can be concluded from the generalized analysis of the images showing transient deformation patterns that pure epoxy behaves in a rather ductile manner relative to particle reinforced epoxy samples, which show rather brittle fracture at much lower velocities. At the same time, the cast sample containing Ni+nano Al+20wt% epoxy shows a rather interesting deformation and failure response.

4.3.2.2 House Analysis of Dynamic Stress-Strain Curves

The analysis of Taylor impact tests by House *et al.* [38] was used to interpret the high deformation rate experiments and produce dynamic stress-strain curves, as previously described in Sections 2.3.1 and 3.2.3.3. This analysis was done on the four shots that showed deformation, one of each sample type. The analysis produces a series of four plots: radius vs. axial position and areal strain vs. axial position, from which stress vs. strain, and strain rate vs. strain curves are obtained.

Because this analysis was developed for ductile materials, there are limitations when using it for materials systems that exhibit fracture. Thus, there are some cases, as explained later in the section, where unusual traces are produced and are not valid.

Additionally, due to the nature of the measurements, there is some error associated with the film data reduction.

Shot 0501, Epoxy sample, velocity = 152 m/s

Figure 4-24: Deformation profiles used in House Analysis of pure epoxy sample impacted at 152 m/s in shot 0501.

Figure 4-24 shows the images of deformed sample corresponding to image frames taken at specific times that were used for the analysis.

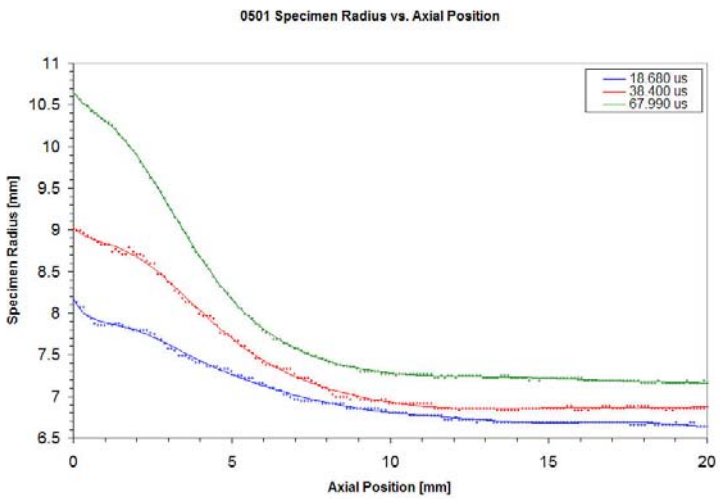

Figure 4-25: Pure epoxy shot 0501 Specimen Radius vs. Axial Position plot generated using the House Analysis. This plot shows an increase in specimen radius with time, as deformation proceeds. It can also be seen that the radius remains un-deformed for much of the length of the specimen.

As described in Section 3.2.3.3, the plot of specimen radius vs. axial position was generated by isolating the sample profile, and then taking a vertical profile. The vertical lines in the profile were measured along the length of the specimen to generate the radius vs. axial position plot shown in Figure 4-25 for three frames (18.68, 38.40 and 68.99 μs). These three frames were chosen by first doing the sample isolation and vertical profile for each frame from impact until fracture (no fracture occurred in this case) and then choosing three representative images. The plot shows evidence of mushrooming increasing with time (as was observed in the images in Figure 4-19), and the sample radius levels off around the initial radius of ~7 mm at an axial position of 9 mm. It can be seen that the three curves do not level off at the same value of un-deformed radius; this is due to the pixel resolution error in measurement from the film data reduction.

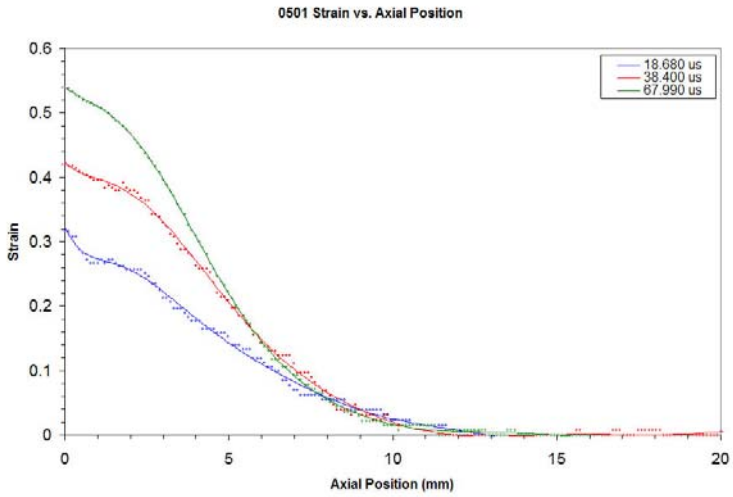

Figure 4-26: 0501 Strain vs. Axial Position plot generated using the House Analysis. This plot shows trends similar to those seen in the specimen radius vs. axial position plot, with increasing amounts of strain at later times.

The radius vs. axial position data generated in the previous figure (Figure 4-25) were then re-plotted as areal strain vs. axial position (Figure 4-26) using Taylor's definition of strain (Equation 2-6). The sample experienced maximum strains of 0.32, 0.42 and 0.54 at the chosen times. The specimen appears to be strained up to an axial position of ~12 mm, at which point it remains unstrained.

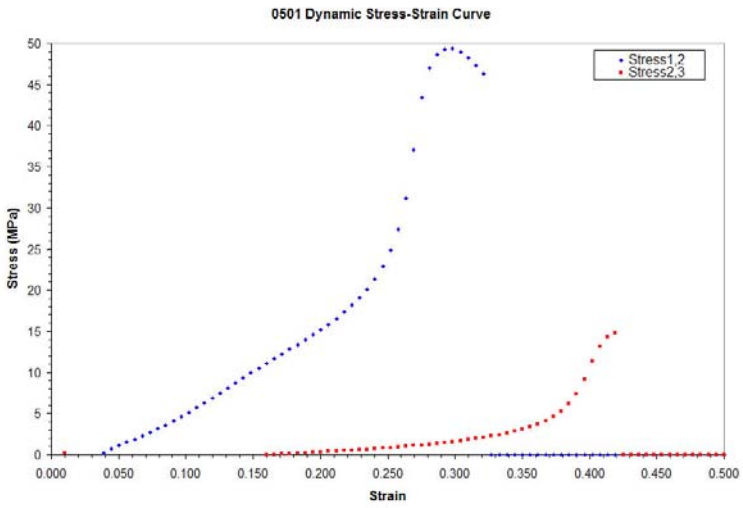

Figure 4-27: Pure epoxy shot 0501 dynamic Stress-Strain Curves generated using the House Analysis. Each trace in the plot shows the stress generated in the time between two chosen frames, and the corresponding amount of strain.

The dynamic stress-strain curve for shot 0501 was then generated using the series of equations described in Section 2.3.1, and is shown in Figure 4-27. First, the back end speed of the sample was calculated by measuring the change in length of the specimen. Next, a series of plastic wave speeds were determined, where each wave speed is the average Eulerian wave speed calculated for a specific strain over a specific time interval. Finally, Equation 2-12 was used to relate stress and strain. The resulting dynamic stress-strain curve shows two curves because the stress and strain are taken between two frames, such that the first curve represents the stress-strain in the first time interval (18.68-38.40 μs), whereas the second curve represents the stress-strain in the second time interval (38.40-67.99 μs).

The stress-strain curve for the pure epoxy sample impacted at 152 m/s and shown in Figure 4-27, illustrates an increase in stress that is almost linear up to a strain of 0.25 and a stress of 20 MPa, and then it increases drastically to a maximum stress of 50 MPa

at a strain of 0.3. After this maximum, the stress decreases rapidly. The stress-strain in the second time interval shows the same linear increase to a stress of 4 MPa at a strain of 0.37. The stress then increases to 15 MPa at a strain of 0.42, where the stress rapidly decreases. Since these stress-strain curves are dynamic, each curve applies only to the specific transient time interval that it is calculated for. For example, for the first time interval shown in Figure 4-27, a 30% strain is supported by a stress of 50 MPa, whereas for the second time interval a 42% strain is supported by a stress of ~15MPa.

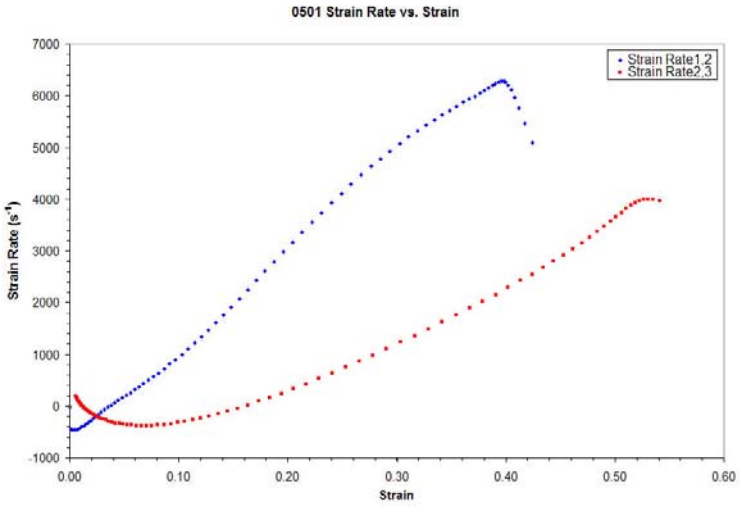

Figure 4-28: Pure epoxy shot 0501 Strain Rate vs. Strain plot generated using the House Analysis. This plot correlates the strain rate to the amount of strain in the sample during the particular time frames examined.

A plot of strain rate vs. strain can also be generated from the House Analysis by examining the strain at a particular axial position over a time interval. Figure 4-28 above shows the plot of strain rate vs. strain for the epoxy sample impacted at 152 m/s. There are again two curves in this plot since the calculations are done over the two time

intervals between the three selected frames. The strain rate is expected to build up from zero ahead of the front to some finite maximum value and then drop back down to zero [38]. Some elements of this behavior are roughly seen in the plot produced. The traces do begin near zero, however they go negative first, therefore the analysis is not valid in this portion. After this initial region, however, the traces do increase to a maximum value and then decrease again before dropping off. The maximum strain rates seen in this plot are ~6000 s^{-1} at 38% strain and 4000 s^{-1} at 52% strain, respectively. Again, these values are specific to the exact strain rate, strain and time interval. These strain rate values would change depending on the frames chosen, for example, earlier frames would exhibit higher strain rates.

Shot 0429, Ni+Al+20wt% epxy sample, velocity = 89 m/s

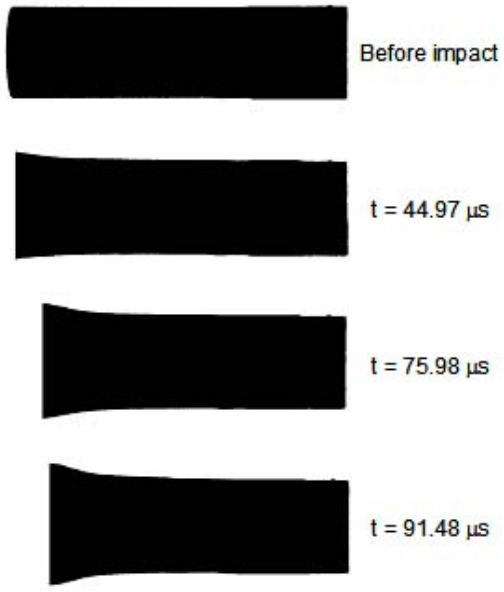

Figure 4-29: Deformation profiles used in House Analysis of Ni+Al+20wt% epoxy sample impacted at 89 m/s in shot 0429.

Figure 4-29 shows deformation profiles corresponding to image frames taken at specific times that were used for the analysis. Analysis of the Ni+Al+20wt% epoxy sample (shot 0429) produced the plot of radius vs. axial position shown in Figure 4-30. This sample also had an initial radius of ~7 mm, as can be seen by the leveling off of the radius vs. axial position curve. The frame times chosen in this analysis are 44.97, 75.98 and 91.48 μs from camera trigger. The maximum strains experienced by this sample at the chosen times are 0.39, 0.32 and 0.22, as can be seen in the plot of areal strain vs. axial position shown in Figure 4-31.

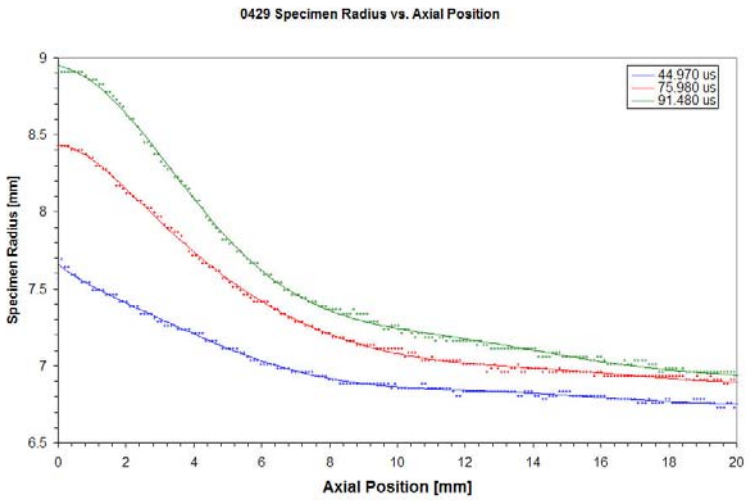

Figure 4-30: Ni+Al+20wt% epoxy shot 0429 Specimen Radius vs. Axial Position plot generated using the House Analysis.

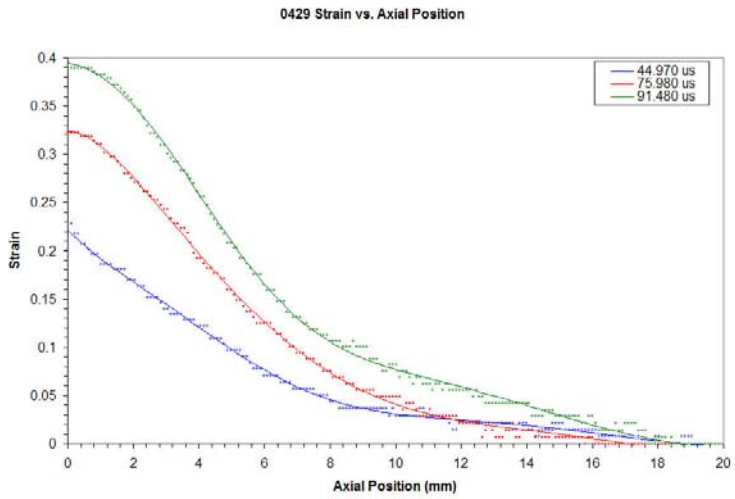

Figure 4-31: Ni+Al+20wt% epoxy shot 0429 Strain vs. Axial Position plot generated using the House Analysis.

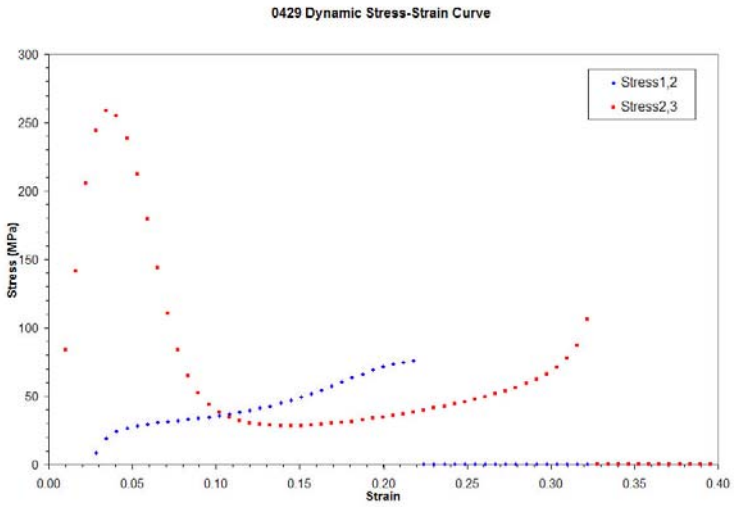

Figure 4-32: Ni+Al+20wt% epoxy shot 0429 Dynamic Stress-Strain Curve generated using the House Analysis.

Figure 4-32 and Figure 4-33 are the corresponding stress vs. strain and strain rate vs. strain plots. These dynamic stress-strain curves generated from shot 0429 (Ni+Al+20% epoxy) show an unusual trend, which needs to be classified and better understood.

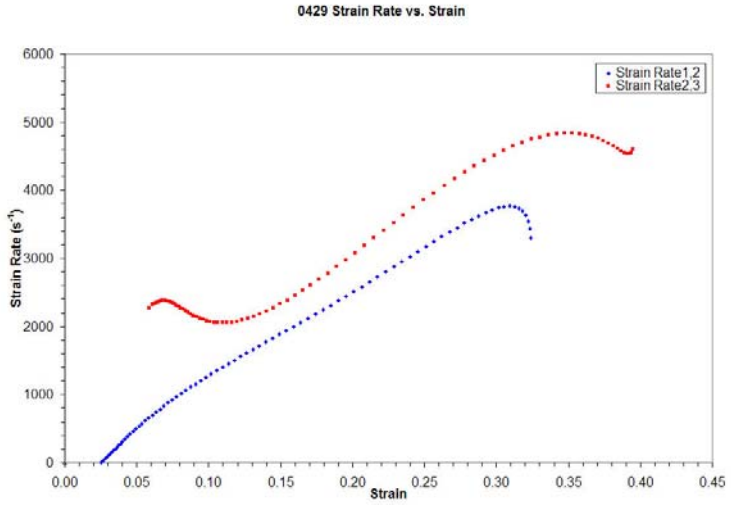

Figure 4-33: Ni+Al+20wt% epoxy shot 0429 Strain Rate vs. Strain plot generated using the House Analysis.

The strain rate vs. strain curves shown in Figure 4-33 shows typical behavior during the first time interval, with strain rate increasing to a maximum, followed by a decrease. This curve shows a maximum strain rate of ~3900 s^{-1} for a strain of 31%.

Shot 0430, Ni+nano Al+20wt% epoxy sample, velocity = 100 m/s

Figure 4-34: Deformation profiles used in House Analysis of Ni+nano Al+20wt% epoxy sample impacted at 100 m/s in shot 0430.

Figure 4-34 shows the deformation profiles corresponding to image frames taken at specific times that were used for the analysis. The radius vs. axial position and strain vs. axial position plots for Ni+nano Al+20% epoxy are shown in Figure 4-35 and Figure 4-36, respectively. The frames chosen for this analysis were at 12.92, 57.05 and 86.48 µs after impact.

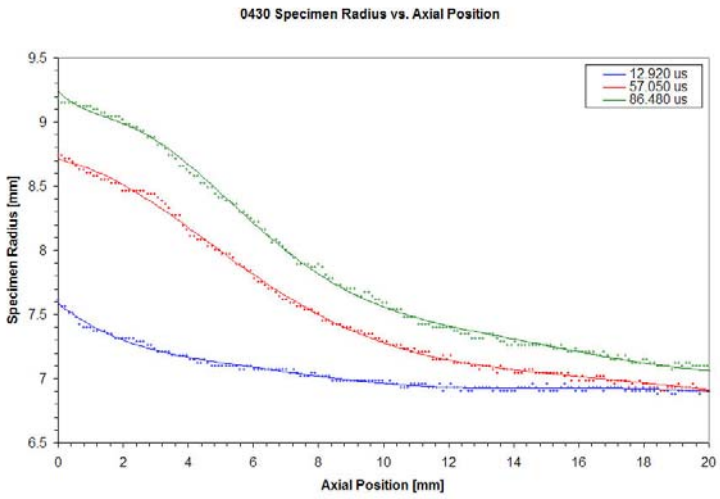

Figure 4-35: Ni+nano Al+20wt% epoxy shot 0430 Specimen Radius vs. Axial Position plot generated using the House Analysis.

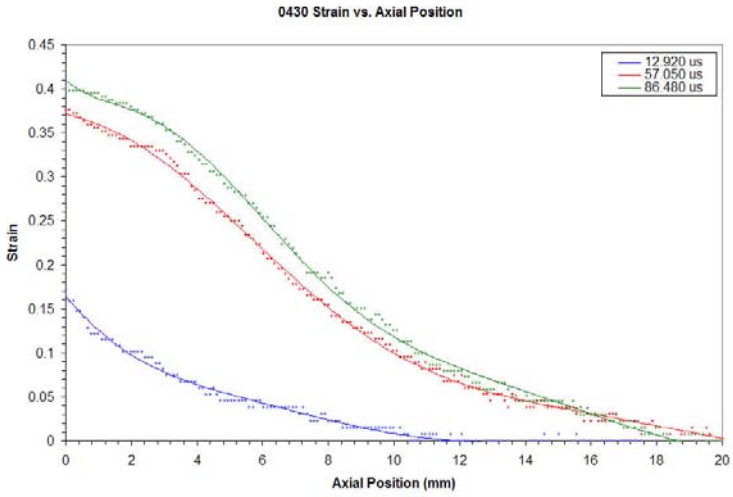

Figure 4-36: Ni+nano Al+20wt% epoxy shot 0430 Strain vs. Axial Position plot generated using the House Analysis.

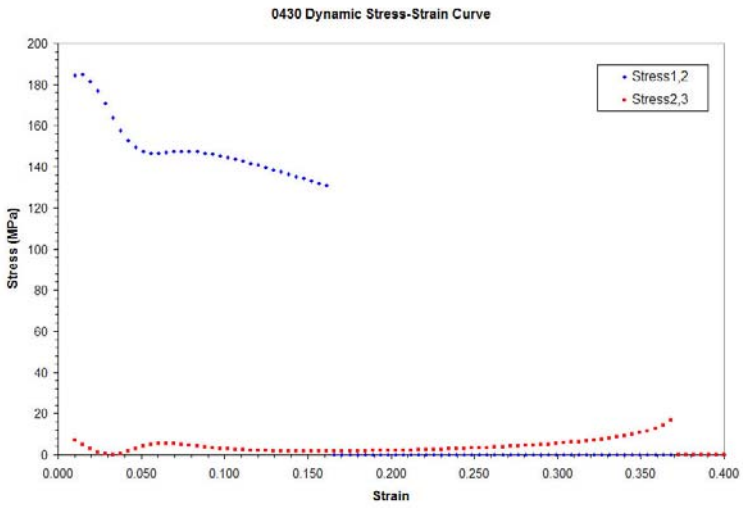

Figure 4-37: Ni+Al+20wt% epoxy shot 0430 Dynamic Stress-Strain Curve generated using the House Analysis.

The corresponding dynamic stress-strain curves (Figure 4-37) for shot 0430 show a more typical behavior in that less stress is required to support the significantly lower strains generated at later times. During the first time interval, a 5% strain is supported by 150 MPa of stress, but during the second time interval, only ~5 MPa of stress is required. The strain rate vs. strain shown in Figure 4-38 reveals a typical behavior. It can also be noted that a much higher strain rate is generated during the first time interval, with the large degree of strain generated.

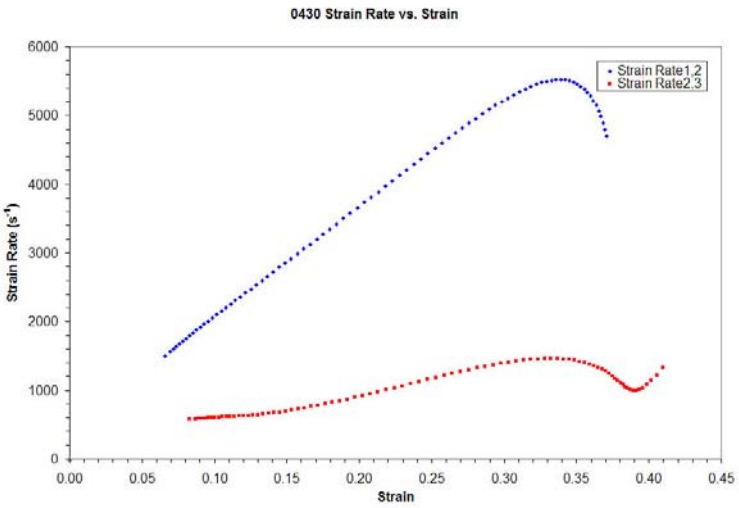

Figure 4-38: Ni+nano Al+20wt% epoxy shot 0430 Strain Rate vs. Strain plot generated using the House Analysis.

Shot 0431, Ni+nano Al+30wt% epoxy sample, velocity = 100 m/s

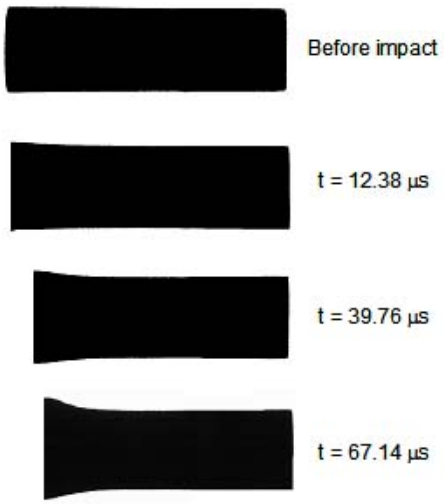

Figure 4-39: Deformation profiles used in House Analysis of Ni+nano Al+30wt% epoxy shot sample impacted at 100 m/s in shot 0431.

Figure 4-39 shows the deformation profiles corresponding to the image frames taken at specific times that were used for the analysis.

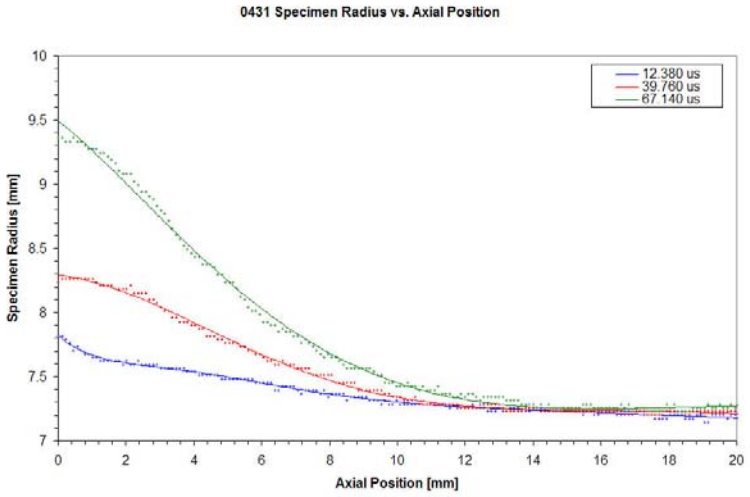

Figure 4-40: Ni+nano Al+30wt% epoxy shot 0431 Specimen Radius vs. Axial Position plot generated using the House Analysis.

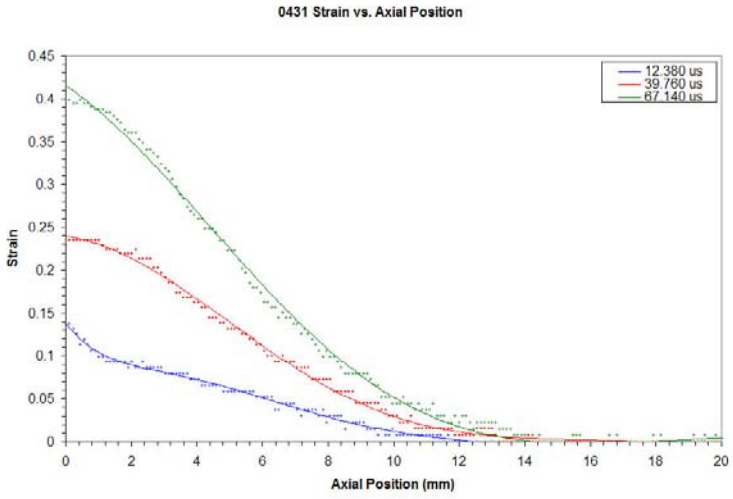

Figure 4-41: Ni+nano Al+30wt% epoxy shot 0431 Strain vs. Axial Position plot generated using the House Analysis.

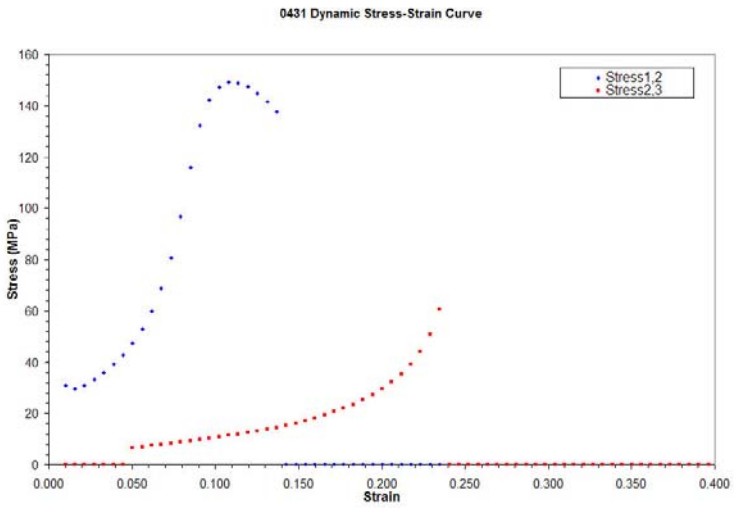

Figure 4-42: Ni+nano Al+30wt% epoxy shot 0431 Dynamic Stress-Strain Curves generated using the House Analysis.

Plots of radius vs. axial length (Figure 4-40) and strain vs. axial length (Figure 4-41) show typical trends. The dynamic stress-strain curve, shown in Figure 4-42, reveals higher stresses necessary at earlier times. This is in conjunction with higher strain rates generated while producing a given strain, as seen in Figure 4-43.

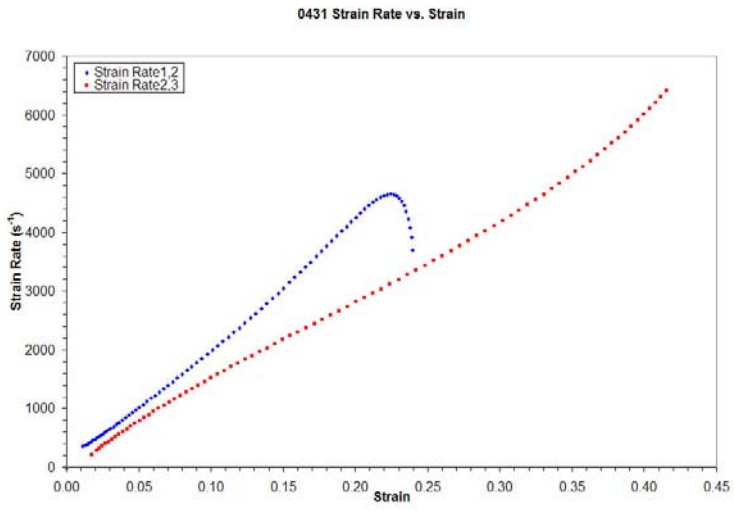

Figure 4-43: Ni+nano Al+30wt% epoxy shot 0431 Strain Rate vs. Strain plot generated using the House Analysis.

Although the House Analysis is useful for validation of models, it is difficult to use it as a basis of comparison between different materials. Since the experiments involve different materials and time frames used to compare these effects, it is not possible to obtain direct comparisons.

In an effort to make some comparison between the shots, and therefore the different materials, the maximum strain experienced before fracture was examined, and is listed in Table 4-10 and shown in a bar graph in Figure 4-44. This maximum strain was determined from isolating the last available image before fracture was evident and then using a vertical profile to measure the size of the radius of the impact face.

Table 4-10: Maximum strain experienced before fracture occurred for each shot showing deformation.

Shot	**Material**	**Maximum Strain Before Fracture**
0501	Epoxy	>0.677
0429	Ni+Al+20% epoxy	0.530
0430	Ni+nano Al+20% epoxy	0.547
0431	Ni+nano Al+30% epoxy	0.505

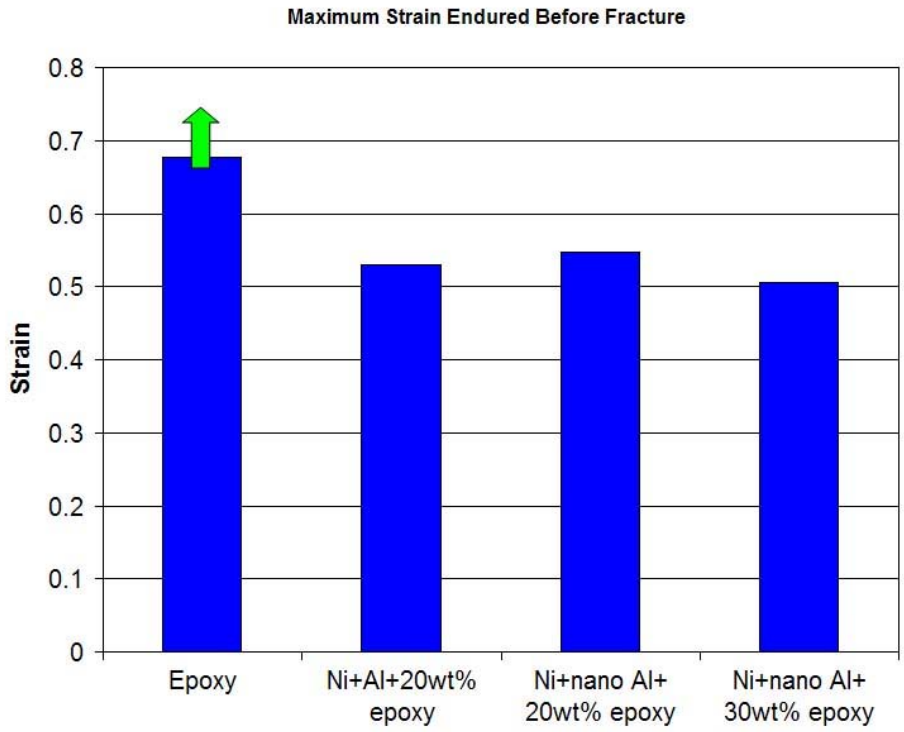

Figure 4-44: Maximum strain experienced before fracture in each material.

In the case of shot 0501 (epoxy), fracture was not observed in any of the images, so the last frame was used to determine the maximum strain. In actuality, the maximum strain endured by this epoxy sample before fracture is higher than 67.7%. Shot 0430 (Ni+nano Al+20% epoxy) only started to show a small amount of fracture, so again the last frame was used to determine strain. In all cases where the sample was a reinforced epoxy, fracture occurred at least to a small degree at a strain much below where epoxy was still deforming in a ductile manner. Out of the three reinforced epoxy materials, Ni+nano Al+20% epoxy showed the best dynamic failure resistance (survived a larger amount of strain before fracture). In each case, the maximum strain observed before

fracture is much higher than the maximum strain before failure observed during compression tests, which were in the range of 0.15-0.25.

4.3.2.3 Reverse Anvil Taylor Impact Test Results Based on Velocity Interferometry

Velocity interferometry (VISAR) was used to determine the velocity of the back surface of the sample, or the free surface velocity. The raw data and the free surface velocity traces for each experiment are shown in Figure 4-45, Figure 4-46, Figure 4-47, Figure 4-48, Figure 4-49, and Figure 4-50. Each plot has two blue traces representing the electrical voltage histories, which are transduced from the light fringes, or oscillations between bright and dark light. The y-axis scale for these traces is on the left side of each plot. The black trace is the free surface velocity, which corresponds to the y-axis scale shown on the right side of each plot. Since the velocity trace is calculated from the interactions between the two light fringes, it can be seen that the time at which these two traces start to change is when the free surface velocity departs from zero. The x-axis of these plots is time after impact. These plots are originally generated with the x-axis indicating time after the VISAR oscilloscope is triggered. Because the impact velocity is calculated and the standoff between the VISAR trigger crush pin and the sample face is known, the time between trigger and impact can be calculated and subtracted in order to generate plots dependent on time after impact. This was done in all cases where all of the necessary values were known.

It can be seen in the figures that the free surface velocity does not depart from zero until many microseconds after impact because the back surface of the sample doesn't move until the elastic wave travels from the impact face all the way to the back surface. Another noticeable feature is the reverberations, which are caused because once

the elastic wave travels as a compressive wave to the back surface of the sample, it bounces back as a tensile release wave and continues to attenuate back and forth between the plastic wave front and the back surface, thus subjecting the sample to repeated tension and compression. The reverberations are also affected by the waves reflecting off of the radial surface of the sample. To minimize these effects, a similar sample radius was used for all shots.

The VISAR data for pure epoxy (shots 0434 and 0501, corresponding to velocities of 85 and 152 m/s, respectively) are shown in Figure 4-45 and Figure 4-46. All plots show very clean traces due to the high signal that was achieved off of the gold coated glass window. VISAR traces from 0429 (Ni+Al+20% epoxy), 0430 (Ni+nano Al+20% epoxy), 0423 and 0431 (both Ni+nano Al+30% epoxy) are shown in Figure 4-47, Figure 4-48, Figure 4-49 and Figure 4-50, respectively. Table 4-11 summarizes the main features of all of these plots.

The VISAR trace for shot 0429 shows some unusual features that need further discussion. Since it was unknown which crush pin triggered the VISAR oscilloscopes, the plot is a function of time after trigger rather than time after impact. The velocity trace for this shot does not show a clear departure from zero as is seen in all other plots; which makes calculation of the rise time difficult. Also, no reverberations are seen in this velocity trace. It is suspected that the trigger pin may have hit the inside of the screw securing the flyer plate to the projectile. This small extra distance between the face of the flyer and the inside of the screw was not expected, and may explain the unusual behavior of the velocity trace, and would also affect the calculations for the oscilloscope timing.

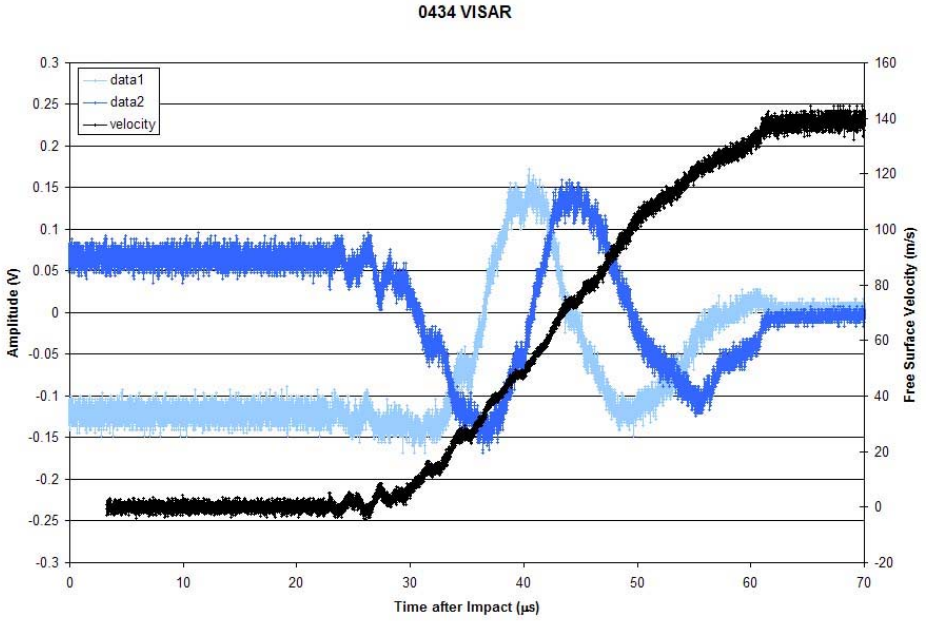

Figure 4-45: VISAR traces from pure epoxy shot 0434, impacted at 85 m/s, showing the velocity of the back surface of the sample.

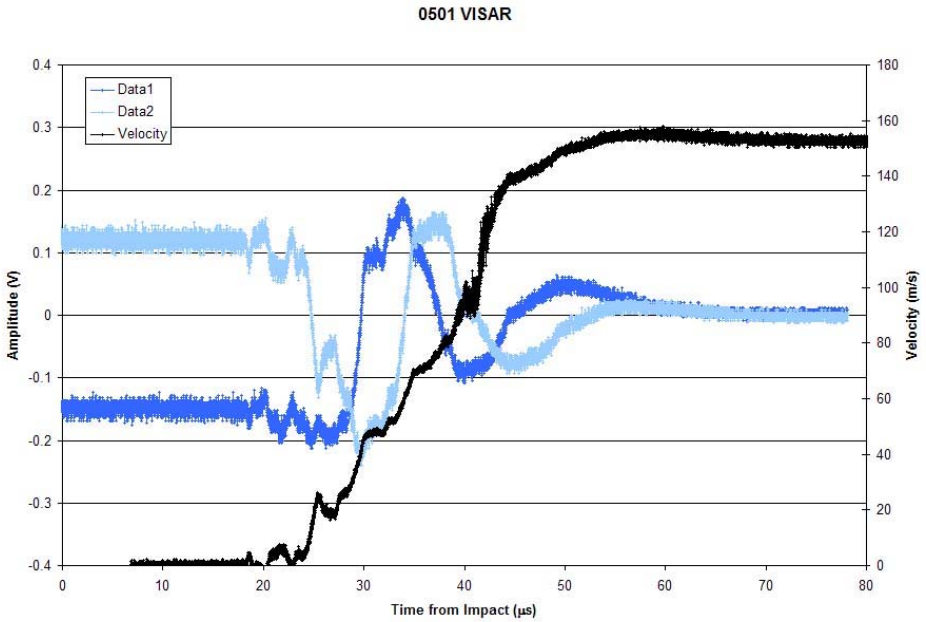

Figure 4-46: VISAR traces from pure epoxy shot 0501, impacted at 152 m/s, showing the velocity of the back surface of the sample.

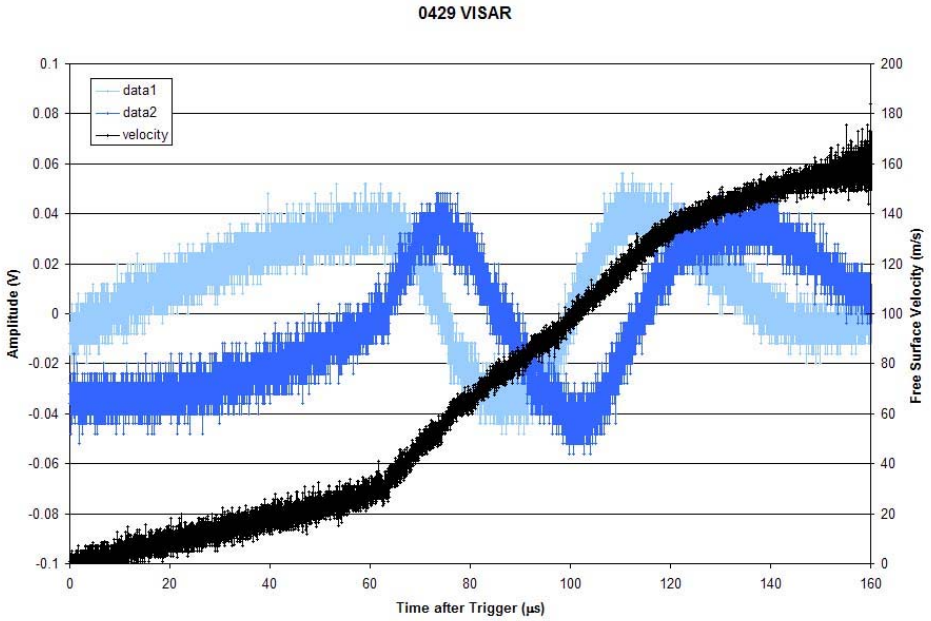

Figure 4-47: VISAR traces from Ni+Al+20wt% epoxy shot 0429, impacted at 89 m/s, showing the velocity of the back surface of the sample.

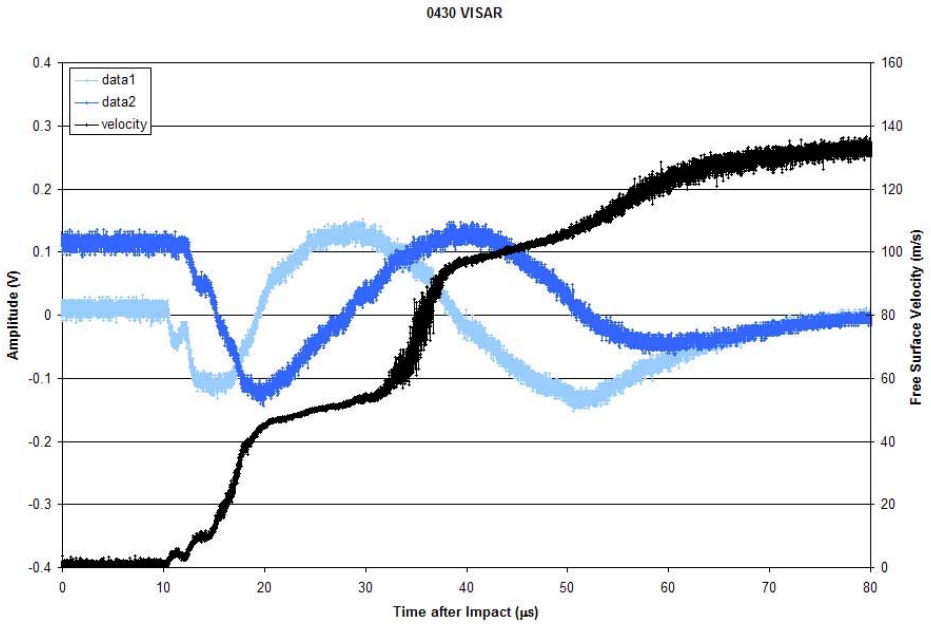

Figure 4-48: VISAR traces from Ni+nano Al+20wt% epoxy shot 0430, impacted at 100 m/s, showing the velocity of the back surface of the sample.

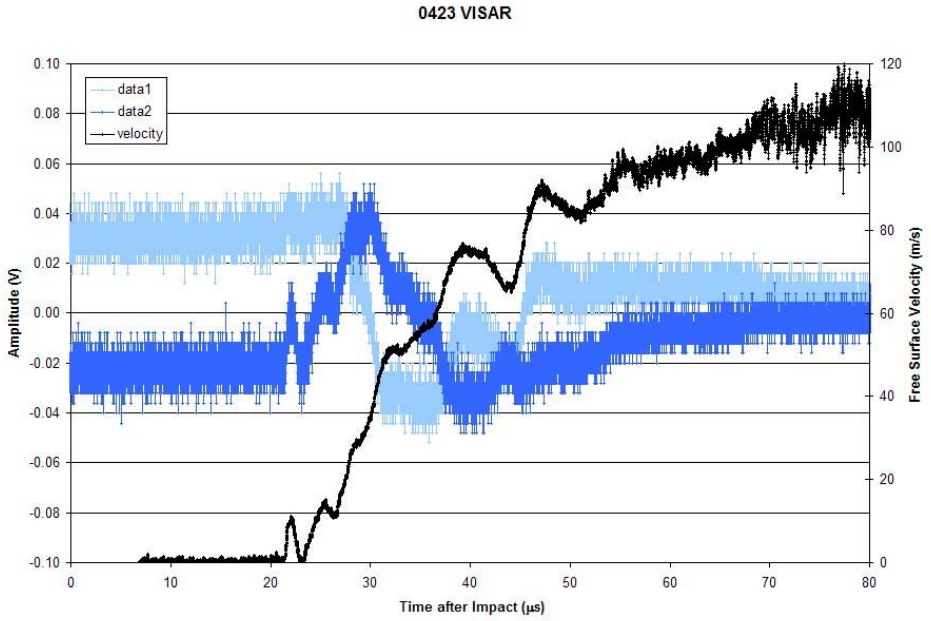

Figure 4-49: VISAR traces from Ni+nano Al+30wt% epoxy shot 0423, impacted at 61 m/s, showing the velocity of the back surface of the sample.

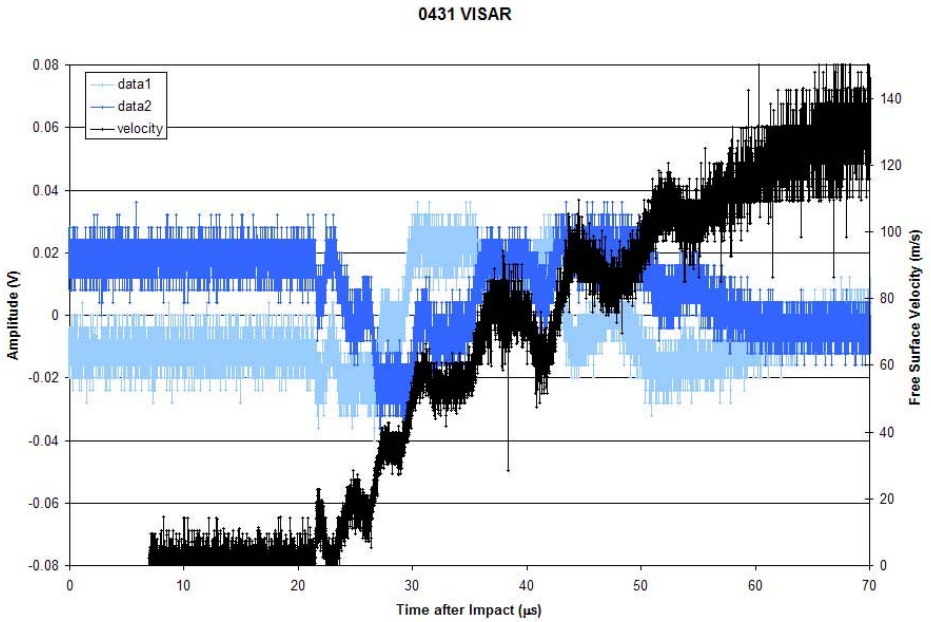

Figure 4-50: VISAR traces from Ni+nano Al+30wt% epoxy shot 0431, impacted at 100 m/s, showing the velocity of the back surface of the sample.

The reverberations seen in the VISAR velocity profile are a function of the tension and compression waves traveling through the sample, as well as radial effects. Since sample radii were all similar, the radial effects cannot be seen by comparison of these plots. By overlaying all of the VISAR traces, as shown in Figure 4-51, the relative shapes of the curves and reverberations can be compared to those occurring in different materials. The pure epoxy sample traces (represented by the two blue velocity traces) are not the same, but show similar trends, in spite of two different impact velocities. The curves show rapid reverberations in the very early stages of free surface movement, and then only slight reverberations throughout the rest of the rise time. The two green curves (the Ni+nano Al+30% epoxy shots) also show the rapid reverberations very early on, but they continue to show very broad and pronounced reverberations throughout the duration of the rise time. The slopes of these curves are less than in the case of pure epoxy. Finally, the Ni+nano Al+20% epoxy sample free surface velocity (orange) shows movement at a much earlier time, which will be discussed later. Also, the reverberations seen in the trace for sample are even more broad and spaced out.

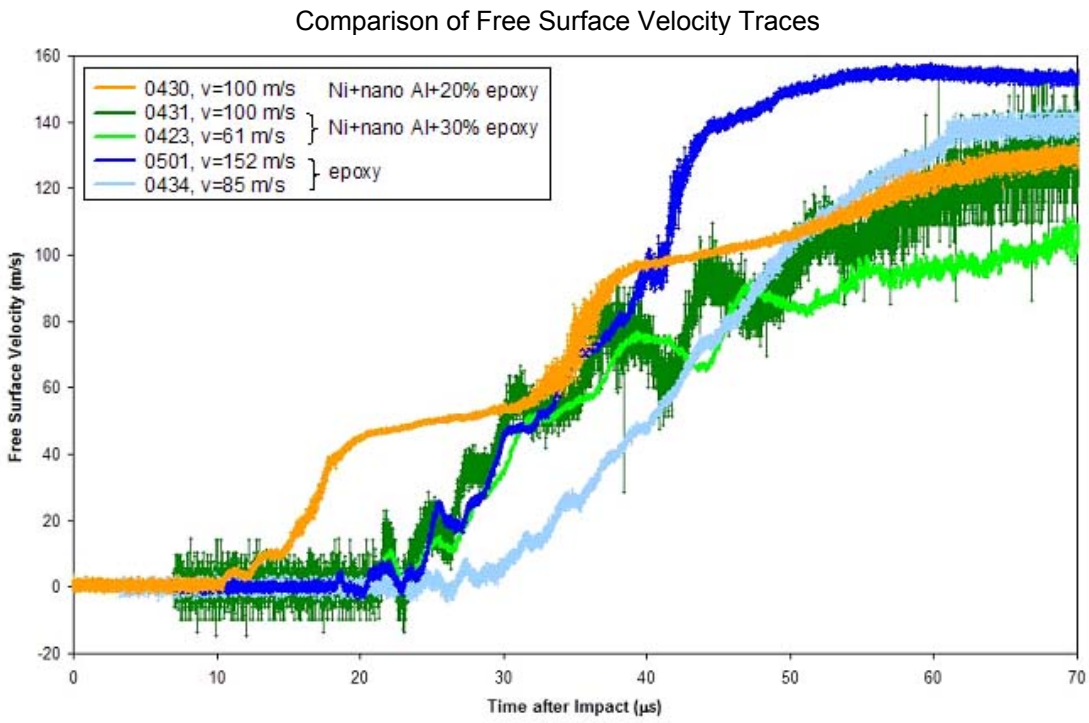

Figure 4-51: Comparison of the slopes and reverberations of VISAR free surface velocity traces.

The VISAR traces provide more information than simply the velocity of the back surface of the sample. The impact time can be determined using the known time of trigger and the standoff distance between the crush pin and the sample face. From the VISAR trace, the time at which the back surface of the sample begins to move can be seen. Using these two pieces of information, the velocity of the elastic wave traveling through the sample can be calculated by dividing the sample length by the time it takes for the back of the sample to start moving. Additionally, the rise time from no movement to maximum free surface velocity can be estimated. This information is summarized in Table 4-11.

Table 4-11: Summary of data derived from VISAR traces for each shot.

Shot	Material	Impact Velocity (m/s)	Time of Movement of Back Surface (μs)	Elastic Wave Speed (m/s)	Rise Time (μs)	Maximum Free Surface Velocity (m/s)	(Free Surface Velocity)/ (Impact Velocity)
0434	Epoxy	84.58	23	2159	38	140	1.66
0501	Epoxy	151.78	18	2794	37	152	1.00
0429	Ni+Al+20% epoxy	88.87	?	?	?	160	1.80
0430	Ni+nano Al+20% epoxy	99.54	10	5002	52	133	1.34
0423	Ni+nano Al+30% epoxy	60.99	22	2580	46	100	1.64
0431	Ni+nano Al+30% epoxy	100.13	22	2116	48	120	1.20

In the case of symmetric impact where both the projectile and the target are of the same material and there is no deformation, the free surface velocity is twice the impact velocity (or particle velocity) [49]:

$$U_p = \frac{1}{2}V ,$$

where U_p = particle velocity and V = impact velocity. In the case of the experiments conducted in the work presented, with a steel flyer impacting a composite sample, the free surface velocity ranges from 1-1.8 times the impact velocity, as illustrated in Figure 4-52. The decrease can be attributed to impedance difference and plastic deformation effects.

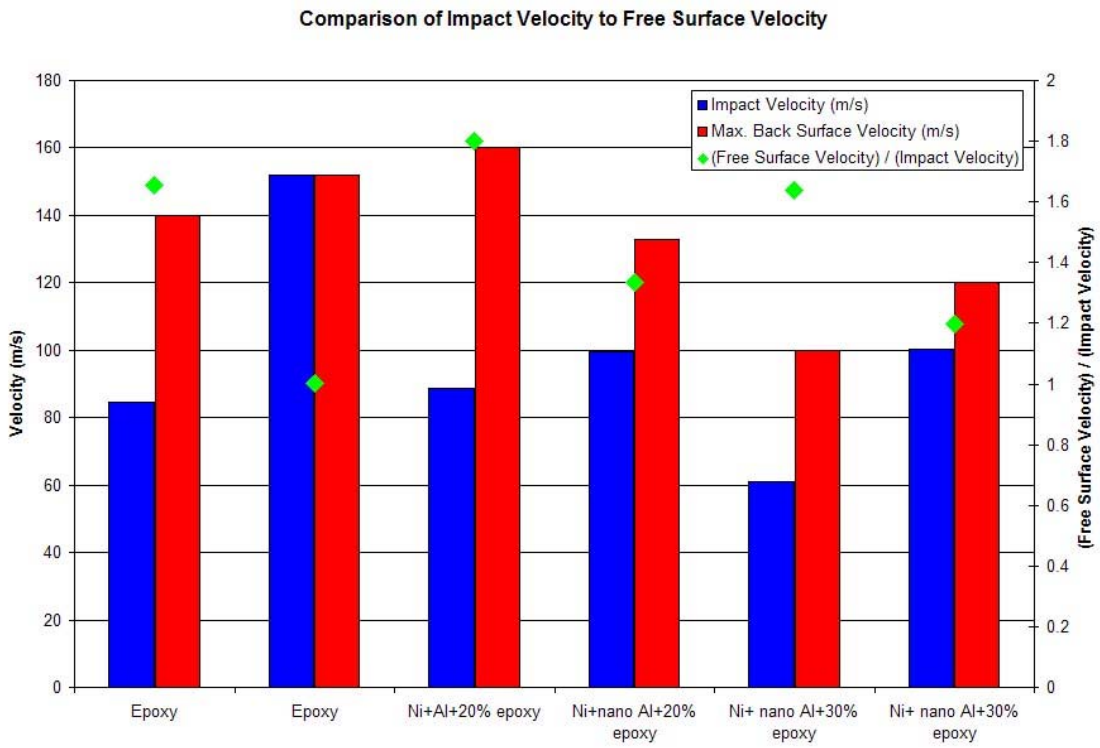

Figure 4-52: Comparison of Impact Velocity to Free Surface Velocity for each reverse anvil Taylor impact test.

The elastic wave speed calculated from the VISAR traces can be compared to the theoretical values of C_l. This comparison is shown in Table 4-12 and plotted in Figure 4-53. Because epoxy is a large volume fraction of all of the materials, it can be seen that by using the Rule of Mixtures, the theoretical values of C_l for materials containing Ni and Al are not much above that of pure epoxy. The elastic wave velocity calculated for epoxy using the VISAR traces showed quite good agreement with the theoretical value, within the standard deviation. However, C_l for Ni+nano Al+20% epoxy was much higher than the theoretical value, and C_l for Ni+nano Al+30% epoxy was much lower than the theoretical value. The Ni+nano Al+20% epoxy value was much higher than any of the measured values due to the fact that this sample started moving 10 μs after impact, while

all other samples did not show movement until around 20 μs. Based on the equations in Section 3.2.3, this increased C_l value is associated with the much higher Elastic Modulus that was measured for this material.

Table 4-12: Theoretical and experimentally measured values of longitudinal elastic wave speed in epoxy-cast materials.

Material	**Theoretical C_l (m/s)**	**Taylor Test C_l (m/s)**
Epoxy	2630	2477 ± 449
Ni+Al+20% epoxy	3512	?
Ni+nano Al+20% epoxy	3512	5002
Ni+nano Al+30% epoxy	3206	2348 ± 328

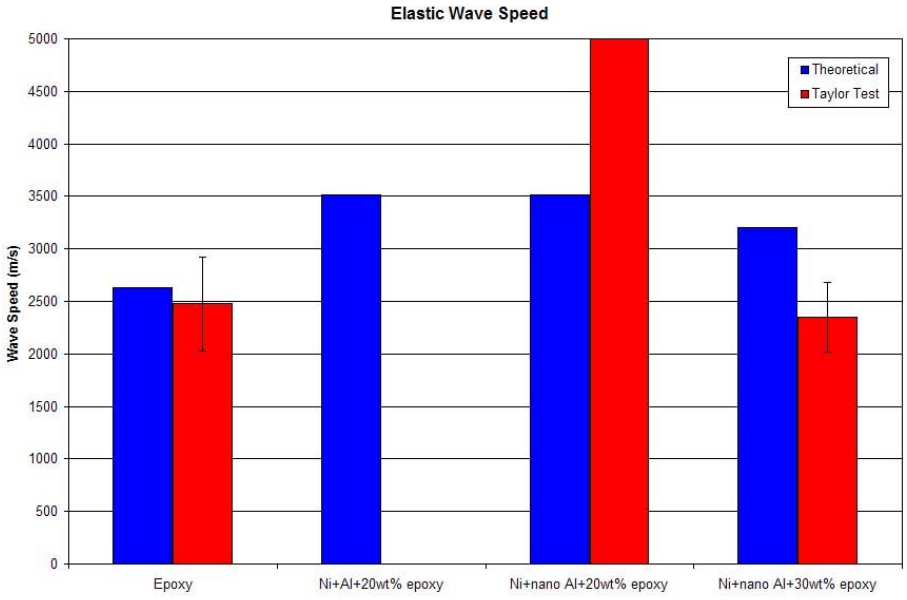

Figure 4-53: Comparison of theoretical longitudinal elastic wave speed to the experimentally measured values from Taylor Tests.

4.3.2.4 Analysis of Recovered Samples

After each reverse-anvil impact experiment, the sample was recovered from the catch tank, if possible. In most cases, large chunks of the sample were found, in addition to some smaller fragments. The pure epoxy sample recovered after shot 0434, shown in Figure 4-54a, showed some deformation due to deformation upon impact in the catch tank, not impact during the actual experiment. The pure epoxy sample from shot 0501 showed a large amount of deformation, which is evident in its recovered sample shown in Figure 4-54b.

The most notable recovered sample was the Ni+Al+20wt% epoxy sample from shot 0429, which is shown in Figure 4-54c. This sample showed a large amount of strain at the impact face, up to 53% before fracture, but the recovered sample was mostly intact. The only part of this sample that had suffered any noticeable deformation was around the edges near the impact face. The fracture was very symmetric and left the sample looking almost conical at the impact face. This fracture pattern suggests that the impact was indeed very planar. This behavior matches with what has been described by Roessig *et al.* [44], who have shown that during impact radial cracks propagate inward from the outward edge, and depending on impact velocity, sometimes a circular crack will form at about half the radius of the cylinder. There was evidence of both of these behaviors in this recovered sample.

The nano Al-containing samples from shots 0430 (Figure 4-54d) and 0431 (Figure 4-54e) showed deformation in the captured images, but the recovered samples did not yield any additional macroscopic information since they fractured more upon impact in the catch tank. In contrast, the nano Al-containing sample from shot 0423 did not

show deformation in the captured images, but was deformed upon recovery due to additional impact in the catch tank, as shown in Figure 4-54f.

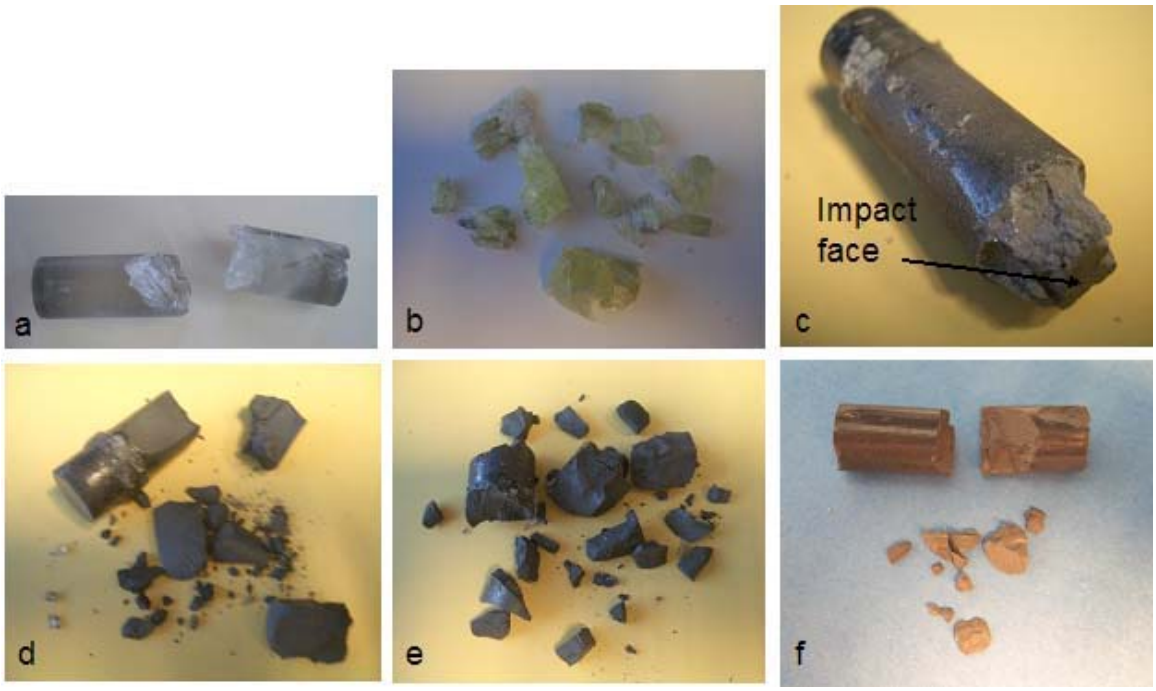

Figure 4-54: Photographs of cast specimens recovered after reverse Taylor impact tests. (a) Pure epoxy sample recovered from Shot 0434 (85 m/s). This sample did not deform when impacted by the projectile; deformation occurred upon additional impact in the catch tank. (b) Pure epoxy sample recovered from shot 0501 (152 m/s). This sample deformed during impact, but fracture took place outside the time frame captured in the images. (c) Ni+Al+20wt% epoxy sample recovered from Shot 0429 (89 m/s). The impact face of this sample shows evidence of good planar impact, as well as evidence of radial cracks propagating inward from the outer edges, or a circular crack forming around half the radius of the cylinder. (d) Ni+nano Al+20wt% epoxy sample recovered from shot 0430 (100 m/s). The sample fractured when impacted by the projectile, and additionally in the catch tank. (e) Ni+nano Al+30wt% epoxy sample recovered from shot 0431 (100 m/s). The sample fractured when impacted by the projectile, and additionally in the catch tank. (f) Ni+nano Al+30wt% epoxy sample recovered from shot 0423 (61 m/s). This sample did not deform when impacted, all damage was caused during impact in the catch tank.

SEM images of the fracture surfaces of samples impacted in the reverse Taylor impact tests were compared with images of the fracture surfaces of compression samples to see if strain rate had an effect on how the materials fractured. The Ni+Al+20% epoxy sample showed features very similar to those seen in the compression sample, as shown in Figure 4-55a. The fracture was glassy, and occurred in the epoxy matrix around the Ni and Al particles. There does not appear to be any fracture of Ni or Al particles. In the case of the recovered Ni+nano Al+20% epoxy sample from shot 0430, shown in Figure 4-55b, the fracture surface is again similar to what was seen in the compression samples. The fracture in this material occurred in the nano Al+epoxy matrix around the Ni particles. There was no evidence of fracture of Ni or Al particles.

The fracture surface of Ni+nano Al+30% epoxy, shown in Figure 4-55c, did show some differences in its fracture surface, which is perhaps an indication that strain rate has an effect on fracture. This material did show some of the familiar fracture in the epoxy matrix around the Ni particles. However, there were also many areas where Ni particles were fractured and their cross-sections could be seen. This was also the case in the fracture surface from Shot 0423, which was the same material.

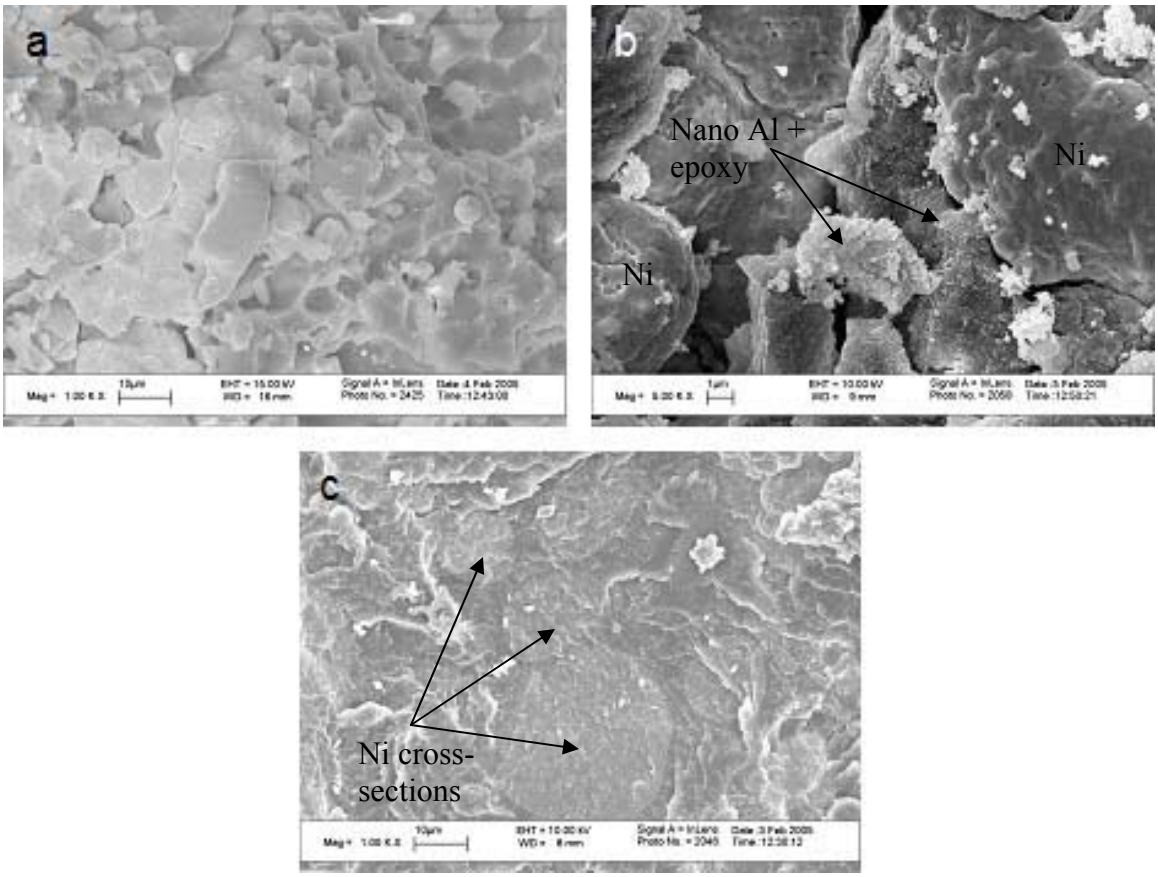

Figure 4-55: SEM images of fracture surfaces of cast specimens recovered after reverse Taylor impact tests. (a) Shot 0429 Ni+Al+20% epoxy Taylor test sample showing glassy fracture in the epoxy matrix and pullout of Ni and Al particles. (b) Shot 0430 Ni+nano Al+20% epoxy Taylor test sample (shot 0430). Fracture occurred in the nano Al+epoxy matrix around the Ni particles. (c) Shot 0431 Ni+nano Al+30% epoxy Taylor test sample showing cross-sections of Ni particles, indicating that fracture occurred through the Ni particles in this sample.

CHAPTER 5

DISCUSSION OF RESULTS

The results of the thermally initiated reaction response and mechanical behavior of Ni+Al+polymer MESMs will be discussed in this chapter, with emphasis on the effects of Al powder particle size, and type and volume fraction of polymeric binder.

5.1 Thermally Initiated Reaction Response of MESMs

Information about the thermally initiated reaction behavior of Ni+Al+polymer MESMs was obtained from DTA and XRD analyses. In particular, the effects of micron-sized versus nano-sized Al, Teflon versus epoxy binder, and different volume fractions of epoxy on reaction behavior were investigated.

From the relative scale of the exothermic reaction peaks observed in DTA traces, it can be concluded that following the melting of Al at ~660 °C there is a stronger and more complete reaction between Ni and micron-sized Al than between Ni and nano-sized Al. This was reinforced by the XRD analysis results that showed presence of unreacted Al in Ni+nano Al samples heated to 800 °C, but no unreacted Al in similarly heated samples of Ni+micron Al. The nano-sized particles have an oxide coating that is quite evidently observed in XRD traces upon heating. It is possible that this coating provides a barrier for thermal initiation of reaction of nano Al, as reported in studies done by Hunt, Aumann and Lebrat [6, 24, 29], which are discussed in Section 2.2.6 of the Literature Review. This would explain the dissimilar reaction response of nano- and micron-sized Al powder in the mixture with micron-sized Ni powder.

When comparing Teflon with epoxy in terms of reaction behavior, Teflon appears to be more reactive with Ni+Al/nano Al. The epoxy-based composites showed no evidence of thermal reaction between epoxy and Ni+Al/nano Al up to 800 °C. In addition, these composites showed reduced reaction between Ni and Al, and no reaction between Ni and nano Al. Microstructural (SEM) characterization of the as-processed materials reveals that interfacial effects may cause the Al particles to break contacts with the Ni particles and become dispersed in the epoxy, which causes the epoxy matrix to act as a barrier for reaction between Ni and Al, with the effects being more severe in the case of nano-sized Al. Teflon-based composites, on the other hand, showed exothermic events indicating reactions of Ni with Al/nano Al as well as reactions of Teflon with Ni+Al/nano Al powders, which were especially prominent in the case of nano-sized Al. XRD analysis also gave indication of formation of NiF_3, NiC_x and possible AlF_3 products when the Teflon-based composites underwent thermally initiated reactions.

5.2 Static and Dynamic Strength Characterization of MESMs

The static and dynamic mechanical properties tests performed in this study yielded interesting results about the strength of the Ni+Al reinforced polymer composites. Due to difficulty in pressing samples, Ni+micron Al+Teflon samples were only tested under static compression conditions tests. These Teflon-containing samples showed very poor strength and a low strain to failure, possibly due to incomplete desification.

The elastic properties of the composites were evaluated through determination of elastic modulus from static compression tests and determination of elastic wave speed using velocity interferometer measurements following reverse Taylor impact tests. Ni+nano Al+20wt% epoxy exhibited an elastic modulus of ~11 GPa, which is almost

four times that of pure epoxy, and is well above that of the other Ni+Al/nano Al composites. Analysis of data obtained using VISAR showed that Ni+nano Al+20wt% epoxy has an elastic wave speed that is much greater than that of any of the other materials (approximately twice that of pure epoxy), and also is ~1500 m/s greater than the calculated expected value.

The stress-strain curves obtained from static compression tests performed on the various epoxy cast-cured samples show different softening/hardening behavior. The pure epoxy and the specimens containing Ni and micron-sized Al exhibited a typical perfectly plastic response. On the other hand, samples with Ni, nano Al and 20 or 30wt% epoxy show strain hardening, which suggests that this effect is not a result of the composition of the reinforcements alone, but the size of the Al particles. One explanation for this behavior is that with micron-sized Ni and Al particles the epoxy matrix absorbs all of the load and dominates the deformation response, with the reinforcement particles having no effect. Since the epoxy alone does not strain harden, the specimens with micron-sized Ni and Al also do not strain harden. In samples with micron-sized Ni and nano-sized Al particles, since nano Al particles detach from the Ni and become blended into epoxy, it is possible that the load is transferred from the nano Al-dispersed epoxy to the Ni particles, and the deformation response of the Ni then dominates the stress-strain behavior, giving rise to strain hardening. However, SEM images of the fracture surfaces of these specimens did not show any deformation of the Ni particles. Hence, the strain hardening behavior observed in the samples with micron-sized Ni and nano Al in 20 or 30wt% epoxy cannot be attributed to the deformation being dominated by the Ni particles. However, it seems possible that the dispersion of nano Al particles in the epoxy is

altering the molecular structure of the epoxy and causing the change in its deformation response that leads to strain hardening. Van Melick et al. [52] found that strain hardening in polymers is proportional to network density, regardless of if the density is caused by chemical cross-links or physical entanglements. The dispersion of the Al particles throughout the epoxy matrix can provide physical entanglements since nanoparticle/matrix interactions lead to a loss in mobility of the chain segments [53]. Nano particles have a very large surface area, and due to the increased contacts between the epoxy and nano particles, the cohesive strength of the epoxy increases and leads to a higher mechanical strength of the interfaces [54]. This is partially due to the mechanical interlocking resulting from the extensive contact between the epoxy and the filler particles [54, 55]. There is evidence in the literature indicating that nano-sized particles have different effects on mechanical properties than micron-sized particles, and the increased strength strain hardening seen in this study seems likely to be caused by the entanglements and interlocking caused by the dispersion of nano Al particles in the epoxy matrix. While this explanation appears logical and consistent with findings in literature, further evidence needs to be obtained prior to conclusive determination of the role of nano Al on the strain hardening response of epoxy. The observed results also provide the rationale for further exploiting this effect to alter the mechanical behavior of epoxies via use of nano-sized particles by influencing their mechanical structure.

Both the static compression tests and the reverse Taylor anvil-on-rod impact tests showed that pure epoxy behaves in a ductile manner relative to the powder-reinforced composites. The addition of Ni and Al powders causes an increase in brittle behavior due to the presence of interfaces where failure can occur. Ni+nano Al+20wt% epoxy showed

the best mechanical properties under both static and dynamic loading conditions, which can be seen by the compressive strength and strain to failure values reported in Table 5-1 and illustrated in the bar graph in Figure 5-1. The dynamic yield strengths listed in Table 5-1 were obtained from the reverse anvil Taylor impact testing in conjunction with Wilkins' analysis (Equations 2-1 through 2-5). For each material, Wilkins' analysis was performed using the last captured image frame in which the back surface of the sample could still be seen for use in measuring a final length. Error bars in the dynamic yield strength calculations are derived from the error in measurement of the various factors contributing to σ_{ys}, e.g., density, impact velocity, and initial and final length, which have inherent measurement error related to the pixel resolution of images captured during Taylor tests.

Table 5-1: Static and dynamic compressive yield strengths, and dynamic strain to failure, for epoxy cast materials.

Material	**Static σ_{ys} (MPa)**	**Dynamic σ_{ys} (MPa)**	**Dynamic Strain to Failure**
Epoxy	99.96 ± 4.11	111.7 +16.6/-13.5	0.677
Ni+Al+20% epoxy	103.80 ± 12.15	124.9 +56.9/-41.1	0.530
Ni+nano Al+20% epoxy	156.80 ± 4.44	236.1 +122.8/-85.9	0.547
Ni+nano Al+30% epoxy	130.20 ± 19.24	214.2 +53.0/-34.8	0.505

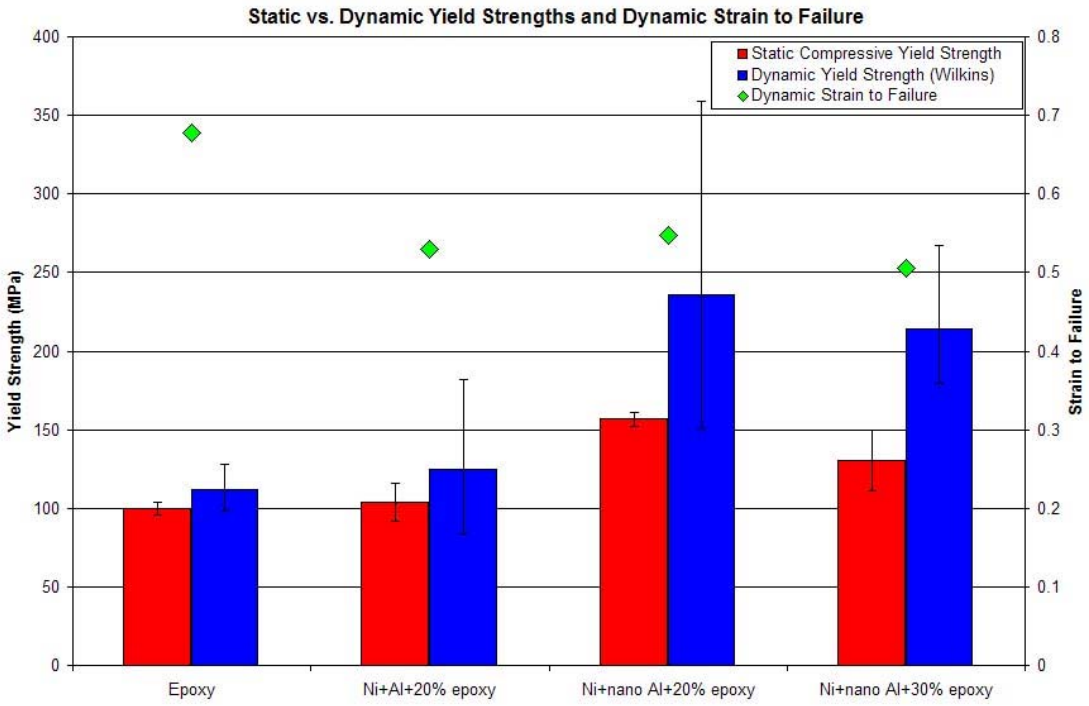

Figure 5-1: Comparison of static compressive yield strengths obtained from compression tests with dynamic yield strengths obtained from reverse anvil Taylor impact tests and Wilkins' analysis. The graph also includes dynamic strain to failure, which was also reported in Figure 4-44.

It can be seen from Figure 5-1 that the addition of Ni+Al powder mixtures to epoxy increases both the static and dynamic compressive strengths. The use of micron-sized Al (in the Ni+Al+20wt% epoxy sample) shows only a marginal strength increase over that of epoxy. On the other hand, Ni+nano Al+20wt% epoxy exhibited a compressive yield strength of ~156 MPa, which is ~157% that of pure epoxy. In the case of dynamic mechanical properties, Ni+nano Al+20wt% epoxy exhibited a yield strength of ~236 MPa, which is slightly more than double the dynamic compressive yield strength of pure epoxy, and likewise, nearly twice that of Ni+Al+20wt% epoxy, which differed

only by Al particle size. Further increase in epoxy content from 20 to 30wt% (55.7 to 68.3 vol%), however, resulted in some decrease in strength as compared to Ni+nano Al+20wt% epoxy, but the strength values were still far above those of pure epoxy and Ni+micron Al+20wt% epoxy. These results suggest significant strengthening of the epoxy matrix by the addition of nano-sized Al powders. As mentioned in the previous section, the nano Al particles seem to detach from the Ni and become dispersed in the epoxy, thereby providing an ideal reinforcement for the composite.

The dynamic yield strength values that were obtained are based on an average and do not incorporate parameters such as strain rate. Fore these reasons, it is not accurate to report a single dynamic yield strength value for a material, but it should be recognized that there is a conceptual dynamic yield strength that exceeds the static yield strength for a material. Additionally, the Wilkins' analysis was performed on the last usable image, which was not necessarily taken after deformation was complete. In order to compensate for these factors, the analysis was applied to all frames after impact in which the back surface of the samples could be seen, and the dynamic yield strength value during each stage of the deformation was plotted versus the ratio of final to initial length. This plot, which is shown in Figure 5-2, shows a trend in that the dynamic yield strength values for all of the materials fall on the same curve. It appears that as deformation continues the dynamic yield strength levels off and approaches some value, which most likely varies depending on the material. Since strain rate decreases as deformation continues, the Wilkins equation suggests that dynamic yield strength decreases proportionally to strain rate. This further suggests that the dynamic yield strength should approach the static

yield strength since strain rate approaches zero, but the Wilkins equation won't describe this correctly.

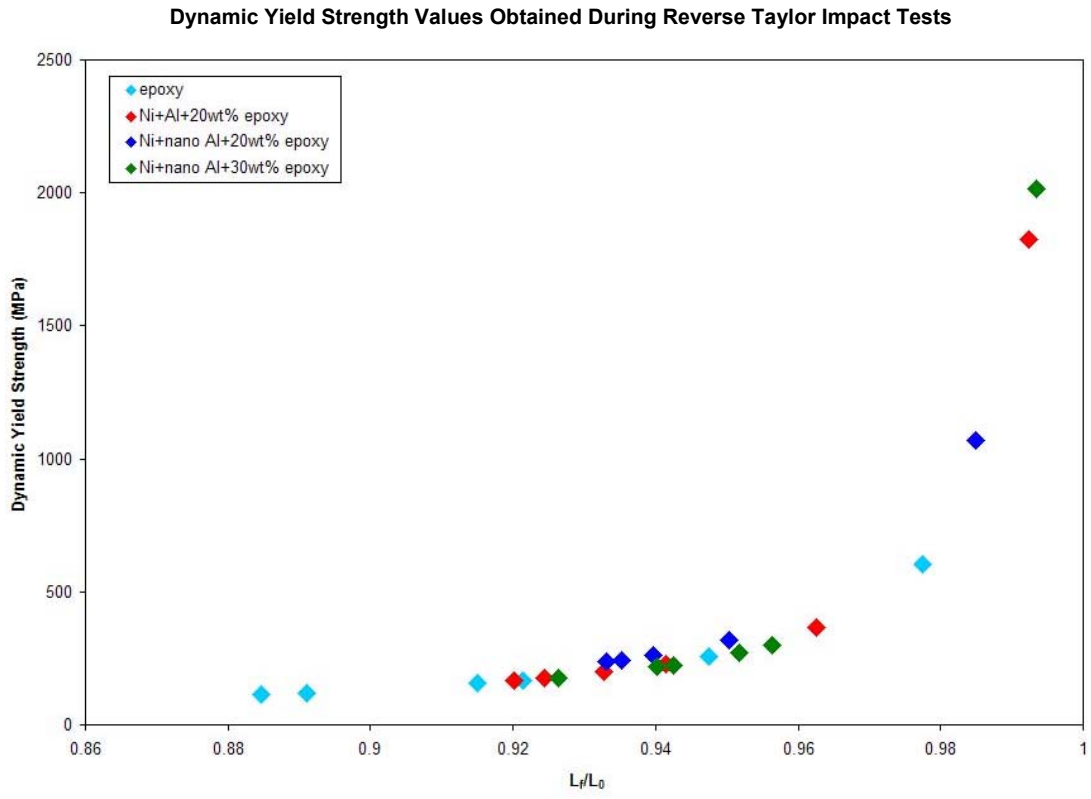

Figure 5-2: Plot of dynamic yield strength vs. L_f/L_0, which shows that the dynamic yield strengths during deformation of all cast materials lie on the same curve. The right side of the plot corresponds to values of L_f/L_0 close to 1, indicating little change in length due to deformation; these values are correspond to early stages of deformation. In contrast, the left side of the plot corresponds to more change in length and later stages in deformation.

Figure 5-3 takes a closer look at the dynamic yield strength values obtained during later stages of deformation. It can be seen that the values for the pure epoxy, Ni+Al+20% epoxy, and Ni+nano Al+30wt% epoxy samples all fall on the same curve. However, the values corresponding to the Ni+nano Al+20wt% epoxy do not fall on this same curve when examined closely. This sample demonstrates a higher dynamic yield

strength than any other cast material when deformed to the same percent of its original length. Although more work needs to be done to confirm this trend, these results indicate that Ni+nano Al+20wt% epoxy exhibits dynamic mechanical behavior that is superior to that of the other materials examined. Figure 5-3 also shows the static yield strength values (indicated as dotted lines) obtained from compression testing. The dynamic yield strength values for each material seem to be approaching a value that is $\geq$ to the corresponding static yield strength value. Also, the three materials with dynamic yield strengths which fall on the same curve also have static yield strengths which are not very different from each other (with the exception of Ni+nano Al+30wt% epoxy, which has a static yield strength ~30 MPa higher than the other two materials). The fact that the static yield strengths are similar would explain why these materials lie on the same curve and appear to be approaching similar values, while the Ni+nano Al+20wt% epoxy lies on a separate curve which approaches its higher static yield strength.

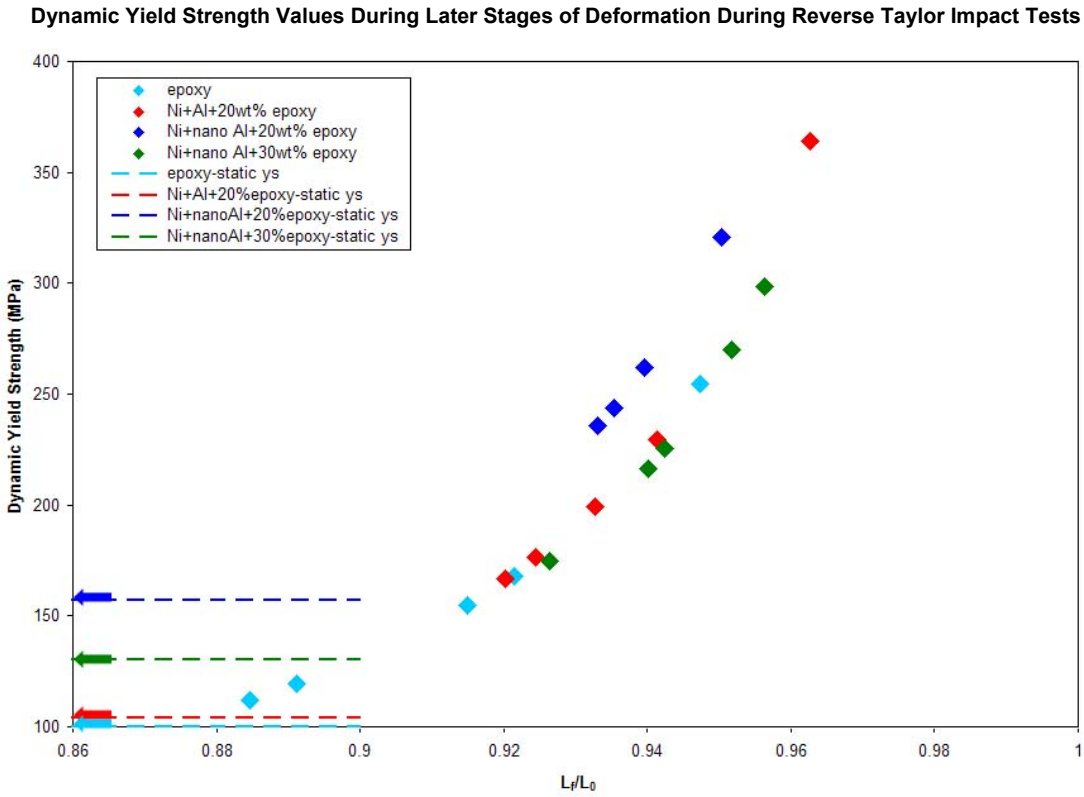

Figure 5-3: A closer view of the dynamic yield strength values from the later stages in deformation presented in Figure 5-2. The plot shows that Ni+nano Al+20wt% epoxy has a higher dynamic yield strength than the other cast materials at any given percent decrease in length. Static yield strength values are also presented on this plot for comparison.

A plot of L_f/L_0 vs. $\rho U^2/2\sigma$, which is shown in Figure 5-4, shows the scaling law used by Wilkins. This plot shows that the data for all types of material lie on the same curve, which is evidence that this scaling law is valid for all of these materials. Additionally, this plot shows that all of the materials are behaving in a similar manner.

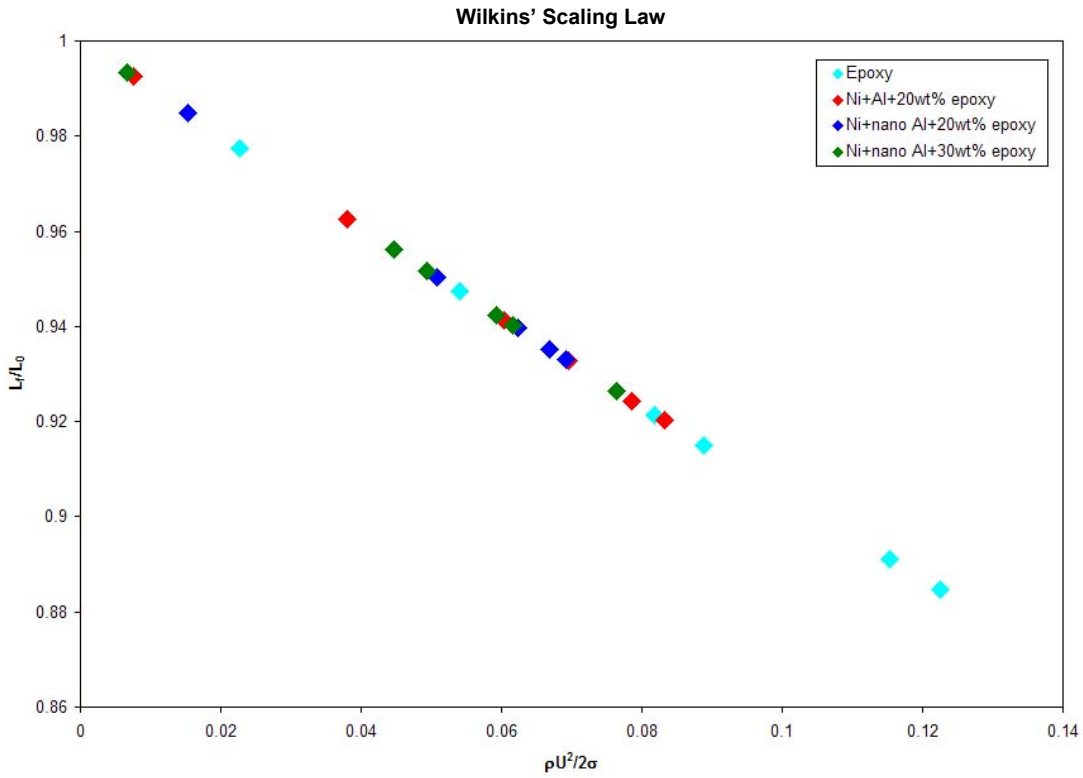

Figure 5-4: Plot showing the scaling law used by Wilkins to determine dynamic yield strength.

SEM analysis of the fracture surfaces showed glassy fracture in the epoxy matrix and pullout of the Ni and Al particles. The Ni+nano Al+30wt% epoxy samples tested under dynamic loading (reverse anvil Taylor impact tests) showed evidence of fracture through the Ni particles, in addition to the particle pullout which was observed under static loading. It is possible that increasing epoxy content increases the strain-rate sensitivity of the Ni+Al+epoxy composites, but more testing on samples with greater variation in epoxy content would be needed to conclusively determine the strain-rate effect.

5.3 Ni+Al+Polymer Composite as a Potential MESM

While none of the Ni+Al+polymer composites fabricated in this study possessed both high strength and reactivity, possibilities still remain for development of a MESM using the materials currently under analysis. There seems to be a few possible ways to use the materials under investigation to produce a material that provides both structural and energetic functions.

The Ni+nano Al+20wt% epoxy sample exhibited the best strength and mechanical properties out of all of the composites investigated; this was believed to be due to the reinforcement of the epoxy matrix by the nano-sized Al particles. However, this same material showed no thermally initiated reactions between Ni and nano Al, or between epoxy and the metallic powders. These results indicate a tradeoff between strength and reactivity, but that may not always be the case. Since the nano Al seemed to be separated from the Ni particles and became engulfed by the epoxy matrix, which prevented reaction, one potential solution would be the use of nano-sized Ni particles in conjunction with nano-sized Al. Since the interfacial properties of nano Ni are much different than those of micron-sized Ni, use of nano Al would allow for clustering of nano Ni with nano Al within the epoxy matrix, so that reaction between Ni and Al can still proceed. More nano-sized reinforcements, in the form of nano Ni powder, would be likely to further increase the strength seen in the case when only nano Al particles were included in the composites.

Another possibility for a MESM would be to take advantage of the reactivity seen when the all powders were of the micron scale. Ni+Al+20wt% epoxy samples showed reactivity between Ni and Al, but these samples were only marginally stronger than pure

epoxy. To increase the strength, a nano-sized reinforcement such as carbon fibers or carbon nanotubes could be introduced into the epoxy matrix. Ni+Al+nano reinforcements+epoxy could potentially exhibit both strength and reactivity.

It should also be noted that only thermally initiated reactions were considered in the evaluation of reactivity, with a heating rate of 10 °C/min. Although epoxy did not show any reactivity with the metallic powders under these conditions, there is potential for reaction under high pressure shock conditions. Under these conditions, mechanical disturbances would be prevalent, causing shear and rubbing amongst metallic constituents, and the rate of heat input would be more rapid. Will these conditions lead to shock-induced chemical reactions involving epoxy? Will the oxide layer around the nano Al particles be mechanically removed during impact, causing nano Al to be more reactive under these conditions? It is important to stress that only one specific reaction scenario was investigated in the present work. Other possibilities for initiation of reactions between the reactive metal constituents and polymer matrix remain to be explored.

Although Teflon-based samples were not able to be mechanically characterized, these materials were shown to be highly reactive in the thermal conditions examined. Teflon has also been shown to be reactive in many previous studies [30-32]. Since Teflon reacts with the metallic powders, in addition to allowing reaction between Ni and Al, the reactivity of this system should be exploited. In order to introduce some strength into this system, compacts of nano-sized Ni, Al and Teflon powders need to be fabricated to much higher densities than were achieved in this study. Use of all nano-scale powders may help the compacts to densify more fully to avoid interparticle friction effects between particles of different sizes and hardnesses. Additional nano-sized

reinforcements may also be used for further increase in strength. Once better Teflon-containing compacts are obtained, static and dynamic compression testing of these samples can give an indication of the strength and reaction response of this materials system.

It is clear that further work is necessary in order to design a MESM based on the Ni-Al system, but the work performed in this thesis has provided a basis for development of candidate multifunctional materials.

CHAPTER 6

CONCLUDING REMARKS AND RECOMMENDATIONS

Following is a summary of results and conclusions obtained from this study, as well as recommendations for future work.

6.1 Summary and Conclusions

Materials consisting of Ni and Al and a Teflon or epoxy polymer binder have been fabricated by pressing or casting. The particle size of Al was varied (~56.3 nm vs. <45 μm), as well as binder content (20-30 wt% epoxy and 10vol% Teflon). Samples containing epoxy binder were cast into rods of 0.6" diameter and 6" length, whereas samples containing Teflon binder were pressed to a maximum size of 0.25" diameter and 1" length. Powder pressing with Teflon binder did not result in samples of a size usable for any mechanical characterization due to difficulty with the die. Additionally, materials containing nano-Al would not densify into rods during pressing.

SEM characterization of fabricated materials revealed a uniform distribution of particles in the polymer matrices. Density measurements showed that cast materials achieved much lower pore content (0-6%) than pressed materials (6.3-14.1% without binder and 8.7-19.8% with binder), although the overall density of the cast materials was lower due to the large epoxy fraction. Also, materials containing nano Al were less dense than those containing micro-Al due to less efficient packing and a higher volume fraction of smaller pores.

The reactive properties of these materials were evaluated using differential thermal analysis coupled with x-ray diffraction. These analyses showed evidence of

thermally initiated reactions between Ni and Al, as well as Ni+Al and the polymer binder. NiAl was the main reaction product formed near the melting point of Al. Nano-sized Al powder showed a preference for reaction with the polymer binder over Ni, while micro-Al reacted strongly with Ni regardless of the presence of a binder. Pressed materials showed an additional reaction between Ni and leading to formation of Ni_2Al_3 that was not seen in cast materials or powder mixtures. DTA showed reactions between Al and Teflon, which couldn't be confirmed by XRD due to overlapping peaks. XRD did, however, show evidence of Ni reacting with polymer binders. These materials proved to be highly reactive with many different factors including processing and particle size that can be controlled to alter reaction products and initiation characteristics.

The structural behavior of these materials was evaluated using static compression tests and dynamic reverse anvil Taylor impact tests in a gas gun with high-speed digital photography and velocity interferometry measurements. Compression tests revealed that pressed samples containing Teflon were lacking in strength when compared to the cast samples. The material with the lowest epoxy content and nano-sized Al powder showed the most superior strength with an elastic modulus of ~11.4 GPa, a static compressive yield strength of ~156 MPa and a dynamic compressive yield strength of ~236 MPa. Dynamic mechanical testing using Taylor tests gave qualitative information about deformation from the high-speed digital photography images. Addition of Ni and Al powders to the epoxy matrix increased the brittle behavior of the material. Of the reinforced polymer composites, the material containing nano Al and 20wt% epoxy again showed the most superior mechanical behavior in that it endured the most strain (~53%) before fracture; this is in comparison to >67% strain seen in the pure epoxy sample.

VISAR measurements revealed free surface velocities between 1 and 1.8 times the impact velocity.

SEM examination of the fracture surfaces of the cast materials revealed pullout of Ni and Al particles, and glassy fracture in the epoxy matrix. This applied to cast materials after fabrication, and samples recovered from compression tests and Taylor tests. The material containing the 30wt% epoxy showed fracture through the Ni particles in the post-Taylor test sample, but not in the compression samples, indicating possible effects of strain rate on fracture mechanism.

6.2 Recommendations for Future Work

While this has been the first study aimed at investigating the reaction and structural behavior of Ni+Al+polymer reinforced composites, it has provided valuable information that warrants further study. The effect of particle size was explored in this study using both micro and nano-sized Al. The effect of the particle size of Ni also needs to be explored.

In terms of processing, the casting/curing process should be optimized in order to fabricate samples with even lower epoxy content. Although samples used in this study contained only 20% epoxy by weight, they still contained more than 50% epoxy by volume. Minimizing epoxy content allows for more Ni and Al, and thus the strength properties of Ni and Al. Another technique that could be utilized to increase strength in these materials would be addition of carbon fiber or carbon nanotubes as reinforcements. However, these would be expected to lower the reactivity.

It would also be desirable to obtain pressed samples of Ni+Al+Teflon of dimensions desirable for Taylor tests. The die used in this study did not permit pressing

of samples of 2” length due to difficulty in overcoming the surface tension of the pressed sample with the die wall during release of the sample from the die. Use of a press that can achieve higher pressure would also be helpful in attaining more dense samples that would provide more strength than exhibited by the samples fabricated in this study. If better quality Teflon-containing samples could be fabricated, the static and dynamic mechanical properties of these materials could be evaluated, since these provide a more attractive reactive response.

Charpy impact testing of these materials would be useful in evaluating the toughness of the various materials, and relating toughness to variations in particle size and binder content. Toughness values and energy absorption characteristics could be correlated to dynamic mechanical behavior observed in Taylor impact tests.

The Taylor impact tests performed in this study were conducted at impact velocities near 100 m/s. It would be desirable to test all of the materials at multiple impact velocities ranging up to 500-600 m/s. This would allow for comparison of dynamic mechanical behavior at different impact velocities and give insight into the behavior of these materials at a wide range of strains and strain rates.

The Hasan-Boyce Model [56, 57] has commonly been used as a strength model for thermoset polymers, including epoxy. It is therefore believed that this would be an appropriate strength model for the Ni+Al+epoxy systems since they are largely epoxy-based. It would be quite useful to see how these materials would behave using this model, in comparison to how they actually deformed in reverse Taylor tests. This comparison, as well as a comparison of free surface velocity profiles and plots obtained from the House analysis, can be made using AUTDOYN 2-D simulations. However, the

user-defined strength equation for the Hasan-Boyce Model would first have to be implemented into the AUTODYN library using Fortran coding. Completion of this task would aid greatly in the modeling of reinforced polymer composites, as well as many other polymer-based systems.

Quantitative characterization of the microstructures fabricated in this study would be helpful in the modeling task associated with this project. Obtaining statistical data about the particle size distribution, nearest neighbor distribution and clustering would provide the basis for modeling mechanical and reactive behavior of these materials.

The reactivity of the Ni+Al+epoxy systems was studied only under thermal conditions. The study should be extended to investigate pressure initiation of reaction. Plate impact experiments with PVDF stress gauges can be employed to deduce the equation of state and infer stress initiated reaction response. These experiments will also give insight to the dynamic high-pressure behavior, phase stability, energy release characteristics and shock-induced chemical reactions leading to high-pressure phase formation in the Ni-Al-epoxy system, in addition to providing a comparison between shock-induced chemical reactions and thermally initiated reactions observed in DTA.

APPENDIX

A.1 XRD Traces

A.1.1 XRD of Ni+Al/nano Al Materials

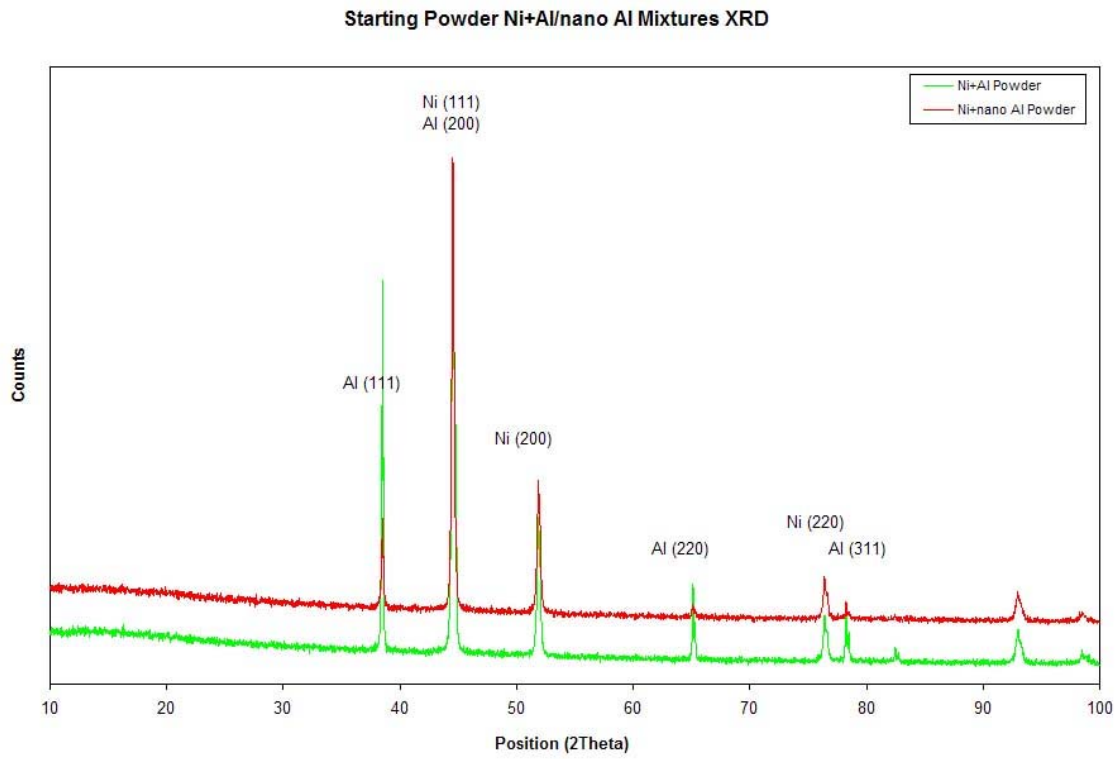

Figure A-1: XRD of mixtures of commercially purchased Ni+Al/nano Al powders.

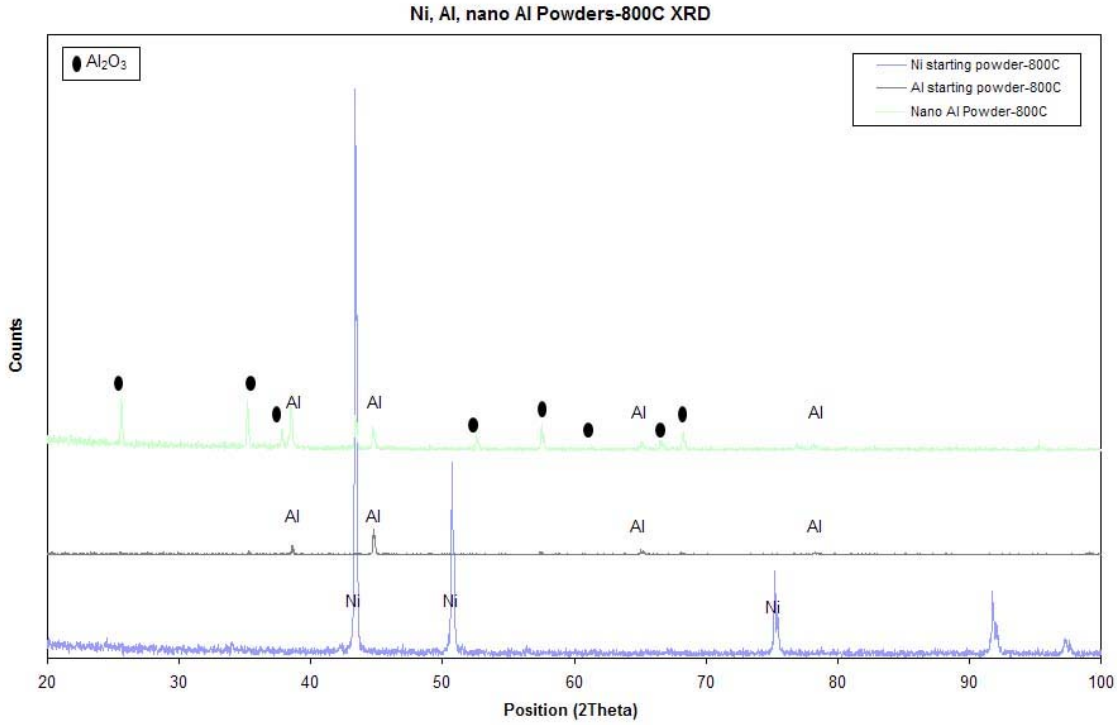

Figure A-2: XRD of Ni, Al, nano Al powders heated to 800 °C to exceed the reaction exotherm corresponding to the melting of Al.

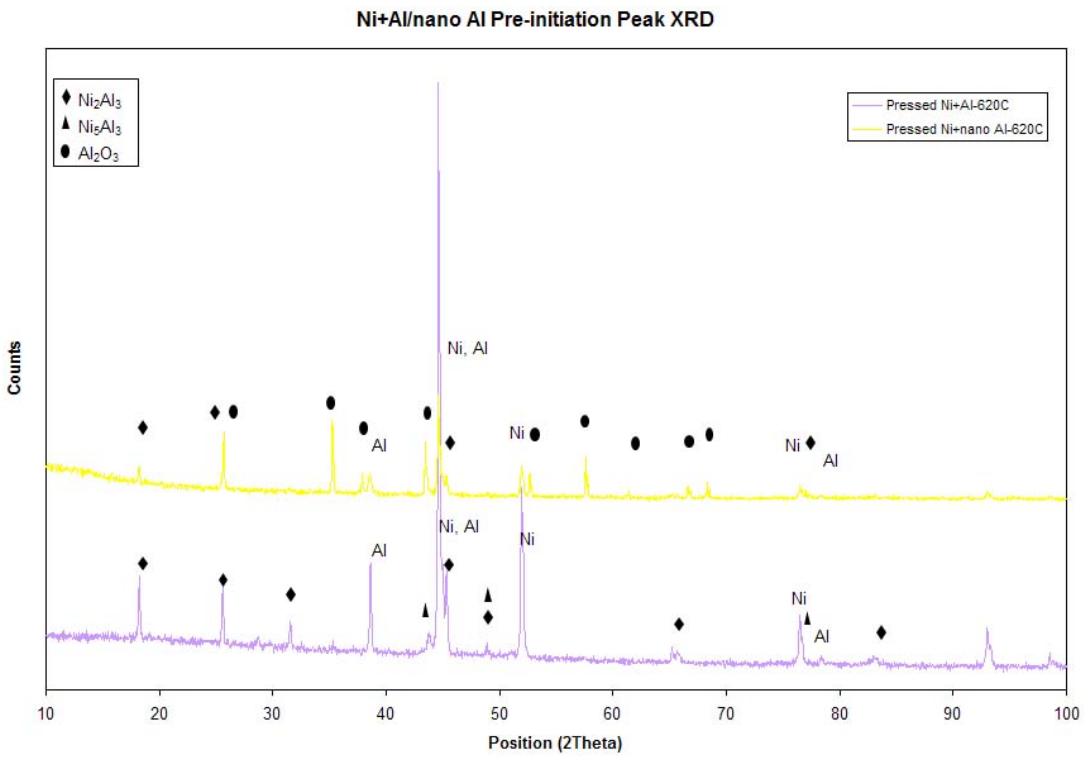

Figure A-3: XRD of mixtures of Ni+Al/nano Al powders that showed a pre-initiaiton reaction exotherm.

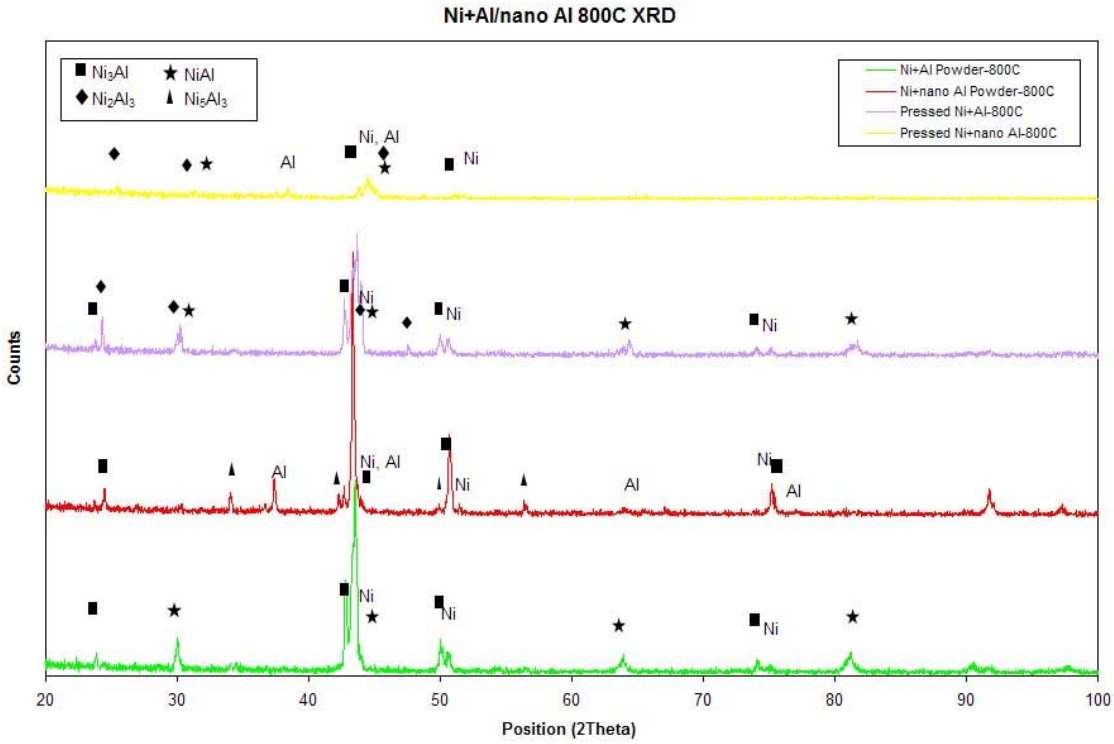

Figure A-4: XRD of mixtures of Ni+Al/nano Al powders after heating to a temperature past exceeding the reaction exotherm corresponding to $T_{m,Al}$.

A.1.2 XRD of Epoxy-Cast Materials

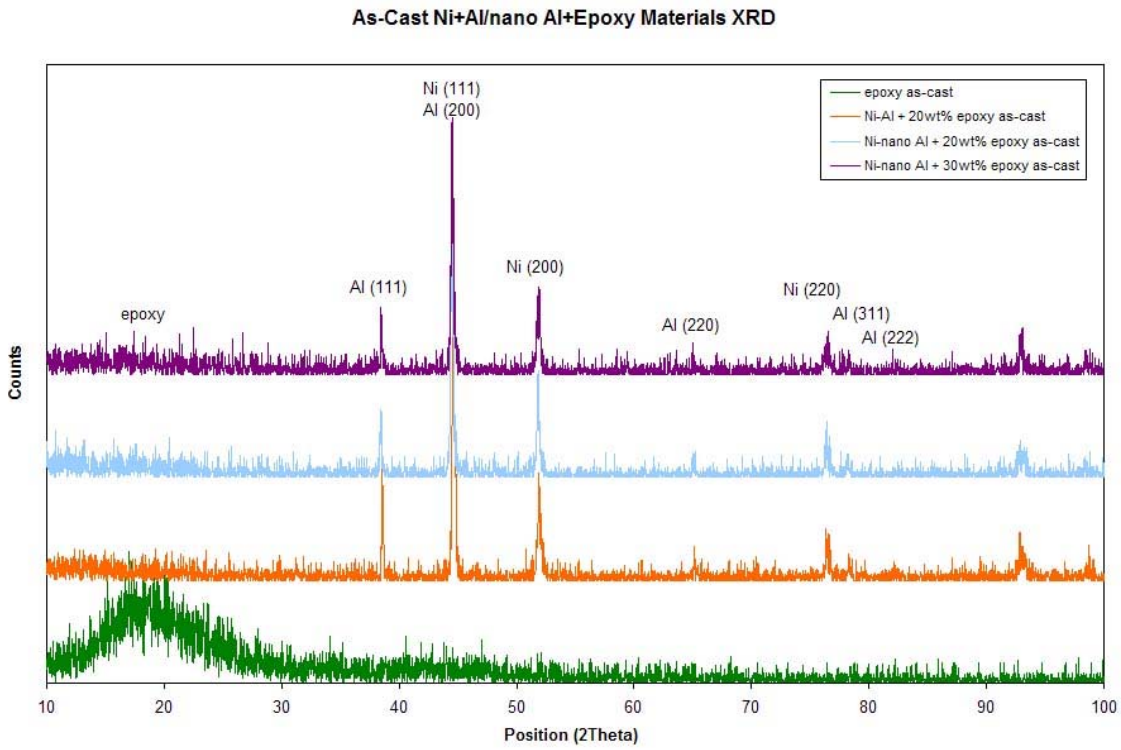

Figure A-5: XRD of epoxy-cast materials in the as-fabricated state.

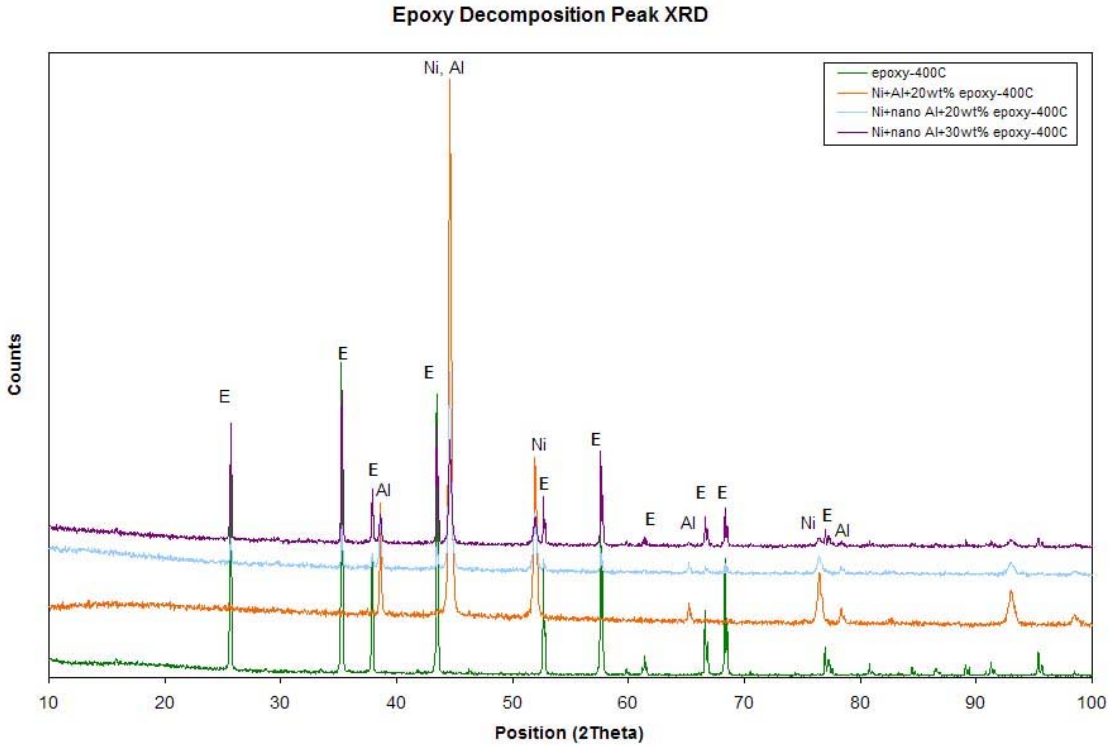

Figure A-6: XRD of epoxy-cast materials after heating past epoxy's decomposition exotherm.

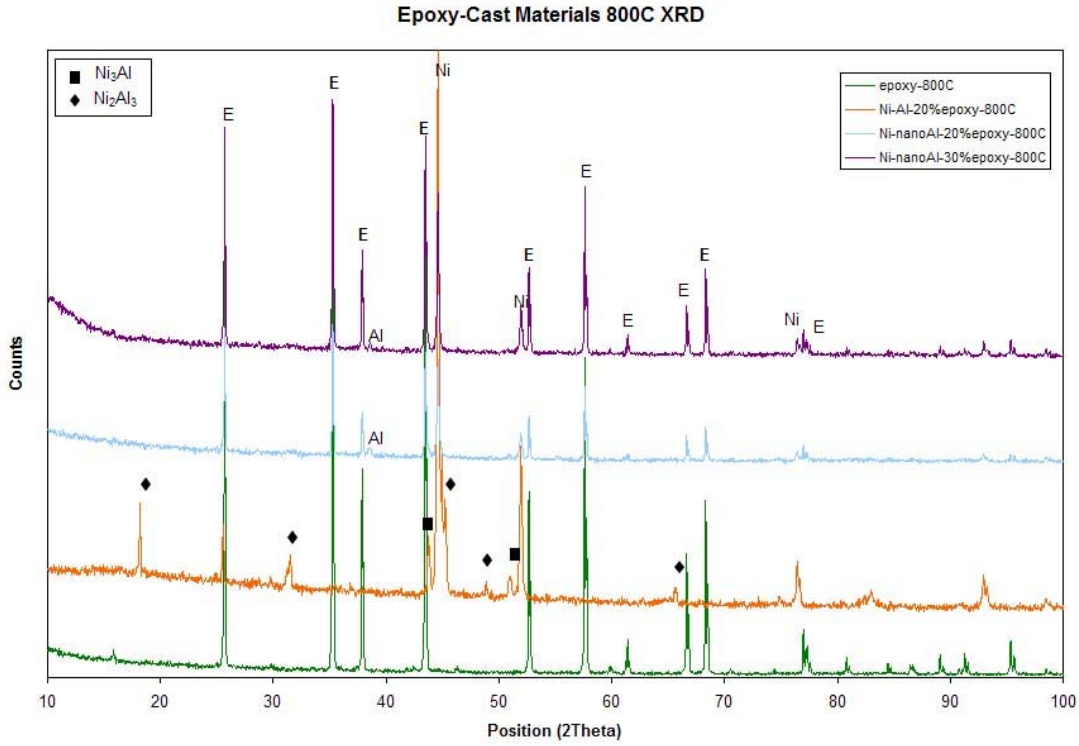

Figure A-7: XRD of epoxy-cast materials after heating past the reaction exotherm corresponding to $T_{m,Al}$.

A.1.3 XRD Teflon-Containing Materials

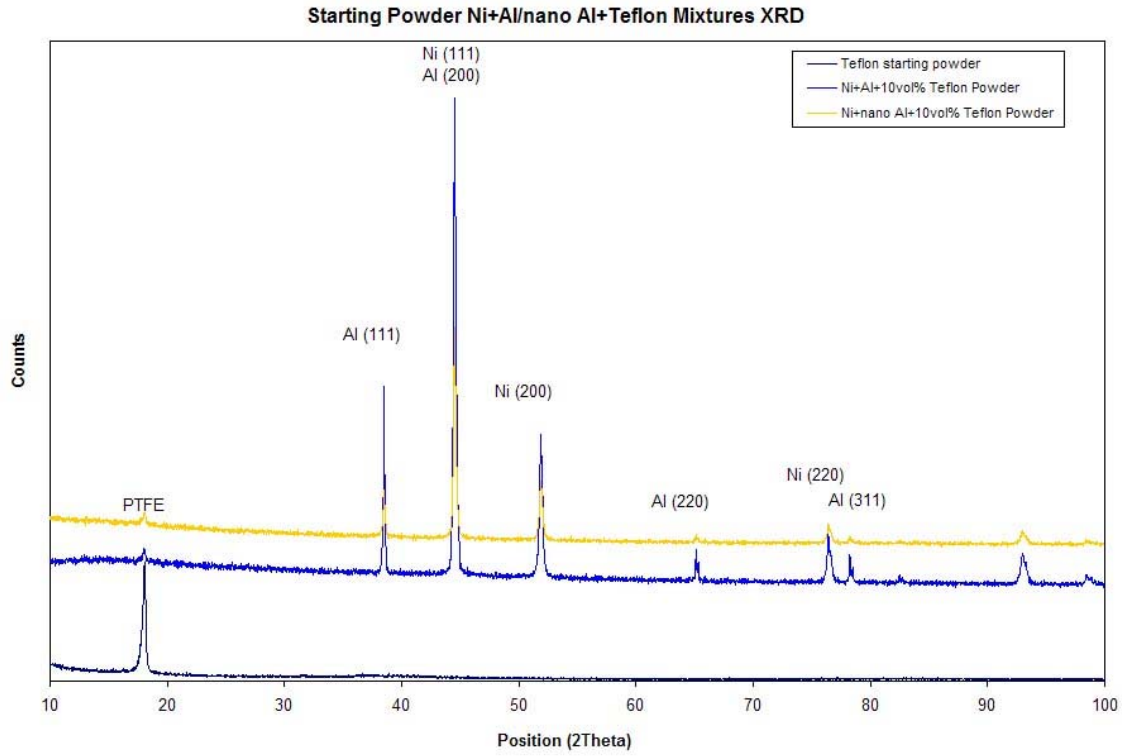

Figure A-8: XRD of mixtures of commercially purchased Ni+Al/nano Al +Teflon powders.

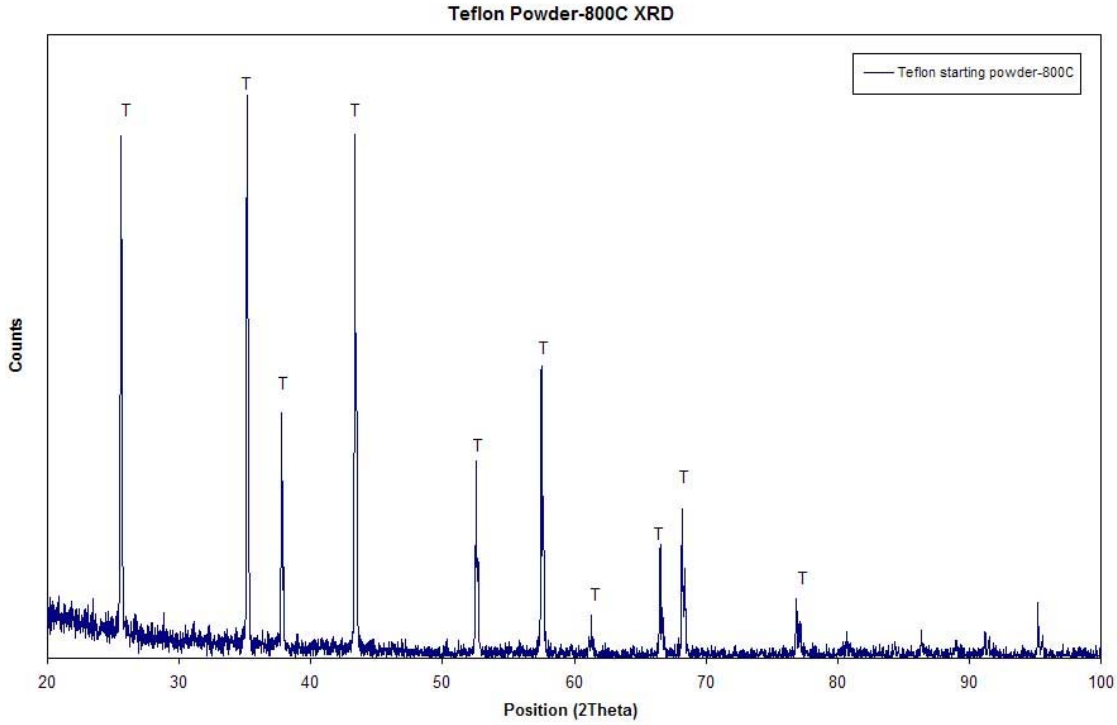

Figure A-9: XRD of Teflon after heating to 800 °C.

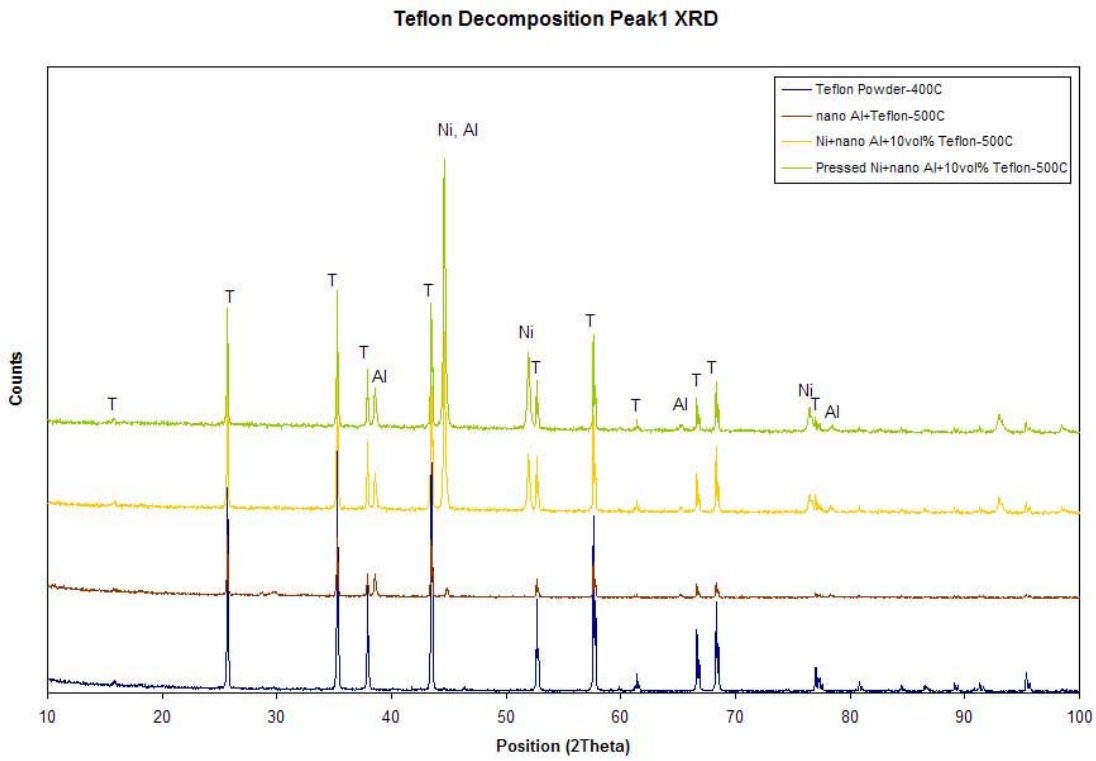

Figure A-10: XRD of materials showing a reaction exotherm at a temperature near Teflon's first decomposition peak.

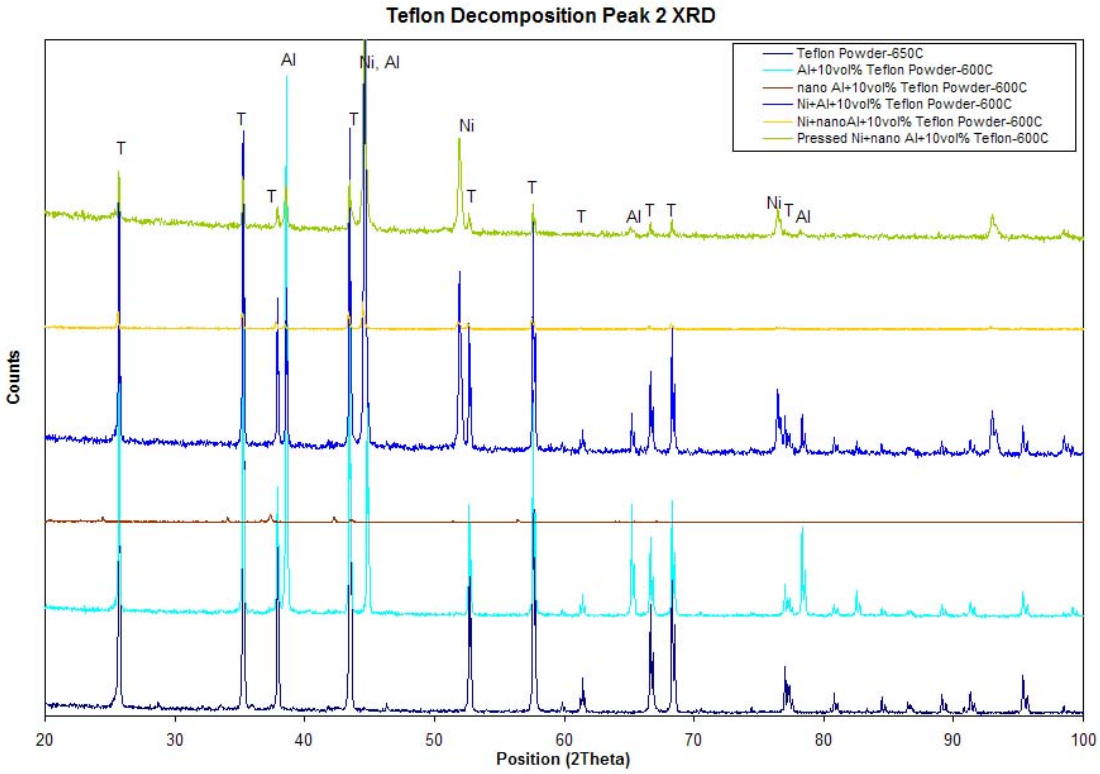

Figure A-11: XRD of materials showing a reaction exotherm at a temperature near Teflon's second decomposition peak.

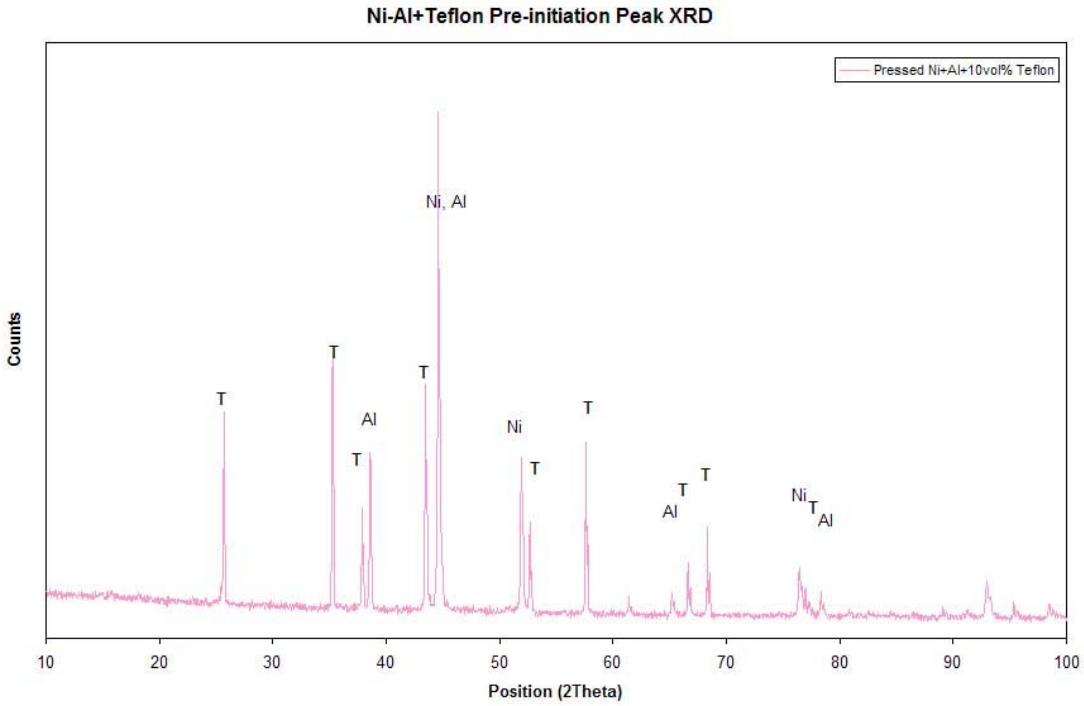

Figure A-12: XRD of Teflon-containing materials showing a pre-initiation reaction exotherm.

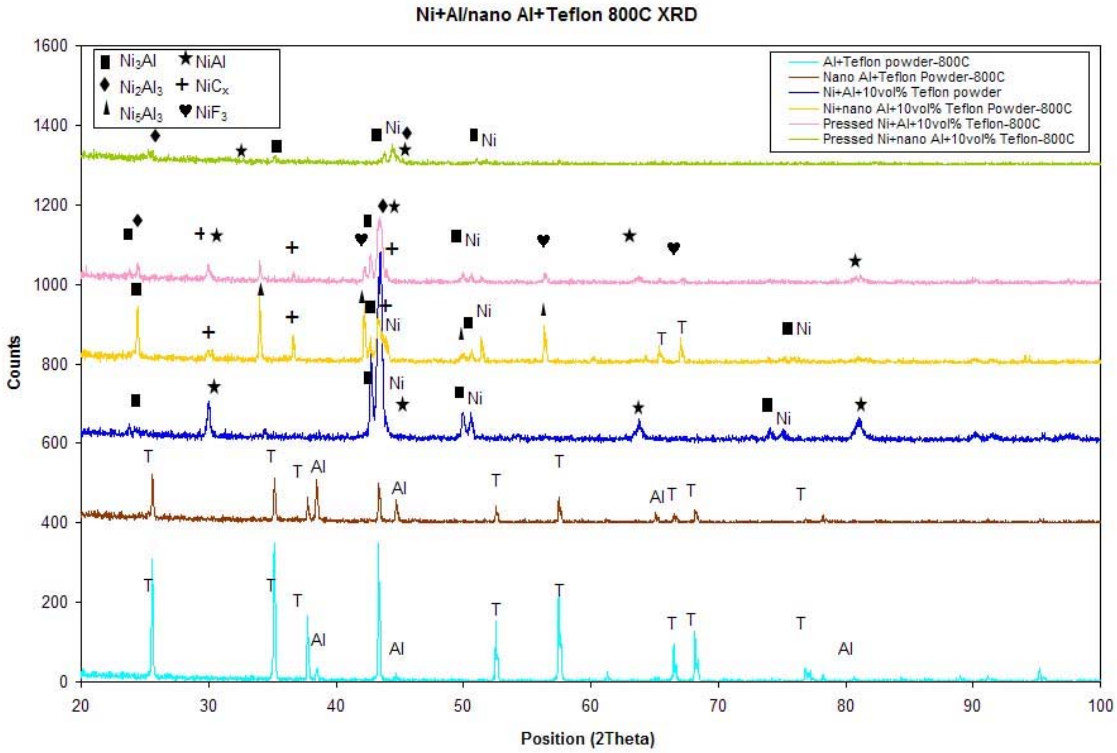

Figure A-13: XRD of Teflon-containing materials after heating to a temperature exceeding the reaction exotherm corresponding to $T_{m,Al}$.

REFERENCES

1. Thadhani, N.N., et al., *Shock-induced reaction synthesis (SRS) of nickel aluminides.* Journal of Materials Research, 1992. **7**(5): p. 1063.

2. Thadhani, N.N., *Shock-induced chemical reactions and synthesis of materials.* Progress in Materials Science, 1993. **37**: p. 117-126.

3. Horie, Y., Graham, R. A., Simonsen, I. K., *Observations on the shock synthesis of intermetallic compounds*. Metallurgical Applications of Shock-Wave and High Strain Rate Phenomena. 1986. 1023-1035.

4. Thadhani, N.N. *Shock-induced chemical synthesis of intermetallic compounds*. 1990: Elsevier Science Publishers B. V.

5. Thadhani, N.N., et al., *Shock-induced chemical reactions and synthesis of binary compounds*, in *Shock Wave and High-Strain-Rate Phenomena in Materials*, L.E.M. M. A. Meyers, and K. P. Staudhammer, Editor. 1992, Marcel Dekker, Inc.: New York. p. 271-281.

6. Hunt, E.M., K.B. Plantier, and M.L. Plantoya, *Nano-scale reactants in the self-propagating high-temperature synthesis of nickel aluminide.* Acta Materiala, 2004. **52**(11): p. 3183-3191.

7. Wronski, *The size dependence of the melting point of small particles of tin.* British Journal of Applied Physics, 1967: p. 1731-1737.

8. Westbrook, J.H., *Mechanical Properties of Intermetallic Materials*. 1959, New York: Wiley.

9. Makino, A. and C.K. Law, *SHS combustion characteristics of several ceramics and intermetallic compounds.* Journal of the American Ceramic Society, 1994. **77**(3): p. 778.

10. Massalski, T.B.C., Editorial Committee), *Binary Alloy Phase Diagrams*. 1986, Metals Park, Ohio: American Society for Metals.

11. Horie, Y. and R.A. Graham, Materials Letters, 1985. **3**(9, 10): p. 354.

12. S. A. Paipetis, G.P., P.S. Theocaris, *Dynamic Properties of Metal-Filled Epoxy Polymers.* Fibre Science and Technology, 1975. **8**(3): p. 221-242.

13. Yi, H.C. and J.J. Moore, *Self-propagating high-temperature (combustion) synthesis (SHS) of powder-compacted materials.* Journal of Materials Science, 1990. **25**(2): p. 1159-1168.

14. Krueger, B.R., A.H. Mutz, and T. Vreeland, *Correlation of shock initiated and thermally initiated chemical reactions in a 1:1 atomic ratio nickel-silicon mixture.* Journal of Applied Physics, 1991. **70**(10): p. 5362-5368.

15. Fischer and Grubelich. *Theoretical energy release of thermites, intermetallics and combustible materials*. 1998.

16. Aizawa, T., *Shock reactive synthesis of refractory metal aluminides and silicides.* Ceramic Engineering and Science Proceedings, 1997. **18**(4B): p. 573-580.

17. Dunbar, E., N.N. Thadhani, and R.A. Graham, *High-pressure shock activation and mixing of nickel-aluminum powder mixtures.* Journal of Materials Science, 1993. **28**(11): p. 2903.

18. Thadhani, N.N., *Shock-induced and shock-assisted solid-state chemical reactions in powder mixtures.* Journal of Applied Physics, 1994. **76**(4): p. 2129-2138.

19. Vandersall, K.S. and N.N. Thadhani, *Investigation of "shock-induced" and "shock-assisted" chemical reactions in Mo + 2Si powder mixtures.* Metallurgical and Materials Transactions A: Physical Metallurgy and Materials Science, 2003. **34**(1): p. 15.

20. Hammetter, W.F. and R.A. Graham. 1988.

21. Namjoshi, S.A. and N.N. Thadhani, *Study of reaction kinetics in dynamically-densified Ti-Si powder mixtures.* 1999. **40**(12): p. 1347.

22. Munir, Z.A. and U. Anselmi-Tamburini, *Self-propagating exothermic reactions: the synthesis of high-temperature materials by combustion.* Materials Science Reports, 1989. **3**: p. 277-365.

23. Song, I. and N.N. Thadhani, *Effects of Shock Processing Parameters on Synthesis of Nickel Aluminides*, in *Shock Compression of Condensed Matter-1985*, J.N.J. S. C. Schmidt, L. W. Davison., Editor. 1990, Elsevier Science Publishers B. V. p. 499-502.

24. Aumann, C.E., G.L. Skofronick, and J.A. Martin, *Oxidation behavior of aluminum nanopowders.* Journal of Vacuum Science & Technology B: Microelectronics Processing and Phenomena, 1995. **13**(3): p. 1178.

25. Dubrovin, A.S., L.V. Slepova, and V.L. Kuznetsov, Combust Explos Shock Waves, 1970. **6**: p. 60.

26. Bockmon, B.S., et al. *Burn rates of nanocomposite thermites*. 2003. Reno, NV.

27. Jones, et al. *Comparative studies of the thermal hazards of Al nanopowders*. 2003.

28. Kwok, S.M., et al., *Characterization of aluminum nanopowder compositions.* Propellants, Explosives, Pyrotechnics, 2002. **27**: p. 229-240.

29. Lebrat, J.P., A. Varma, and P.J. McGinn, *Mechanistic studies in combustion synthesis of Ni_3Al and Ni_3Al-matrix composites.* Journal of Materials Research, 1994. **9**(5): p. 1184.

30. Licheri, R., R. Orru, and G. Cao, *Chemically-activated combustion synthesis of TiC-Ti composites.* Materials Science and Engineering A, 2004. **367**(1-2): p. 185.

31. Woody, D.L., J.J. Davis, and P.J. Miller. *Metal/metal exothermic reactions induced by low velocity impact*. 1996.

32. Yang, L., et al., *An analysis of shock-induced reactions in a Fe2O3 + Al + Teflon powder mixture*. 1996.

33. Taylor, G., *The use of flat-ended projectiles for determining dynamic yield stress. I: Theoretical considerations.* Proceedings of the Royal Society of London A, 1948. **194**: p. 289-299.

34. Whiffin, A.C., *The use of flat-ended projectiles for determining dynamic yield stress. II: Tests on various metallic materials.* Proceedings of the Royal Society of London A, 1948. **194**(1038): p. 300-322.

35. Carrington, W.E. and M.L.V. Gayler, *The use of flat-ended projectiles for determining dynamic yield stress. III: Changes in microstructure caused by deformation under impact at high striking velocities.* Proceedings of the Royal Society of London A, 1948. **194**(1038): p. 323-331.

36. Wilkins, M.L. and M.W. Guinan, *Impact of cylinders on a rigid boundary.* Journal of Applied Physics, 1973. **44**(3): p. 1200-1206.

37. Celentano, D.J., *Thermomechanical analysis of the Taylor impact test.* 2002. **91**(6): p. 3675.

38. House, J.W., et al., *Film data reduction from Taylor impact tests.* Journal of Strain Analysis for Engineering Design, 1999. **34**(5): p. 337.

39. House, J.W., et al., *Estimation of flow stress under high rate plastic deformation.* Int. J. Impact Eng., 1995. **16**(2): p. 189-200.

40. Millett, J.C.F., N.K. Bourne, and N.R. Barnes, *The behavior of an epoxy resin under one-dimensional shock loading.* Journal of Applied Physics, 2002. **92**(11): p. 6590.

41. Doucet, Q., Composite Engineering, 1993. **3**: p. 55.

42. Thaumaturgo, C. and A.M. DaCosta, Jr., *Shock-waves on polymer composites.* Journal of Materials Science Letters, 1997. **16**: p. 1480-1482.

43. F.R Christopher, J.C.F., Jr., L.L. Wilson, H.L. Gilland. *The Use of Impact Techniques to Characterize the High Rate Mechanical Properties of Plastic Bonded Explosives*. in *11th International Detonation Symposium*. 1998.

44. Roessig, K.M., J. J.C. Foster, and L.L. Wilson, *High Strain Rate Behavior of Plastic Bonded Explosives.* something Russian, 2001. **20**(8): p. 55-60.

45. Rae, P.J., et al. *The Taylor impact response of PTFE (Teflon)*. 2004.

46. Paipetis, S.A., G. Papanicolau, and P.S. Theocaris, *Dynamic Properties of Metal-Filled Epoxy Polymers.* Fibre Science and Technology, 1975. **8**(3): p. 221-242.

47. *ASTM Standard C 914-95: Standard Test Method for Bulk Density and Volume of Solid Refractories by Wax Immersion*. 1995.

48. in *LASL Shock Hugoniot Data*, S.P. Marsh, Editor. 1980, University of California Press: Berkeley, CA. p. 111, 166-167, 417, 467-468.

49. Meyers, M.A., *Dynamic Behavior of Materials*. 1994, New York: John Wiley & Sons, Inc. 668.

50. *ASTM Standard D695-02a: Standard Test Method for Compressive Properties of Rigid Plastics*. 2002.

51. Barker, L.M., *The VALYN VISAR User's Handbook*. 1996, VALYN International: Albuquerque, NM.

52. van Melick, H.G.H., L.E. Govaert, and H.E.H. Meijer, *On the origin of strain hardening in glassy polymers.* Polymer, 2003. **44**: p. 2493-2502.

53. Wetzel, B., F. Haupert, and M.Q. Zhang, *Epoxy nanocomposites with high mechanical and tribological performance.* Composites Science and Technology, 2003. **63**: p. 2055-2067.

54. Meguid, S.A. and Y. Sun, *On the tensile and shear strength of nano-reinforced composite interfaces.* Materials and Design, 2004. **25**: p. 289-296.

55. Hussain, M., A. Nakahira, and K. Niihara, *Mechanical property improvement of carbon fiber reinforced epoxy composites by Al_2O_3 filler dispersion.* Materilas Letters, 1996. **26**: p. 185-191.

56. Hasan, O.A. and M.C. Boyce, *A Constitutive Model for the Nonlinear Behavior of Glassy Polymers.* Polymer Engineering and Science, 1995. **35**(4): p. 331-344.

57. Lu, H., G. Tan, and W. Chen, *Modeling of Constitutive Behavior for Epon 828/T-403 at High Strain Rates.* Mechanics of Time-Dependent Materials, 2001. **5**: p. 119-130.